IMPLANTABLE LIGHT DELIVERY INTERFACES FOR OPTICAL NEURAL STIMULATION

by

Tanya Vanessa F. Abaya

A dissertation submitted to the faculty of
The University of Utah
in partial fulfillment of the requirements for the degree of

Doctor of Philosophy

Department of Electrical and Computer Engineering

The University of Utah

December 2013

The University of Utah Graduate School

STATEMENT OF DISSERTATION APPROVAL

The dissertation of **Tanya Vanessa F. Abaya**

has been approved by the following supervisory committee members:

Florian Solzbacher	, Chair	**10/30/13** Date Approved
Steve Blair	, Co-chair	**10/30/13** Date Approved
Gregory A. Clark	, Member	**11/22/13** Date Approved
Loren Rieth	, Member	**10/30/13** Date Approved
Michael A. Scarpulla	, Member	**10/30/13** Date Approved

and by **Gianluca Lazzi** , Chair/Dean of

the Department/College/School of **Electrical and Computer Engineering**

and by David B. Kieda, Dean of The Graduate School.

ABSTRACT

Optical methods are well-established in the fields of neuroscience, medical imaging, and diagnostics, etc. Optogenetics, for example, enables molecular specificity in optical neural stimulation and recording and has been named the "Method of the Year 2010" by Nature Methods. A novel microdevice was designed, fabricated, developed, and tested to facilitate three-dimensional (3D) deep-tissue light penetration with the capacity to accommodate spatiotemporal modulation of one or more wavelengths to advance a broad range of applications for optical neural interfaces. A 3D optrode array consisting of optically transparent "needles" can penetrate >1 mm directly into tissue, thereby creating multiple independent paths for light propagation that avoid attenuation due to tissue absorption and scattering, providing a high level of selectivity and comprehensive access to tissue not available in current interfaces.

Arrays were developed based upon silicon and glass. The silicon optrode array is based upon the well-established Utah electrode array architectures and is suitable for near-infrared (NIR) applications; glass optrodes are appropriate waveguides for both visible and NIR wavelengths. Arrays were bulk-micromachined with high-aspect ratio, a process that has not been reported to be applied to glass previously. In addition to device fabrication, extensive laboratory testing was performed with various optical sources to determine loss mechanisms and emitted beam profiles in tissue across the relevant wavelength ranges, with particular focus on performance metrics for optogenetic and infrared neural stimulation applications. Optrode arrays were determined to be amenable to integration with typical neural stimulation and imaging light delivery mechanisms such as optical fibers and microscopes. Glass optrodes were able to transmit light at ~90% efficiency through depths many times greater than the tissue attenuation length, with negligible light in-coupling loss. Si optrodes were determined to be only ~40% efficient with losses mostly from high

index contrast, tip backreflection, and taper radiation. The in-coupling technique and optrode geometry may be modified to produce illumination volumes appropriate for various experimental paradigms.

While the focus of this work is on optical neural stimulation, optrode array devices have application in basic neuroscience research, highly selective photodynamic therapy, and deep tissue imaging for diagnostics and therapy.

To my mom.

CONTENTS

LIST OF TABLES

ACKNOWLEDGMENTS

I would like to acknowledge the many people who have helped and supported me throughout my PhD years. My deepest appreciation goes to my advisers for trusting me and giving me independence to explore ideas, thus allowing to me grow as a researcher: Dr. Florian Solzbacher, first and foremost, for taking a chance on me and inviting me to join his research group, and Dr. Steve Blair, who provided much guidance in my work. I would also like to thank the rest of my committee members: Dr. Loren Rieth, who was always available to act as secondary adviser, Dr. Greg Clark, who always gave constructive criticsm and helped me out on the biology side, and Dr. Mike Scarpulla, who helped strengthen my work on the optics side.

My gratitude is extended to Dr. Prashant Tathireddy and to the members of the Microsystems Lab and Photonics Research Group for their feedback and suggestions that have contributed to substantiating my dissertation. Thank you to the Nanofab as well for equipment training and assistance; special mention to Brian Baker and Dr. Brian van Devener. I also want to thank our collaborators in upper campus that are helping advance the design and use of optrode arrays.

I am grateful for the friendships I have made in Salt Lake City, which made life easier and memorable along the way. I would have especially gone crazy while doing my PhD without Rajesh, Michelle, Phung, Becky, Jen, and Lori.

As always, thank you to my good friend Paulo for the inspiration.

My deepest gratitude goes to my family for always being so supportive and proud of me: Mom, Kuya, Ate, Mamang, Dad, Ate Fe, Jholo, Andrea, Enzo, Mikki, Inigo, and Kim. Thank you Mom for being the most awesome woman I know and showing me how to be awesome myself.

I would like to give a very big thanks to my life partner Dean for being my rock. I hoped

in my MS thesis acknowledgement that I will still be sharing this accomplishment with you, and here we are sharing new dreams and goals together.

Lastly, thank you to the universe that always seem to come through for me.

CHAPTER 1

INTRODUCTION

Control of neural activity for neuroscience research and neuroprosthesics applications is being developed using neural interface devices. The current gold standard for interfacing neural tissue is by electrical methods, and three-dimensional (3D) penetrating microelectrode arrays, such as the Utah electrode array (UEA), have been widespread for high-channel count electrical stimulation and recording. However, optical methods are becoming established in the fields of neuroscience, medical imaging and diagnostics, etc., because of several key advantages: lack of stimulus artifact, potential for longer-term stability, and intrinsic biocompatibility. A device structure facilitating 3D spatiotemporal high-density light delivery in deep tissue is a critical need and has yet to be demonstrated. In this work, optical neural interfaces similar in form to UEAs were designed, fabricated, and characterized for optical neural control.

This introduction consists of 6 sections. Neural interfaces and their role in neural control are first introduced, followed by a focus on photonic methods for brain and nerve stimulation. Considerations on tissue optics for light delivery in neural tissue are discussed next. The motivation and significance of this study is presented in section 1.4, succeeded by an overview of the proposed approach towards creating effective neural interfaces for light delivery. The last section discusses the specific aims of the study.

1.1 Neural control and neural interfaces

The nervous system coordinates all processes within the body. In neuroscience, the goal is to understand the structural, functional, and computational aspects of the nervous system. This objective is intimidating as there are billions of neurons making thousands of specific connections with one another to pass on dynamic information to control behavior,

memory, perception, physiology, etc. The brain has several cortical regions, each having layers of distinct combinations of various neuronal cell types and links to other regions. To advance the field, research employs external neural control and recording methods to isolate local networks of neurons/cells for identification of various specific functions and relationships within the nervous system. Artifical control also has serious implications for health; it is the basis of emerging prostheses and treatment for spinal cord and brain injury, sensory inadequacy, and neurological disorders. For example, spatial mapping of the visual cortex and its artifical stimulation has led to modalities for vision substitution [1, 2]; on the other hand, current techniques are still unable to determine exactly which cells or circuits are responsible for depression [3].

Approaches for neural control includes electrical, magnetic, and optical methods. Electrodes inject low-level pulsed current to generate signals called action potentials, or use senstivie amplifiers to record neural signals. Magnetic stimulation is commonly applied to studying the human brain and performed using fields produced from brief high-current pulses through a coil over the head. Depending on the stimulus parameters, neurons can either be excited or inhibited [4, 5]. Modern optical methods include micro-Watt optogenetic (visible light) and infrared stimulation in mammals [6, 7].

Because the nervous system functions via spatial and temporal patterns of electrical activity, neural interfaces are developed to transduce these patterns in tissue. Neural interfaces for electrical stimulation and recording have been extensively developed and utilized to progress neuronal information processing studies and functional rehabilitation. The most advanced control systems include cochlear prostheses to restore hearing capabilities to the otherwise profoundly deaf patients [8], deep brain stimulation to treat motor symptoms of Parkinson's disease [9], functional electrical stimulation to reanimate paralyzed limbs [10–14], and high-count electrode arrays to record brain signals and restore aspects of motor control to paralyzed individuals [15].

Among electrode array interfaces, the Utah architecture is distinguised as it is the only high-density penetrating micro-electrode array that is approved for human use by the Federal Drug Administration. The Utah electrode array (UEA) and Utah slant electrode array (USEA) are shown in Figures 1.1(a) and 1.1(b). These are doped silicon arrays

typically consisting of 100 tapered electrodes in a 10×10 configuration with a 400 μm pitch. The UEA has 1.5-mm long electrodes used for interfacing with the cortex, while the USEA has electrode lengths varying form 0.5 to 1.5 mm in one direction to gain access to nerve fibers (i.e., axons) across the cross-section of peripheral nerves. The UEA/USEAs have been designed for restoration of vision, hearing, bladder control, and motor function among others [16–19]. In addition, both wired and wireless Utah arrays have been developed; the wireless integrated neural interface in Figure 1.1(c) is designed for neuroprothetic applications and can allow the study of free-moving animals without the implanted device affecting experimental results [20].

The UEA/USEAs have been demonstrated to provide multiple independent focal stimulation/recording sites across the 3D structure of neural tissue, a high degree of selectivity, chemical and mechanical stability, and ease of implantation [21–25]. Despite the invasiveness of the penetrating array, chronic studies have demonstrated the UEA/USEA long-term functionality. Behavioral responses of cats to chronic sciatic nerve implants are generally benign, and long-term chronic physiology and device stability have shown considerable improvement [23] relative to initial investigations [26]; stimulation remains highly selective among individual electrodes four months (terminal experimental time point) after implantation. Longer-term reliability of implanted arrays in rhesus macaque motor cortex was observed for over 31 months, although a slow decline of recorded action potential amplitude was recognized [27, 28]; degradation was not discernable for a study period of 569 days [29]. In paralyzed humans, the commercialized version of the UEA device has been tested successfully [15]. Furthermore, no adverse results were reported in one human subject who had an array implanted in the median nerve [30].

Interest in optical methods has grown in the last couple of years. Optogenetics, for example, despite being a nascent field of study, has been named the Method of the Year 2010 by Nature Methods. Due to the infancy of optical neural control, development of neural interfaces for light transmission is also in its early stages and experiments typically utilize optical fibers or optical microscopy hardware to couple light into tissue (see Chapter 2).

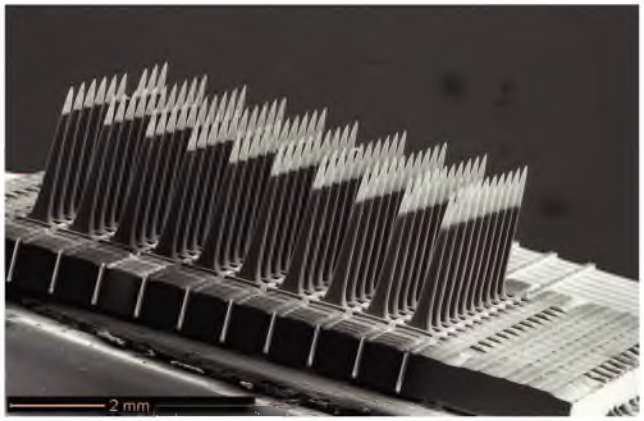

(a)

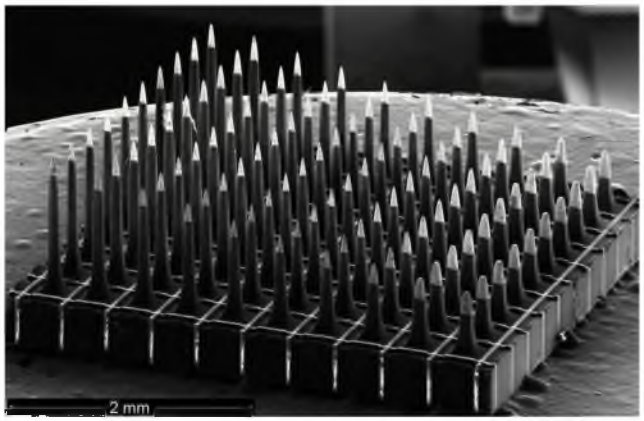

(b)

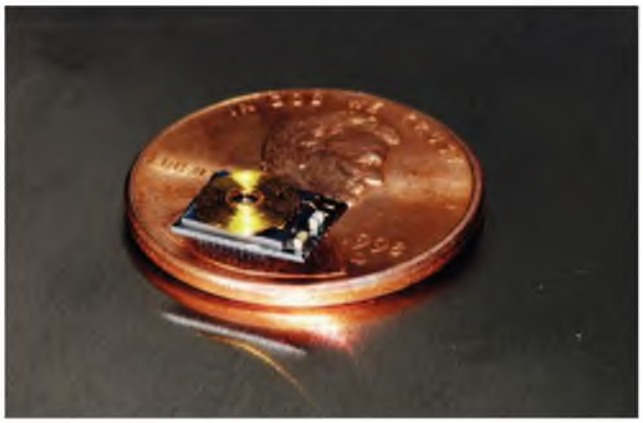

(c)

Figure 1.1. 10×10 silicon micro-electrode arrays with 400 μm pitch. (a) Utah electrode arrays primarily implanted in the brain consist of 1.5-mm long missile-shaped needles. (b) Utah slant electrode arrays provide comprehensive access to peripheral nerves by having 0.5 to 1.5-mm long electrodes. (c) An array can be integrated as a wireless neural interface composed of an inductive power receiving coil, a custom-designed signal processing and telemetry IC, and surface-mount capacitors.

1.2 Neurophotonics

Neurophotonics, which is the use of light to investigate and interact with neuronal tissue, is an emerging alternative to electrical-based strategies. Methods for neural control include infrared (IR) stimulation and optogenetics using visible light (sections 1.2.1 and 1.2.2). Optical stimulation and/or recording of neural activity has several advantages. First, optical stimulation is more biocompatible; it eliminates potentially harmful by-products of electrochemical reactions involved in electrical stimulation [31], and under some circumstances does not require direct contact between the probe and tissue. In cases where penetrating probes are implanted, rejection or destruction of an optical neural interface is less likely to occur as its materials (e.g., fused silica, polydimethylsiloxane) are chemically inert and/or have excellent biocompatibility [32, 33]. Further, encapsulation methods may be applied to optical probes; biocompatibility of electrical neural interfaces has been enforced by encapsulation techniques involving use of silicon carbide, polymide, silicon nitride, silicon dioxode, silicone, or FDA-approved polydimethylsiloxane (PDMS) or parylene-C [24, 34, 35].

Penetrating probes for optical stimulation can also potentially perform with longer-term stability. After implantation, the formation of glial scar encapsulates the active sites and isolates the device from electrical communication with the neurons [36–38]. Whereas the glial scar acts as an insulator that degrades signals during electrical stimulation/recording, formation of glial scars is not problematic from a neurophotonics perspective; glial scars are mainly composed of reactive astrocytes within an extracellular matrix consisting of lamina and other structural networks [39, 40]. Although there are inadequate data on the optical properties of glial scar, glia is largely optically transparent and is not expected to hinder optical stimulation [41].

With optical stimulation, there is also absence of electrical current spread that can reduce the selectivity of stimulation and produce a stimulus artifact [42]. Consequently, one can potentially stimulate optically and record electrically at or near the same time and location, which is a great advantage. Lastly, cell-type specific stimulation of neuronal or glial subpopulations are possible with optogenetic methods [7, 43]; illumination within a volume full of neurons will only activate cell types genetically coded for manipulation.

1.2.1 Optogenetics

Optogenetics is an optical approach to excite or inhibit neurons to trigger or prevent explicit events in specific cells. This method has a temporal precision in the millisecond-scale and is achieved through the use of light-sensitive control tools that may be targeted by gene delivery [44, 45]. Only specific cell types will express the control tools (e.g., only oligodendrocytes but not astrocytes, which are both glial cells [46]). The control tools are mainly light-gated ion channels in the microbial opsin family; examples of microbial opsins characterized for optogenetics include channelrodopsin-2 (ChR2; responsive to blue light for neuronal excitation), halorhodopsin (NpHR; responsive to yellow light for inhibition), archaerhodopsin-3 (Arch; responsive to yellow-green light for inhibition), channelrhodopsin from *Volvox carteri* (VChR; activated by green light), and various ChR2 chimeras (e.g., ChR2(T159C), ChR2(H1s3R), ChETA) [47–51]. With typical ChR2 expression levels in cells illuminated with $\lambda = 473\,\text{nm}$, $\sim$1 mW/mm^2 intensity at $\sim$10 ms exposure time is required to achieve depolarization across the cell membrane, leading to the generation of compound action potentials [7]. However, light delivery requirements (e.g., intensity, exposure time) for each type of rhodopsin is influenced by its light sensitivity and kinetic properties as well as the animal model [45, 52]. In nonhuman primates, a minimum of $2.6\,\text{mW/mm}^2$ is needed to produce a 1 kHz spike rate from activation of ChR2-expressing cells [52]. Also, NpHR is reported to have a threshold intensity of $21.8\,\text{mW/mm}^2$ for 100% spike suppression during illumination [48].

Optogenetics was first demonstrated using ChR2 in scattered hippocampal neurons in the mammalian brain with noninvasive delivery of brief pulses of blue light, which prompted neuronal depolarization at the resolution of single spikes [7]. Noncontact transmission of light into tissue necessitates optical input that is $>100\times$ of the intensity required at the target cell to compensate for scattering [41]; research with the mammalian brain with illumination at $\lambda = 473\,\text{nm}$ on the brain surface from a 100-μm fiber of 0.22 NA estimates that the irradiance decreases rapidly to 10% of the value on the surface within only 300 μm deep [45].

1.2.2 Infrared neural stimulation

A method of directly stimulating neural tissue with IR radiation is referred to as infrared neural stimulation (INS). Nerve stimulation with infrared light at 1.064 μm was demonstrated in Aplysia (sea slug) in 1971 [53]. However, stimulation with IR light ($\lambda = 2.1$ to 6.1 μm) was first systematically analyzed in 2005 using rat sciatic nerve with a laser-coupled 600-μm optical fiber emitting a pulsed laser beam on a single spot on the nerve surface [6, 54]. Action potentials were selectively evoked without causing histological tissue damage. Stimulation and ablation fluence thresholds were determined; wavelengths having lower absorption coefficients (i.e., higher penetration depth) in tissue had larger safety margins, while those having high absorption only stimulated at energies above the damage threshold. Wavelengths of 2.1 and 4 μm, which are at relative valleys of the absoprtion spectrum, were found to be particularly well suited for extraneural infrared stimulation of rat peripheral nerves. Both stimluation and ablation trends were observed to depend on the absorption spectrum of water; the damage threshold was strongly affected by the absorption coefficient, but stimulation threshold levels varied less. Activation and damage levels are about the same for $\lambda = 3$ μm because the dose needed to surpass the epineurium (connective tissue layer surrounding nerve) is likely equal to the minimum dose for IR energy deposition in fibers beneath the epineurium. For 2.1-μm wavelength, light is able to penetrate further than the epineurium but requires more input energy for stimulation due to lower absorption; the location of stimulation is probably in the inner fibers.

Other INS applications including cochlear prosthesis, embryonic heart pacing, brain stimulation, and nerve fiber identification for diagnostics emerged using noncontact delivery of pulsed light via a single fiber as well [55–58]. Wavelengths of $\sim$1.45, $\sim$1.87 and 2.12 μm, which have similar absorption, have also been used to balance optimal penetration with stimulation efficacy.

Measurements of surface nerve temperatures suggest that INS acts via the induction of a spatiotemporal heat gradient in the tissue (4°C at the axonal level with about 3 mJ/mm^2 extraneural threshold dose) [59]. The underlying physiological mechanism is still under investigation, although it has been posed that IR is absorbed in tissue during INS and causes local tissue heating that depolarizes the target cell by changing the membrane electrical

capacitance [60].

Infared-triggered temperature changes have also been demonstrated to activate thermal transient receptor potential (TRP) ion channels [61], which can be genetically targeted to perform thermogenetic stimulation (similar to rhodopsins for optogenetic stimulation); these TRP channels are $\sim 1000\times$ more sensitive than optogenetic tools (i.e., produce the same current at much lower expression levels) and have mainly been useful in the study of the relationship between specific neuronal activation to behavioral outputs in fruit flies, which does not require high temporal resolution [62–64].

1.3 Tissue optics for neurophotonics

Light-tissue interactions are limited by the penetration depth of light into tissue, which is limited by absorption and/or scattering; these limitations are strongly wavelength dependent and can only be partially overcome by increasing light fluence due to the potential for damage. Figure 1.2 plots a tissue attenuation spectrum, which is the combination of absorption and scattering [65]. Tissue components that absorb light are known as the chromophores, which in skin are melanin, hemoglobin, and water. Tissue absorption is dominated by amino acids, nucleic acids, and hemoglobin below 450-nm wavelength, while absorption is dominated by (oxy)hemoglobin and melanin between 450 and 700 nm; beyond about 1400 nm, the dominant chromophore is water [66]. Scattering is typically described by a combination of Rayleigh and Mie scattering. Rayleigh scattering scales as $1/\lambda^4$, and Mie scattering scales as $1/\lambda^p$ with p determined by the effective particle size [65]. Scattering dictates the light transport for wavelengths in the visible range and less strongly impacts total attenuation at infrared wavelengths, making IR light at the water absorption bands effective for heat generation at useful depths in tissue [6, 59]. Penetration depth (i.e., depth where intensity falls to $1/e$ of surface value) is roughly limited in the range of 100 μm to 1 mm from the blue to near-IR.

With visible light, the practical depth limit for many applications is a few hundred microns, which has significance to tissue spectroscopy, optogenetic methods, and photomedicine, for example. In the IR, one may argue that the limit is deeper as the 650–950 nm window have been used in imaging to effective depths of $\sim$1 cm below the tissue surface.

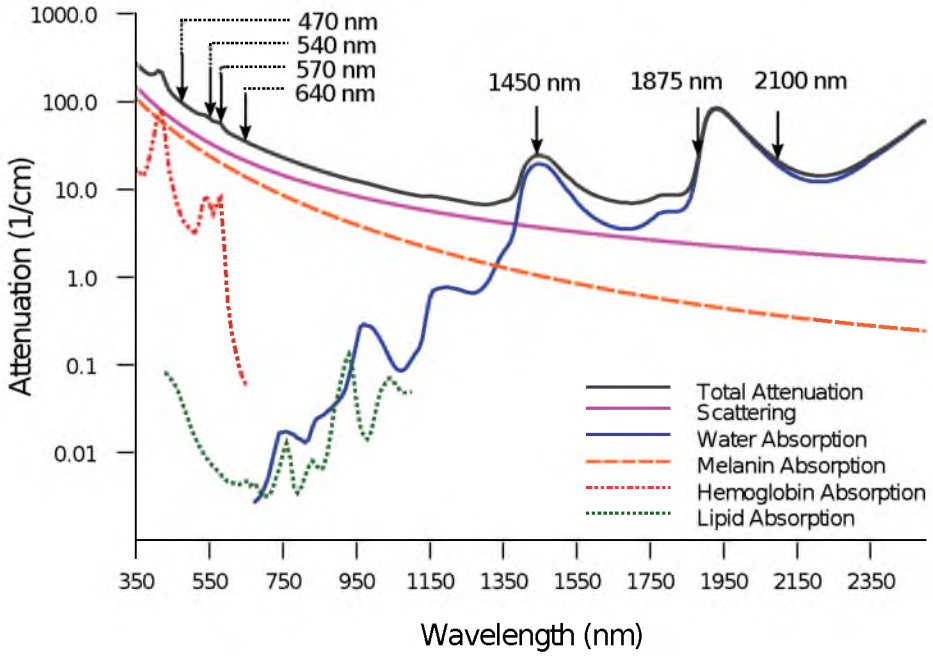

Figure 1.2. Representative components of tissue attenuation. Absorption in skin is due primarily to melanin, and in perfused tissue, hemoglobin, while water is the primary chromophore in the infrared. Scattering more strongly affects visible to short wavelength propagation. Penetration depth (i.e., depth where intensity falls to $1/e$ of surface value) is limited in the range of 100 μm to 1 mm from the blue to near-IR. Relevant wavelengths for neurophotonic stimulation are indicated as well.

However, most imaging results are gathered from scattering data [67]; scattering makes the signal at such depth weak and insufficient for optical stimulation. The intensity of light concentrated in a defined area is of interest in optical stimulation. Indeed, higher light intensity incident on cells expressing channelrhodopsin variants result in higher levels of action potential recordings [50]. Results of extraneural INS also reveal that wavelengths having approximately zero penetration depths easily created nerve damage with threshold stimulation fluence, and wavelengths with very low absorption will likely fail to deliver sufficient amounts of energy to evoke a response [54].

The NIR wavelength range is also popular for optical methods based upon two-photon absorption to excite chromophores in the visible, but scattering of excitatation light and recording return light in the visible imposes similar depth limitations as with visible excitation, to ~800 μm [68]. Two-photon excitation with wavelengths in this NIR window (i.e., 900–920 nm) have been applied for optogenetic stimulation, reaching as deep as 240 μm into

tissue [69–71]. Still, two-photon strategies typically operate at depths of only ~500 μm and may be limited to ~1 mm [72, 73].

1.4 Motivation and significance

Although numerous experiments have been performed for the study of neurological function and neuroprosthesis using optical control, neural interfaces providing the vital capabilities for light delivery in tissue have yet to be presented.

The advantages of neural control via light activation discussed in section 1.2 open up opportunities for neurological studies not possible with electrical stimulation. Optogenetics now allows the identification of the role of specific neurons in brain function, health and disease; the absence of a stimulus artifact with light stimulation also allows simultaneous recording of sensory inputs and stimulation. Many studies in neuroscience are based upon the stimulation and/or recording of activity in the neocortex. In mammals, the neocortex consists of up to six layers of different neuronal subtypes; neocortex thickness ranges from 0.5 to 1 mm in rodents to 2 to 4 mm in primates. Optical stimulation techniques have also been applied to the peripheral nervous system. Specific and selective stimulation of the peripheral nerves with both optogenetic and infrared techniques has been demonstrated, aiming towards the restoration of optimal neural or muscle control of disabled subjects [2, 55, 74–76]. The dimensions and operations of the brain and nerves necessitate deep penetration of light for optical neural control. Consequently, deeper brain sections or innermost nerve fibers are inaccessible, which restricts the location of optical manipulation and/or observation. 3D access along the width, length, and depth in tissue with patterned stimulation has been implemented for electrical stimulation using Utah micro-electrode arrays, as already mentioned in section 1.1. The success of the UEA/USEA makes its blueprint a good candidate for optical neural interface design. The architecture is well suited to the neocortex—depth can be adjusted according to the specific layer/s to be accessed, and the pitch is ideally matched to the width of the columnar units. The multiple needles available within the array allow utilization of complex stimuli combinations that imitate natural nervous system processes/responses. As previously demonstrated, the high-channel electrode count allows successive recruitment of neurons to evoke maximal

fatigue-resistant forces in various muscles [77]; furthermore, a graceful feline stance with paralyzed hind limbs of the cat was produced by the graded activation of several muscles using the USEA [78]. Across a wide range of mammalian species, the array architecture maps well to the architecture of large peripheral nerves.

Beyond 3D access to tissue, optical neural control may require several other features. Optical input delivered into tissue may be comprised of multiple wavelengths. In optogenetic applications facilitating bidirectional interrogation of neural circuits, multiple independent light sources over the same area/volume are needed because of the simultaneous expression of ChR2 and NpHR for exciting and inhibiting the same target cell, respectively [48, 79, 80]. Neural modulation advances understanding of synaptic connectivity between excitatory and inhibitory neurons within neocortical microcircuits to reveal processing of sensory information and high-speed functional operation of neuronal networks in general [81]. Identification of disease-related neuronal types to improve therapy may also be conducted using bidirectional modulation [48].

Different wavelengths of light experience different scattering and absorption in different types of tissue [45], which makes control of the illuminated volume harder to control. The same set of illumination parameters will not guarantee the same illumination profile for different wavelengths and thus, functional performance can vary with wavelength. Illumination volume control may be achieved by varying light source characteristics (e.g., numerical aperture, size, power), input coupling mechanism (e.g., through aperture, lens, attenuator), and even waveguide geometry (if waveuide is used) to influence the morphology of the volume illuminated above threshold.

Given the multifarious experimental paradigms and the complex operation and 3D structure of tissue, the features of an ideal light delivery interface for optical neural control are summarized as follows. Features include:

(a) effective deep tissue light penetration

(b) input spatiotemporal patterning capability

(c) adaptability to various light sources, possibly including integration of multiple light sources of varying wavelengths and/or to existing experimental platforms

(d) flexibility in manufacturing to alter geometry as well as performance characteristics to cater to diverse animal models and test platforms for a wide range of optical neural control applications

(e) versatility as an *in-vitro* or *in-vivo* and acute or chronic device for stationary or mobile subjects

(f) implantability

(g) biocompatibility

1.5 Hypothesis

The overarching hypothesis of this work is that an optical neural array based on the UEA/USEA architectures is an excellent light delivery device for optical neural control experiments for neuroengineering and neuroscience research. Instead of electrodes, each needle in the array constitutes a waveguide and is optimized for light transmission. Such design may meet efficiency, depth access and emission profile requirements of optical stimulation of a range of tissue structures.

A neural waveguide array, which is essentially an *optrode array* (analogous to an electrode array), breaks the penetration depth barrier for multipath light propagation into tissue under all modes of operation, ranging from visible to the near infrared, and including multiphoton techniques. Admittedly, the 3D resolution of a 10×10 or even a 40×40 array will not match that obtained with scanning confocal microscopy. Nevertheless, even with the reduced spatial resolvability, the optrode array offers unprecedented depth access (as with any penetrating probe approach) combined with the application of any light stimulus combination that is not limited to the raster patterns of scanning microscopy. Like the UEA/USEA again, the optrode array may be wired or wireless in the long term, depending on the power in-coupling mechanism integrated with it. A wireless optrode array would be best for chronic *in-vivo* implantations for mobile subjects.

The optrode device may thus introduce transformative benefits relative to current optical approaches to tissue interactions in the contexts of fundamental neuroscience studies and neuroengineering applications. The advantages offered by penetrating optical probe architectures are already recognized [82–84]. An optrode array is perhaps the most flexible device

in offering quasi-3D spatially-multiplexed (and possibly input wavelength time-multiplexed) optical neural control, and it is based upon an architecture that has been deployed successfully for decades in electrical stimulation and recording studies [85, 86]. In fact, the UEA device has been successfully implanted for chronic studies, with operational lifetimes in primates exceeding 31 months [27]. Furthermore, one of the *in-vivo* penetrating optical neural interfaces in use today is based upon a single tapered optical fiber inserted at a central position within a commercial USEA device [82], which has had a demonstrated chronic implant lifetime of eight months [87] in the neocortex of a transgenic rat.

1.6 Specific aims and thesis outline

The overall objective of this work is to design, characterize, and develop waveguide array interfaces for optical neural control. The specific aims are as follows:

(a) *Adapt the Utah electrode array architecture for infrared light delivery.* Silicon neural array fabrication is well established and well documented. Intrinsic silicon, which is transparent to near-infrared wavelengths, can be fabricated using processes similar to the traditional device for enabling light transmission. Infrared neural stimulation is most commonly applied to peripheral nerves. In electrical stimulation of peripheral nerves with micro-electrode arrays, the slanted architecture (i.e., USEA) is used because it provides comprehensive access along the width and the depth of the nerve. The USEA is taken and optimized for light transmission. The electrodes became optrodes, and the USEA becomes the Utah slant optrode array (USOA). Changes in the fabrication processes due to the change in substrate and application must be identified; the transmission efficiency is the most important metric to be characterized. To this end, several bench test setups are designed to quantify and/or characterize the losses (e.g., Fresnel, in-couplin, taper) suffered by optrodes of different physical dimensions. Illumination volumes from the optrode tips must also be sufficient for INS; output beam profiles must be extracted and analyzed.

(b) *Extend the use of optical neural arrays to optogenetic applications.* Fused silica/quartz is a very good candidate material for a light delivery interface from an optics perspective, especially if coupled from optical fibers (also made of fused silica).

Glass has a refractive index close to that of tissue (i.e., $n = 1.45$ compared to $n = 1.36$ for tissue) and is transparent to both visible and near-infrared. Fabrication of glass optrode arrays leverages off the extensive work done on UEA engineering. Still, there are differences in chemical and mechanical properties between glass and silicon; etching and dicing parameters (e.g., feed speed, revolutions) needs to be investigated a great deal until yield is satisfactory. Efficiency, emission profile, and losses are also characterized. Light in-coupling is explored in greater depth compared to the USOA because of the more varied techniques/requirements of light delivery for optogenetics. In addition, insertion of glass optrodes into tissue must be examined, especially if geometry is different from the well-established silicon electrodes.

(c) *Characterize device performance in tissue.* The aim is to further understand the suitability of optrodes for optical neural control light delivery and develop methods to predict transmitted intensity and profile in tissue. The effect of tissue optical properties on the transmission efficiency of the optrodes is investigated. An ideal result is to get a transmission that is barely influenced by wavelength and the surrounding media; this would imply that light delivery depth is practically independent of tissue optical properties, but is rather dictated by the optrode length. The output beam profiles in tissue for different optrode geometries are also measured to verify spatial coverage of target tissue structures (e.g., neuron, cell, brain layer) in optical neural control. The profiles are compared with results from modeling and bench tests in air in order to examine whether estimates from models or theoretical derivations from results in air will suffice to determine optrode geometries appropriate for specific tissues/applications.

(d) *Investigate light in-coupling mechanisms for highly-efficient optrode arrays.* Measurements and analysis of coupling from various sources (e.g., lasers) and via different methods (e.g., lenses) are performed to evaluate the ease to which current light delivery techniques may be modified to include optrode arrays. More importantly, this will provide insight on enabling techniques towards a fully-integrated optical neural interface.

In summary, the study aims to establish fabrication and application methods for highly efficient optrode arrays and systematically evaluate performance metrics with respect to a wide range of optogenetic and infrared neural stimulation applications. The primary metrics are transmission efficiency and illumination volume from the output beam profile.

This dissertation starts with an overview of neural control, neural interfaces, and neurophotonics here in Chapter 1. Chapter 2 then describes currently developed or implemented optical techniques or devices for optogenetic and infrared stimulus delivery in tissue, and compares the proposed optrode arrays to other architectures. Chapter 3 introduces the USOA for infrared neural stimulation (INS) and gives a comprehensive discussion on its fabrication, sources of loss, light transmission charateristics and output beam profiles dependent on geometry, and practical efficiency with standard INS platform. The glass optrode array for both INS and optogenetics is presented in Chapter 4 with similar analysis as the USOA in the previous chapter. Chapter 5 provides the characterization in tissue for both types of optical neural arrays. This chapter includes the modeling and analysis of the effect on the transimission efficiency of tissue optical properties as well as emission profiles in tissue for various wavelengths with modeling and estimation from bench tests in air. Also included is a remark on how various optrode illumination profiles are appropriate for varying optical neural control applications. Various light in-coupling mechanisms are investigated in Chapter 6; analysis on coupling from fibers, Lambertian and Gaussian sources, collimated beams, and through lenses (e.g., microscope obectives) is the scope of this chapter. Finally, the findings are summarized in Chapter 7; conclusions and suggestions for future study are also outlined.

1.7 References

[1] R. A. Normann, D. J. Warren, J. Ammermuller, E. Fernandez, and S. Guillory, "High-resolution spatio-temporal mapping of visual pathways using multi-electrode arrays," Vision Res. **41**, 1261–1275 (2001).

[2] W. Al-Atabany, B. McGovern, K. Mehran, R. Berlinguer-Palmini, and P. Degenaar, "A processing platform for optoelectronic/optogenetic retinal prosthesis," Biomedical Engineering, IEEE Transactions on **PP**, 1 (2011).

[3] A. Komaroff, ed., *Understanding Depression* (Harvard Health Publications, 2011).

[4] A. Barker, R. Jalinous, and I. Freeston, "Non-invasive magnetic stimulation of human motor cortex," The Lancet **325**, 1106–1107 (1985).

[5] A. Rotem and E. Moses, "Magnetic stimulation of one-dimensional neuronal cultures," Biophys. J. **94**, 5065–5078 (2008).

[6] J. Wells, C. Kao, K. Mariappan, J. Albea, E. D. Jansen, P. Konrad, and A. Mahadevan-Jansen, "Optical stimulation of neural tissue in vivo," Opt. Lett. **30**, 504–506 (2005).

[7] E. S. Boyden, F. Zhang, E. Bamberg, G. Nagel, and K. Deisseroth, "Millisecond-timescale, genetically targeted optical control of neural activity," Nat. Neurosci. **8**, 1263–1268 (2005).

[8] J. T. Rubinstein and C. A. Miller, "How do cochlear prostheses work?" Curr. Opin. Neurobiol. **9**, 399–404 (1999).

[9] A. L. Benabid, "Deep brain stimulation for parkinsons disease," Curr. Opin. Neurobiol. **13**, 696–706 (2003).

[10] M. W. Keith, P. H. Peckham, G. B. Thrope, K. C. Stroh, B. Smith, J. R. Buckett, K. L. Kilgore, and J. W. Jatich, "Implantable functional neuromuscular stimulation in the tetraplegic hand," J. Hand Surg. Am. **14**, 524–530 (1989).

[11] K. L. Kilgore, P. H. Peckham, M. W. Keith, G. B. Thrope, K. S. Wuolle, A. M. Bryden, and R. L. Hart, "An implanted upper-extremity neuroprosthesis. Follow-up of Five Patients," J. Bone Joint Surg. **79**, 533–41 (1997).

[12] P. Peckham, M. W. Keith, K. L. Kilgore, J. H. Grill, K. S. Wuolle, G. B. Thrope, P. Gorman, J. Hobby, M. Mulcahey, S. Carroll, V. R. Hentz, and A. Wiegner, "Efficacy of an implanted neuroprosthesis for restoring hand grasp in tetraplegia: a multicenter study," Arch. Phys. Med. Rehabil. **82**, 1380–1388 (2001).

[13] P. Peckham, K. L. Kilgore, M. W. Keith, A. M. Bryden, N. Bhadra, and F. W. Montague, "An advanced neuroprosthesis for restoration of hand and upper arm control using an implantable controller," J. Hand Surg. Am. **27**, 265–276 (2002).

[14] B. Smith, Z. Tang, M. Johnson, S. Pourmehdi, M. Gazdik, J. Buckett, and P. Peckham, "An externally powered, multichannel, implantable stimulator-telemeter for control of paralyzed muscle," IEEE T. Bio-Med. Eng. **45**, 463–475 (1998).

[15] L. R. Hochberg, M. D. Serruya, G. M. Friehs, J. A. Mukand, M. Saleh, A. Caplan, A. Branner, D. Chen, R. D. Penn, and J. P. Donoghue, "Neuronal ensemble control of prosthetic devices by a human with tetraplegia," Nature **442**, 164–171 (2006).

[16] R. Bhandari, S. Negi, L. Rieth, R. A. Normann, and F. Solzbacher, "A novel method of fabricating convoluted shaped electrode arrays for neural and retinal prostheses," Sens. Actuators A Phys. **145-146**, 123–130 (2008).

[17] T. Davis, R. Parker, P. House, E. Bagley, S. Wendelken, R. Normann, and G. B., "Spatial and temporal characteristics of v1 microstimulation during chronic implantation of a microelectrode array in a behaving macaque." J. Neural Eng. **9**, 065003 (2012).

[18] T. Hillman, A. Badi, R. Normann, T. Kertesz, and C. Shelton, "Cochlear nerve stimulation with a 3-dimensional penetrating electrode array." Otol. Neurotol. **24**, 764–768 (2003).

[19] H. A. C. Wark, B. R. Dowden, P. C. Cartwright, and R. A. Normann, "Selective activation of the muscles of micturition using intrafascicular stimulation of the pudendal nerve," J. Emerg. Sel. Topic Circuits Syst. **1**, 631–636 (2011).

[20] R. Harrison, R. Kier, S. Kim, L. Rieth, D. Warren, N. Ledbetter, G. Clark, F. Solzbacher, C. Chestek, V. Gilja, P. Nuyujukian, S. Ryu, and K. Shenoy, "A wireless neural interface for chronic recording," in *Proceedings of IEEE Biomedical Circuits and Systems Conference* (2008), pp. 125–128.

[21] A. Branner and R. Normann, "A multielectrode array for intrafascicular recording and stimulation in sciatic nerve of cats," Brain Res Bull **51**, 293C306 (2000).

[22] A. Branner, R. B. Stein, and R. A. Normann, "Selective stimulation of cat sciatic nerve using an array of varying-length microelectrodes," J. Neurophysiol. **85**, 1585–1594 (2001).

[23] G. Clark, N. Ledbetter, D. Warren, and R. Harrison, "Recording sensory and motor information from peripheral nerves with utah slanted electrode arrays," in *Proceedings of International Conference of the IEEE Engineering in Medicine and Biology Society* (2011), pp. 4641–4644.

[24] J.-M. Hsu, L. Rieth, R. Normann, P. Tathireddy, and F. Solzbacher, "Encapsulation of an integrated neural interface device with parylene C," IEEE T. Bio-Med. Eng. **56**, 23–29 (2009).

[25] P. Rousche and R. Normann, "A method for pneumatically inserting an array of penetrating electrodes into cortical tissue," Ann. Biomed. Eng. **20**, 413–422 (1992).

[26] A. Branner, R. Stein, E. Fernandez, Y. Aoyagi, and R. Normann, "Long-term stimulation and recording with a penetrating microelectrode array in cat sciatic nerve," IEEE T. Bio-Med. Eng. **51**, 146–157 (2004).

[27] C. A. Chestek, V. Gilja, P. Nuyujukian, J. D. Foster, J. M. Fan, M. T. Kaufman, M. M. Churchland, Z. Rivera-Alvidrez, J. P. Cunningham, S. I. Ryu, and K. V. Shenoy, "Long-term stability of neural prosthetic control signals from silicon cortical arrays in rhesus macaque motor cortex," J. Neural Eng. **8**, 045005 (2011).

[28] G. Santhanam, M. Linderman, V. Gilja, A. Afshar, S. Ryu, T. Meng, and K. Shenoy, "Hermesb: a continuous neural recording system for freely behaving primates," IEEE T. Bio-Med. Eng. **54**, 2037–2050 (2007).

[29] S. Suner, M. Fellows, C. Vargas-Irwin, G. Nakata, and J. Donoghue, "Reliability of signals from a chronically implanted, silicon-based electrode array in non-human primate primary motor cortex," IEEE T. Neur. Sys. Reh. **13**, 524–541 (2005).

[30] K. Warwick, M. Gasson, B. Hutt, I. Goodhew, P. Kyberd, B. Andrews, P. Teddy, and A. Shad, "The application of implant technology for cybernetic systems," Arch. Neurol. **60**, 1369–1373 (2003).

[31] Y.-T. Kim, R. W. Hitchcock, M. J. Bridge, and P. A. Tresco, "Chronic response of adult rat brain tissue to implants anchored to the skull," Biomaterials **25**, 2229–2237 (2004).

[32] K. Lilienthal, M. Stubenrauch, M. Fischer, and A. Schober, "Fused silica 'glass grass': fabrication and utilization," J. Micromech. Microeng, **20**, 025017 (2010).

[33] S. L. Peterson, A. McDonald, P. L. Gourley, and D. Y. Sasaki, "Poly(dimethylsiloxane) thin films as biocompatible coatings for microfluidic devices: Cell culture and flow studies with glial cells," J. Biomed. Mater. Res. **72A**, 10–18 (2005).

[34] S. F. Cogan, D. J. Edell, A. A. Guzelian, Y. Ping Liu, and R. Edell, "Plasma-enhanced chemical vapor deposited silicon carbide as an implantable dielectric coating," J. Biomed. Mater. Res., Part A **67A**, 856–867 (2003).

[35] S. Myllymaa, K. Myllymaa, and R. Lappalainen, *Recent Advances in Biomedical Engineering* (InTech, 2009), chap. 9, pp. 165–169.

[36] M. P. Ward, P. Rajdev, C. Ellison, and P. P. Irazoqui, "Toward a comparison of microelectrodes for acute and chronic recordings," Brain Res. **1282**, 183–200 (2009).

[37] V. S. Polikov, M. L. Block, J.-M. Fellous, J.-S. Hong, and W. M. Reichert, "In vitro model of glial scarring around neuroelectrodes chronically implanted in the CNS," Biomaterials **27**, 5368–5376 (2006).

[38] D. Szarowski, M. Andersen, S. Retterer, A. Spence, M. Isaacson, H. Craighead, J. Turner, and W. Shain, "Brain responses to micro-machined silicon devices," Brain Res. **983**, 23–35 (2003).

[39] E. Camand, M.-P. Morel, A. Faissner, C. Sotelo, and I. Dusart, "Long-term changes in the molecular composition of the glial scar and progressive increase of serotoninergic fibre sprouting after hemisection of the mouse spinal cord," Eur. J. Neurosci. **20**, 1161–1176 (2004).

[40] C. C. Stichel and H. W. Muller, "The CNS lesion scar: new vistas on an old regeneration barrier," Cell Tissue Res. **294**, 1–9 (1998).

[41] A. M. Aravanis, L.-P. Wang, F. Zhang, L. A. Meltzer, M. Z. Mogri, M. B. Schneider, and K. Deisseroth, "An optical neural interface: in vivo control of rodent motor cortex with integrated fiberoptic and optogenetic technology," J. Neural Eng. **4**, S143 (2007).

[42] J. Wells, P. Konrad, C. Kao, E. D. Jansen, and A. Mahadevan-Jansen, "Pulsed laser versus electrical energy for peripheral nerve stimulation," J. Neurosci. Methods **163**, 326–337 (2007).

[43] A. R. Adamantidis, F. Zhang, A. M. Aravanis, and K. D. L. de Lecea, "Neural substrates of awakening probed with optogenetic control of hypocretin neurons," Nature **450**, 420–424 (2007).

[44] K. Deisseroth, "Optogenetics," Nat. Methods **8**, 26–29 (2011).

[45] O. Yizhar, L. Fenno, T. Davidson, M. Mogri, and K. Deisseroth, "Optogenetics in neural systems," Neuron **71**, 9–34 (2011).

[46] P. A. Lawlor, R. J. Bland, A. Mouravlev, D. Young, and M. J. During, "Efficient gene delivery and selective transduction of glial cells in the mammalian brain by AAV serotypes isolated from nonhuman primates," Mol. Ther. **17**, 1692–1702 (2009).

[47] G. Nagel, T. Szellas, W. Huhn, S. Kateriya, N. Adeishvili, P. Berthold, D. Ollig, P. Hegemann, and E. Bamberg, "Channelrhodopsin-2, a directly light-gated cation-selective membrane channel," Proc. Natl. Acad. Sci. U. S. A. **100**, 13940–13945 (2003).

[48] F. Zhang, L.-P. Wang, M. Brauner, J. F. Liewald, K. Kay, N. Watzke, P. G. Wood, E. Bamberg, G. Nagel, A. Gottschalk, and K. Deisseroth, "Multimodal fast optical interrogation of neural circuitry," Nature **446**, 633–639 (2007).

[49] F. Zhang, M. Prigge, F. Beyrire, S. P. Tsunoda, J. Mattis, O. Yizhar, P. Hegemann, and K. Deisseroth, "Red-shifted optogenetic excitation: a tool for fast neural control derived from volvox carteri," Nat. Neurosci. **11**, 631–633 (2008).

[50] J. Y. Lin, M. Z. Lin, P. Steinbach, and R. Y. Tsien, "Characterization of engineered channelrhodopsin variants with improved properties and kinetics," Biophys. J. **96**, 1803–1814 (2009).

[51] A. Berndt, P. Schoenenberger, J. Mattis, K. M. Tye, K. Deisseroth, P. Hegemann, and T. G. Oertner, "High-efficiency channelrhodopsins for fast neuronal stimulation at low light levels," Proc. Nat. Acad. Sci. **108**, 7595–7600 (2011).

[52] X. Han, "Optogenetics in the nonhuman primate," Prog. Brain Res. **196**, 215–233 (2012).

[53] R. Fork, "Laser stimulation of nerve cells in Aplysia," Science **171**, 907–908 (1971).

[54] J. Wells, C. Kao, E. D. Jansen, P. Konrad, and A. Mahadevan-Jansen, "Application of infrared light for in vivo neural stimulation," J. Biomed. Opt. **10**, 064003 (2005).

[55] A. Izzo, J. Walsh, E. Jansen, M. Bendett, J. Webb, H. Ralph, and C.-P. Richter, "Optical parameter variability in laser nerve stimulation: a study of pulse duration, repetition rate, and wavelength," IEEE T. Bio-Med. Eng. **54**, 1108–1114 (2007).

[56] M. W. Jenkins, A. R. Duke, S. Gu, Y. Doughman, H. J. Chiel, H. Fujioka, M. Watanabe, E. D. Jansen, and A. M. Rollins, "Optical pacing of the embryonic heart," Nat. Photonics. **4**, 623–626 (2010).

[57] J. M. Cayce, R. M. Friedman, E. D. Jansen, A. Mahavaden-Jansen, and A. W. Roe, "Pulsed infrared light alters neural activity in rat somatosensory cortex in vivo," Neuroimage **57**, 155–166 (2011).

[58] N. Fried, S. Rais-Bahrami, G. Lagoda, A.-Y. Chuang, L.-M. Su, and A. Burnett, "Identification and imaging of the nerves responsible for erectile function in rat prostate, in vivo, using optical nerve stimulation and optical coherence tomography," IEEE J. Sel. Topics in Quantum Electron. **13**, 1641–1645 (2007).

[59] J. Wells, C. Kao, P. Konrad, T. Milner, J. Kim, A. Mahadevan-Jansen, and E. D. Jansen, "Biophysical mechanisms of transient optical stimulation of peripheral nerve," Biophys. J. **93**, 2567–2580 (2007).

[60] M. G. Shapiro, K. Homma, S. Villarreal, C.-P. Richter, and F. Bezanilla, "Infrared light excites cells by changing their electrical capacitance," Nat. Commun. **3**, 736 (2012).

[61] J. Yao, B. Liu, and F. Qin, "Rapid temperature jump by infrared diode laser irradiation for patch-clamp studies," Biophys. J. **96**, 3611–3619 (2009).

[62] J. G. Bernstein, P. A. Garrity, and E. S. Boyden, "Optogenetics and thermogenetics: technologies for controlling the activity of targeted cells within intact neural circuits," Curr. Opin. Neurobiol. **22**, 61–71 (2012).

[63] A. C. von Philipsborn, T. Liu, J. Y. Yu, C. Masser, S. S. Bidaye, and B. J. Dickson, "Neuronal control of drosophila courtship song," Neuron **69**, 509–522 (2011).

[64] N. C. Peabody, J. B. Pohl, F. Diao, A. P. Vreede, D. J. Sandstrom, H. Wang, P. K. Zelensky, and B. H. White, "Characterization of the decision network for wing expansion in drosophila using targeted expression of the TRPM8 channel," J. Neurosci. **29**, 3343–3353 (2009).

[65] S. Prahl and S. L. Jacques, "Optical properties spectra," http://omlc.ogi.edu/spectra (2001).

[66] A. Vogel and V. Venugopalan, "Mechanisms of pulsed laser ablation of biological tissues," Chem. Rev. **103**, 577C644 (2003).

[67] T. Durduran, R. Choe, W. B. Baker, and A. G. Yodh, "Diffuse optics for tissue monitoring and tomography," Rep. Prog. Phys. **73**, 076701 (2010).

[68] M. Makale, M. McElroy, P. O'Brien, R. M. Hoffman, S. Guo, M. Bouvet, L. Barnes, E. Ingulli, and D. Cheresh, "Extended-working-distance multiphoton micromanipulation microscope for deep-penetration imaging in live mice and tissue," J. Biomed. Opt. **14**, 024032 (2009).

[69] D. Oron, E. Papagiakoumou, F. Anselmi, and V. Emiliani, "Two-photon optogenetics," Prog. Brain Res. **196**, 119–143 (2012).

[70] B. K. Andrasfalvy, B. V. Zemelman, J. Tang, and A. Vaziri, "Two-photon single-cell optogenetic control of neuronal activity by sculpted light," Proc. Nat. Acad. Sci. **107**, 11981–11986 (2010).

[71] S. K. Mohanty, R. K. Reinscheid, X. Liu, N. Okamura, T. B. Krasieva, and M. W. Berns, "In-depth activation of channelrhodopsin 2-sensitized excitable cells with high spatial resolution using two-photon excitation with a near-infrared laser microbeam," Biophys. J. **95**, 3916–3926 (2008).

[72] P. Theer and W. Denk, "On the fundamental imaging-depth limit in two-photon microscopy," J. Opt. Soc. Am. A **23**, 3139–3149 (2006).

[73] M. Oheim, E. Beaurepaire, E. Chaigneau, J. Mertz, and S. Charpak, "Two-photon microscopy in brain tissue: parameters influencing the imaging depth," Journal of Neuroscience Methods **111**, 29–37 (2001).

[74] M. E. Llewellyn, K. R. Thompson, K. Deisseroth, and S. L. Delp, "Orderly recruitment of motor units under optical control in vivo," Nat. Med. **16**, 1161–1165 (2010).

[75] S. M. Rajguru, A. I. Matic, A. M. Robinson, A. J. Fishman, L. E. Moreno, A. Bradley, I. Vujanovic, J. Breen, J. D. Wells, M. Bendett, and C.-P. Richter, "Optical cochlear implants: evaluation of surgical approach and laser parameters in cats," Hearing Res. **269**, 102–111 (2010).

[76] L. E. Moreno, S. M. Rajguru, A. I. Matic, N. Yerram, A. M. Robinson, M. Hwang, S. Stock, and C.-P. Richter, "Infrared neural stimulation: beam path in the guinea pig cochlea," Hearing Res. **282**, 289–302 (2011).

[77] R. Normann, D. McDonnall, G. Clark, R. Stein, and A. Branner, "Physiological activation of the hind limb muscles of the anesthetized cat using the Utah slanted electrode array," in *Proceedings of IEEE International Joint Conference on Neural Networks* (2005), pp. 3103–3108.

[78] R. A. Normann, B. R. Dowden, M. A. Frankel, A. M. Wilder, S. D. Hiatt, N. M. Ledbetter, D. A. Warren, and G. A. Clark, "Coordinated, multi-joint, fatigue-resistant feline stance produced with intrafascicular hind limb nerve stimulation," J. Neural Eng. **9**, 026019 (2012).

[79] M. L. Rein and J. M. Deussing, "The optogenetic (r)evolution," Mol. Genet. Genomics **287**, 95–109 (2012).

[80] X. Han and E. S. Boyden, "Multiple-color optical activation, silencing, and desynchronization of neural activity, with single-spike temporal resolution," PLoS ONE **2**, e299 (2007).

[81] M. Avermann, C. Tomm, C. Mateo, W. Gerstner, and C. C. H. Petersen, "Microcircuits of excitatory and inhibitory neurons in layer 2/3 of mouse barrel cortex," J. Neurophysiol. **107**, 3116–3134 (2012).

[82] J. Zhang, F. Laiwalla, J. A. Kim, H. Urabe, R. V. Wagenen, Y.-K. Song, B. W. Connors, F. Zhang, K. Deisseroth, and A. V. Nurmikko, "Integrated device for optical stimulation and spatiotemporal electrical recording of neural activity in light-sensitized brain tissue," J. Neural Eng. **6**, 055007 (2009).

[83] A. N. Zorzos, E. S. Boyden, and C. G. Fonstad, "Multiwaveguide implantable probe for light delivery to sets of distributed brain targets," Opt. Lett. **35**, 4133–4135 (2010).

[84] S. Royer, B. V. Zemelman, M. Barbic, A. Losonczy, G. Buzski, and J. C. Magee, "Multi-array silicon probes with integrated optical fibers: light-assisted perturbation and recording of local neural circuits in the behaving animal." Eur. J. Neurosci. **31**, 2279–2291 (2010).

[85] K. Jones, P. Campbell, and R. Normann, "A glass/silicon composite intracortical electrode array," Ann. Biomed. Eng. **20**, 423–437 (1992).

[86] A. Branner and R. A. Normann, "A multielectrode array for intrafascicular recording and stimulation in sciatic nerve of cats," Brain Res. Bull. **51**, 293–306 (2000).

[87] J. Wang, F. Wagner, D. A. Borton, J. Zhang, I. Ozden, R. D. Burwell, A. V. Nurmikko, R. van Wagenen, I. Diester, and K. Deisseroth, "Integrated device for combined optical neuromodulation and electrical recording for chronic in vivo applications," J. Neural Eng. **9**, 016001 (2012).

CHAPTER 2

BACKGROUND AND STATE OF THE ART: LIGHT DELIVERY FOR OPTICAL NEURAL STIMULATION

The desired features and capabilites of an optical neural interface were stated in Chapter 1. This chapter reviews devices and methodologies previously devised and/or used for achieving optogenetic or infrared stimulation of the brain and nerves, *in-vivo* or *in-vitro*. Details on the relevant optics and physiology for neural control are discussed to develop an understanding of the merits and shortcomings of these techniques. A survey of literature reveals that penetrating probes and patterned illumination have almost been mutually exclusive; there are also diverse applications requiring different architectures for effective light transmission.

2.1 Optics for light delivery for neural control

To obtain design targets for an implantable light delivery interface for neural control, one must start with an understanding of how light can be transmitted, how light is propagated in tissue, and the mechanisms for optogenetic and infrared stimulation.

2.1.1 Waveguides

Light is typically transmitted along dielectric waveguides. Common materials for microfabricated waveguides include semiconductors, silica, titanium dioxide, silicon oxynitride, and polymers; characteristics are listed in Table 2.1. Figure 2.1 depicts a step-index waveguide, which consists of a core and a surrounding lower refractive index cladding.

From a simple ray perspective, light travels through the core via total internal reflection

Table 2.1. Materials used for microfabricated waveguides and corresponding properties.

Core material	**Transparency wavelength (λ) range**	**Refractive index (n)**	**Fabrication techniques**	**Application**	**Reference**
Titanium dioxide	0.4–1.5 μm	$n = 2.87$ ($\lambda = 0.4\,\mu m$) $n = 2.45$ ($\lambda = 1.5\,\mu m$)	sputter, dry-etch, nanoimprint	optical interconnects	[1, 2]
Silica	0.2–2 μm	$n = 1.56$ ($\lambda = 0.4\,\mu m$) $n = 1.53$ ($\lambda = 1.5\,\mu m$)	drawing process, etch	optical communications, sensors	[2, 3]
Silicon	1.1–5.5 μm	$n = 3.48$ ($\lambda = 1.5\,\mu m$)	conventional silicon processing	optoelectronics	[2, 4]
III-V	1.2–12 μm	$n = 3.40$ ($\lambda = 1.5\,\mu m$)	chemical vapor deposition, epitaxy	optoelectronics	[2, 5]
Silicon oxynitride	0.2–2 μm	$n \approx 1.46$ to 2.1 as nitride content increases	chemical vapor deposition, sputter	optical communications	[6]
Polymer	$>0.4\,\mu$m	$n = 1.4$ to 1.6	etch, mold, emboss, diffusion	optical interconnects	[7–9]

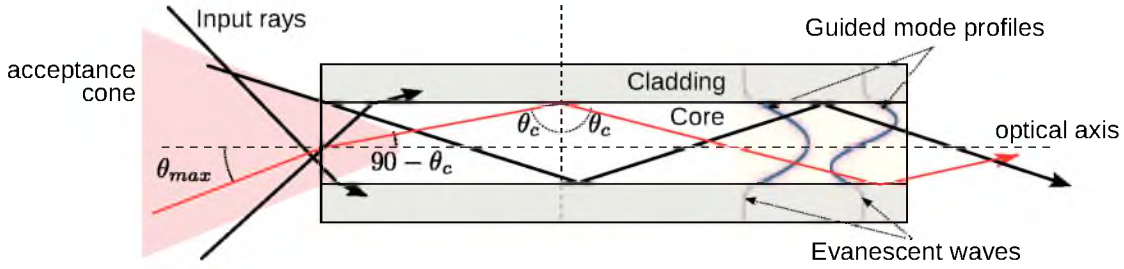

Figure 2.1. An optical waveguide is typically composed of a higher index core material surrounded by a lower index cladding. Multiple rays are transmitted through multimode waveguides, but only rays incident at an angle within the acceptance/emission cone angle θ_{max} will be coupled to/from the waveguide. This ensures total internal reflection (TIR) above the critical angle θ_c at the core-cladding interface. TIR gives rise to guided modes and evanescent waves.

as long as it is reflected off of the core-cladding interface at an angle greater than the critical angle θ_c (see Section 2.1.1.1). Waveguides can be single mode or multimode, meaning that one or multiple rays of light are carried throughout, respectively; multimode waveguides generally have core diameters that are much larger than the transmitted wavelength. Light is also modeled as waves derivative of Maxwell's equations; the wave representation allows determination of the discrete modes permitted within the waveguide. The lowest order mode corresponds to a ray almost parallel to the optical axis and the highest order mode is a ray trajectory close to the critical angle. The modes are established by the wave equation eigenvalue solutions depending on waveguiding parameters such as refractive index, core size and transmission wavelength λ. The approximate number of modes is

$$m = Int[hk_0\sqrt{(n_{core}^2 - n_{clad}^2)}/\pi] \tag{2.1}$$

where h is half of the core thickness and $k_0 = 2\pi/\lambda$. The expression $hk_0\sqrt{(n_{core}^2 - n_{clad}^2)}$ is the V-number that indicates how the waveguide parameters influence the number of modes and provides a general description of the mode cut-off condition. The guided modes are standing waves within the core with power exponentially decaying into the cladding; the decaying tail of the waves are referred to as evanescent waves. A higher contrast between the core and cladding refractive indices maximizes power confinement in the core. Mode profiles in the y-plane may be described mathemetically as

$$E_y = \begin{cases} Ae^{-\gamma(x-h/2)} & x \geq h/2 \\ A\frac{\cos \kappa x}{\cos \kappa h/2} \text{ or } A\frac{\sin \kappa x}{\sin \kappa h/2} & -h/2 \leq x \geq h/2 \\ \pm Ae^{\gamma(x+h/2)} & x \leq -h/2 \end{cases} \tag{2.2}$$

in a symmetric waveguide with $x = 0$ along the optical axis, where A is the amplitude, h is the core thickness, κ is the tranverse wavevector, and γ is the wave attenuation (i.e., decay) coefficient in the cladding. Figure 2.1 shows the lowest even (cosine) and odd (sin) modes within the waveguide core with evanescent waves decaying into the surrounding cladding. Note that the existence of evanescent waves provides the physical continuity of electric and magnetic fields at the boundary during total internal reflection; it does not give a net power flow in the x-direction.

2.1.1.1 Coupling into step-index multimode waveguides

High efficiency coupling between waveguides, or sources and waveguides, is especially important for light delivery in deep-tissue to prevent surface heating. Factors to consider during coupling include the numerical aperture (NA), aperture and/or beam area, misalignment, and reflection losses at the interface. Figure 2.2 illustrates the typical sources of coupling loss.

First, the waveguide can only accept or emit light that is incident over a limited range of angles characterized by the numerical aperture

$$NA = n_{core} \sin \theta_{max} = \sqrt{n_{core}^2 - n_{clad}^2}\,, \tag{2.3}$$

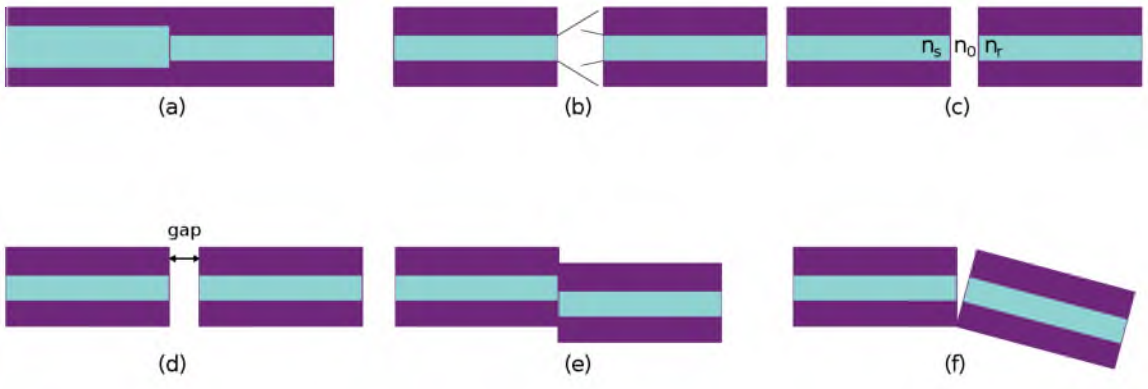

Figure 2.2. Coupling losses may arise from (a) core size mismatch, (b) numerical aperture mismatch, (c) refractive index mismatch, (d) end separation, (e) lateral misalignment, or (f) angular misalignment.

where θ_{max} is the half-angle of the acceptance/emission cone, and n_{core} and n_{clad} are the core and cladding refractive indices. The NA is visualized as an acceptance cone in Figure 2.1. Rays entering the waveguide at angles greater than the cone do not meet the critical angle θ_c requirement between the core and cladding. The values of θ_{max} and θ_c are both determined from Snell's Law,

$$n_i \sin\theta_i = n_t \sin\theta_t, \tag{2.4}$$

where n and θ are the refractive index and incidence angle with respect to the optical axis (i.e., line of propagation direction) in the incident (i) or transmitting (t) media. The transmitted angle reaches 90° when the incident angle is increased sufficiently, beyond which light cannot be transmitted across the interface. The critical angle for total internal reflection in a waveguide is then computed as $\theta_c = \sin^{-1}(n_{clad}/n_{core})$; note that this dictates that the core refractive index must be larger than that of the cladding for total internal reflection to occur. The θ_c is traced back to the input interface to calculate the maximum acceptance angle as $\theta_{max} = \sin^{-1}[(n_{core}/n_0)\sin(90 - \theta_c)]$ with n_0 as the refractive index of the medium surrounding the waveguide at the input interface (e.g., air). For lossless coupling with $\eta_{NA} = 1$, the numerical aperture of the source waveguide must be smaller than that of the receiving waveguide, $NA_s < NA_r$ (i.e., emitted cone is narrower than acceptance cone). The coupling efficiency with NA mismatch is

$$\eta_{NA} = (NA_r/NA_s)^2, \eta_{NA} = NA_s > NA_r. \tag{2.5}$$

Aside from the NA, the aperture area (i.e., opening through which light is emitted or accepted) of the source must also be smaller than that of the receiving waveguide, $a_s < a_r$, to collect all light. Otherwise, the maximum coupling efficiency given an area mismatch is

$$\eta_{area} = a_r/a_s,, \qquad a_s > a_r. \tag{2.6}$$

Fresnel reflection loss also decreases the efficiency in cases where the source and receiving waveguides have different core refractive indices or are not in physical contact, as in Figure 2.2c. The efficiency accounting for Fresnel loss when there is physical contact is

$$\eta_{ref} = 1 - \left(\frac{n_s - n_r}{n_s + n_r}\right)^2. \tag{2.7}$$

If a gap is present, this coupling efficiency equation is applied twice to include both source and receiving interfaces such that

$$\eta_{ref,gap} = \left[1 - \left(\frac{n_s - n_0}{n_s + n_0}\right)^2\right]\left[1 - \left(\frac{n_0 - n_r}{n_0 + n_r}\right)^2\right]. \tag{2.8}$$

End separation will result in further loss when the source light beam is diverging. Although the core area and NA may be matched between source and receving waveguide, the beam is broadened such that the area a_s' at the receiving interface is considered in the coupling efficiency instead

$$\eta_{end} = a_r/a_s'. \tag{2.9}$$

A longer end separation causes a wider beam at the receiving interface.

Lastly, mechanical misalignment influences the coupling efficiency as it evidently prevents "line of sight" transmission of all light power from one waveguide to another. Lateral misalignment leads to coupling efficiency equal to the overlapping area of the cores

$$\eta_{lat} = a_{rs}/a_s, \tag{2.10}$$

where a_{rs} is the area of overlap between the source and receiving cores. For example, two congruent square waveguides with thickness t and optical axes displacement d in one direction will have $\eta_{lat} = t(t-d)$. On the other hand, angular misalignment yields a maximum efficiency of

$$\eta_{ang} = 1 - \frac{n_0\phi}{\pi NA} \tag{2.11}$$

found by computing the overlap of the transmitting and receiving cones with n_0 as the interface medium refractive index and ϕ as the angle between the optical axes.

The overall coupling efficiency is the product of all efficiency factors in consideration. To summarize the preceeding discussion, a source may be coupled into the waveguide with minimal losses if:

(a) source NA is less than waveguide NA,

(b) source aperture is less than the area of the waveguide core,

(c) source and waveguide optical axes are aligned and in physical contact,

(d) source and waveguide index of refraction is matched or input interface has antireflection coating.

2.1.1.2 Lensed coupling into multimode waveguides

Coupling through converging lenses is a common method to achieve high efficiency coupling. Lens images are mostly described by geometric optics from where the thin lens equation is derived as

$$\frac{1}{f} = \frac{1}{t_i} + \frac{1}{t_o}, \tag{2.12}$$

or as $(t_o - f)(t_i - f) = f^2$ in the Newtonian form. The variables are depicted in Figure 2.3. The object and image distance from the lens is t_o and t_i, respectively; the distance between the lens and its focal point is the focal length f. The image location occurs at the intersection of the ray traces that are drawn according to the fundamental rules of lens imaging:

(a) A light ray parallel to the optical axis will pass through the focal point located at a distance f from the vertex of the lens on the other side.

(b) A light ray through the center of the lens will pass straight through undeviated.

(c) A light ray through the focal point will be refracted parallel to the optical axis on the other side of the lens.

Thus, a collimated beam (i.e., beam consisting of rays parallel to the optical axis due to an object at an infinite distance) will be focused to a spot at the focal point, although the smallest focused spot radius is actually diffraction limited at $1.22\lambda f/d$ with d as the lens diameter. On the other hand, a point source of light at the focal point will be converted into a collimated beam by the lens. If the object is placed closer to the lens than the focal length, an upright virtual image is apparent on the same side; light rays diverge on the other side upon refraction such that the image location can only be found by extending the refracted rays backwards to form an intersection on the object's side of the lens. If the object is placed farther from the lens than the focal length, as in Figure 2.3, an inverted real image may be projected onto a screen at the other side; the image is smaller or larger than the object when the object is positioned $>2f$ or between f and $2f$ away from the lens, respectively. The lens magnification is simply the ratio of the image to object length (i.e., imaged beam diameter to initial beam diameter), which consequently leads to

$$M = t_i/t_o. \tag{2.13}$$

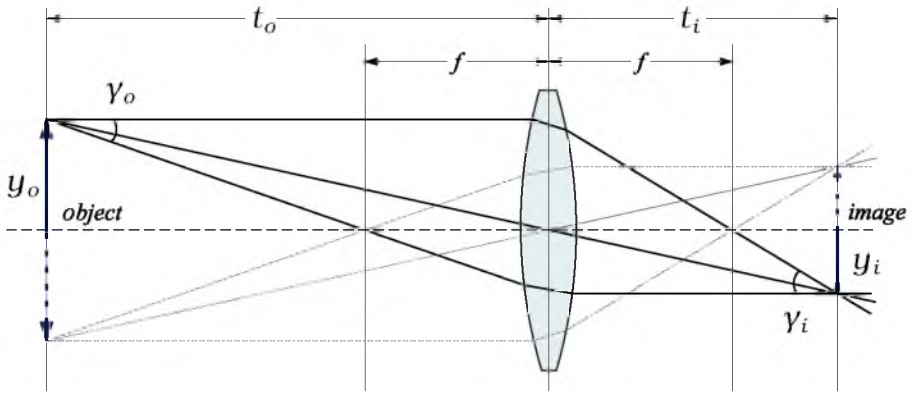

Figure 2.3. Geometry for derivation of the thin lens equation.

For lossless coupling or imaging, the limit for the object-to-image size reduction is dictated by the Abbe sine condition $y_o \sin(\gamma_o) = y_i \sin(\gamma_i)$. When a circular light souce with area $a_s = \pi y_o^2$ and numerical aperture $\mathrm{NA}_s = \sin(\gamma_o)$ is used and mapped on an area $a_r = y_i^2$ with $\mathrm{NA}_r = \sin(\gamma_i)$, the smallest possible image area is

$$a_{r,min} = a_s \frac{NA_s^2}{NA_r^2}. \tag{2.14}$$

In addition, $\mathrm{NA}_r < 1$ because $\gamma_i < 90°$, and thus $a_{r,min} \geq a_s NA_s^2$. Note that this equation imposes lossless imaging that is limited at least by the product of the initial beam area and the square of its numerical aperture, which is a combination of Equations 2.5 and 2.6 for maximum coupling efficiency.

2.1.2 Beam propagation in tissue

A beam traveling in tissue loses its power from absorption and scattering, as briefly discussed in Chapter 1. Again, the absorption and scattering properties, which constitute the overall attenuation, vary with wavelength and tissue composition. Figure 2.4 plots light attenuation in mouse brain, derived from adding scattering data to the absorption data of characteristic components (e.g., water, blood, lipid) [2, 10–15]. Rodent brain/nerve is the most widely-used tissue model for optical neural control. A simplified mathematical model of the transmission of light in a medium is the Beer–Lambert law

$$T = e^{-\alpha L}, \tag{2.15}$$

where T is the fractional power, α is the attenuation coefficient in distance^{-1} units and L is the distance traveled by light. This leads to the low fraction of incident light at the point 100 μm deep along the optical axis in mouse brain, as shown in Figure 2.4 as well. Note that the fractional power is an exponential function of depth; it is evident that light can only be transmitted within micrometers below the tissue surface. Here, blue light at 470 nm is seen to have roughly 100 μm $1/e$ (i.e, 37%) penetration depth. A more classical yet relaxed measure of the extent of light transmission is the $1/e^2$ (i.e., 13.5%) penetration depth, beyond which an increase in incident intensity results in marginal increase of the local intensity.

Fractional power vs. depth is a one-dimensional measure that does not give information on the beam spread (i.e., lateral distribution) in 3D tissue. A 2D intensity profile of the beam propagation, which can be extended to 3D, provides more insight into the effective illumination volume by indicating contours of fractional power. The 2D profile is especially influenced by scattering, which in turn is dictated by the inhomogeneity of tissue. Because tissue components (e.g., cells) are of comparable size to visible-IR wavelengths, scattering is mostly in the forward direction. The concept of *transport* scattering length (l_t) indicates where scattering becomes truly random; it is computed from $l_s/(1-g)$, where the scattering length l_s is the average distance between scattering events and g is the anisotropy of tissue

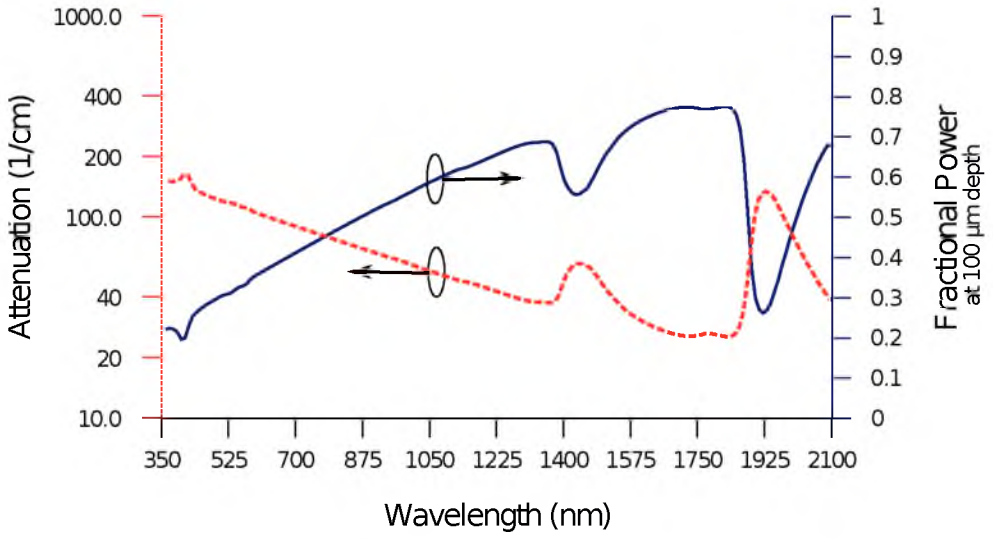

Figure 2.4. Estimated attenuation of visible light and fractional power at 100 μm deep in mouse brain (adapted from data in [13, 14]).

taking on a value between 0 and 1. Highly anisotropic media (i.e., $g \approx 1$), where particle sizes are large, cause the intensity distribution to extend in the forward direction with light straying from the optical axis at smaller angles. For example, brain tissue scattering length is 50–200 μm from the blue to NIR range and anisotropy is high at ~0.9, which leads to l_t of 0.5–2 mm [13, 16]. Models have been formulated to estimate the 2D profile, mostly applying Monte Carlo analysis [17–19]. Simulation results closely match actual measurements in tissue [19, 20]. Figure 2.5 illustrates examples of 2D profiles of beam propagation in tissue on the X-Y plane at Z = 0 and Y-Z plane at X = 0 (X-Y is the plane perpendicular to the propagation, Z is the propagation direction).

The limit of light transmission may be delineated at the $1/e^2$ contour of the intensity profile to be congruent with the definition of the $1/e^2$ penetration depth. For each infinitesimal X-Y plane, the profile more or less follows the gaussian distribution illustrated in Figure 2.6(a), with a beam width $2w$ taken as the diameter where $1/e^2$ intensity occurs. In the Y-Z plane, the beam divergence (i.e., increase in beam width) conforms to a gaussian beam propagation as well; Figure 2.6(b) shows the gaussian beam spread and the parameters relevant to this work. True gaussian beams propagate as

$$w(z) = w_0 \sqrt{1 + \left(\frac{z}{z_R}\right)^2} \tag{2.16}$$

with

$$z_R = \left(\frac{\pi w_0^2}{\lambda}\right), \tag{2.17}$$

where w is the radius of the $1/e^2$ contour along the propagation distance z, w_0 is the beam waist (i.e, smallest beam radius at $z = 0$), z_R is the Rayleigh distance, and λ is the operating wavelength. Note that for a multimode Gaussian-like beam, which is typically the case, Equation 2.17 does not strictly hold. The "Rayleigh distance" does not necessarily depend on the beam waist, but a divergence length can be defined as a multimode analogue to the Rayleigh length, which is the distance at which the starting beam width increases by a factor of $\sqrt{2}$. Beyond the divergence length, the beam spreads with a full-angle divergence ϕ. An M^2 factor is often defined to denote how the actual beam form compares to the ideal gaussian

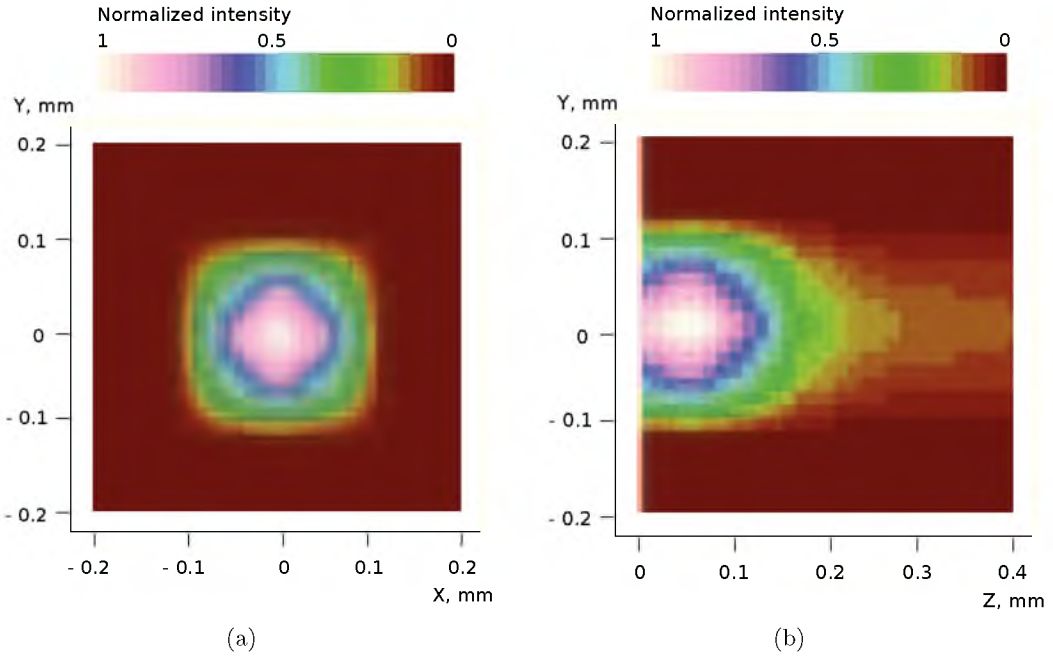

Figure 2.5. Example of 2D intensity profiles in tissue perpendicular (a) and parallel (b) to beam propagation.

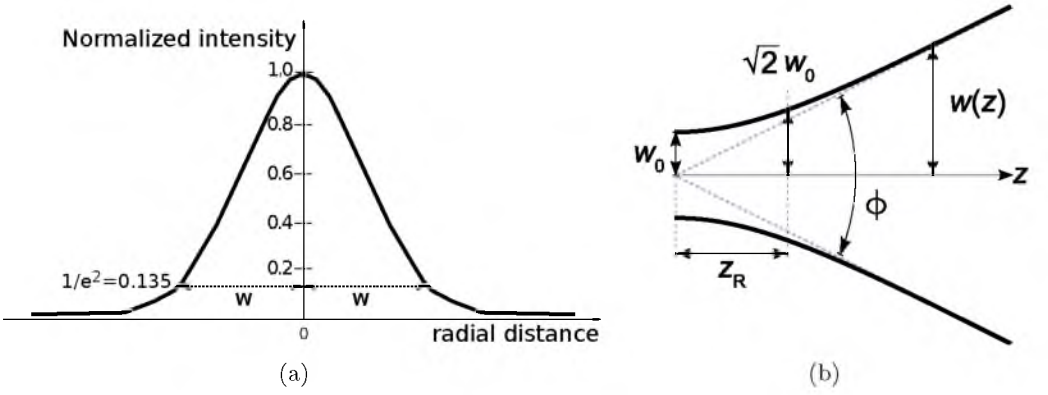

Figure 2.6. Gaussian intensity profile (a) and beam spread (b). The beam width $2w$ is the diameter where normalized intensity falls to $1/e^2$. The initial beam width w_0 increases by $\sqrt{2}$ at the Rayleigh distance z_R along the propagation, beyond which the beam diverges at a full angle ϕ.

beam; the ideal gaussian beam has an M^2 factor of exactly one. Multimode gaussian-like beams contain a gaussian function in the mathematical models; the true beam width is M times smaller than that of the multimode beam diameter and the divergence is M times greater.

2.2 Tissue damage threshold due to light exposure

Excessive amounts of incident light onto tissue causes heating that raises the ambient temperature of the cells. Tissue damage progresses with increasing temperature [21, 22]. At the body temperature of 37°C, cells are considered functional, but a change to 41°C inititates structural breakdown. When the temperature is further increased to 45°C, the irreversible process of protein denaturation occurs, which disrupts cell activity. At 60°C, soft tissue is converted into a dry mass as a result of coagulation. When water starts to evaporate at 100°C, the tissue is vacuolated (sponge-like) due to the steam. Beyond this, tissue charring and vaporization can be observed.

A 1°C increase in rat sciatic nerve temperature by exposure to 1.87 μm infrared light can be driven by an additional 0.04 J/cm^2 [22]. Damage thresholds for infrared stimulation have been quantified as fluence levels where observable tissue ablation occurs [23]. For infrared wavelengths with an optical penetration depth between 1 μm and 0.5 cm, fluence values in the range 0.4 to 7 J/cm^2 result in tissue ablation [22, 24].

In optogenetics, damage thresholds were defined as intensity levels. With optogenetic light sources, up to $\approx$75 mW/mm^2 of incident beam intensity has been determined safe for in-vivo experiments when using short laser pulses of about 0.25 to 50 ms duration [25, 26]. For continuous illumination that allows 400 pA of opsin-mediated current, an intensity of less than 20 mW/mm^2 at the target cell is recommended to avoid phototoxicity [27].

2.3 Mechanism of optical stimulation

Infrared neural stimulation (INS) is based on the photothermal effect of light absorption of water in neural tissue [22, 28]. Infrared light induce currents that track the resulting temperature rise from pulsed irradiation; transient local heating changes the membrane electrical capacitance that disturbs the balance of ions, thereby producing currents. The tissue temperature linearly increases rapidly during the laser pulse and slowly decays ex-

ponentially with a heat relaxation time consistent with that of water. It then follows that effective irradiation requires an optimum exposure time, when maximum heat is confined within the target [21]. The concept of thermal relaxation time τ_r functions as the ceiling of exposure duration; it is loosely defined as the time to dissipate a fraction of the heat absorbed by tissue during a laser pulse. The value of τ_r(ms) depends on the wavelength, desired penetration depth, heat diffusion, and the tissue thermal diffusitivity. Wavelengths for INS used today have ∼300–500 μm penetration depth—1450, 1875, and 2120 nm.

On the other hand, optogenetics is completely dependent on the properties of light-sensitive ion channels expressed in the cell wall. Only transduced cells will respond to light stmuli and cause direct hyperpolarization (i.e., inhibition) or depolarization (i.e., excitation) via ion flow. The following are common opsin-based photosensitive ion channels with corresponding activation wavelengths [27]:

(a) channelrhodopsin-2 (ChR2; excitatory) - 470 nm,

(b) *Volvox cateri* channelrhodopsin-2 (VChR2; excitatory) - 545 nm,

(c) halorhodopsin (NpHR; inhibitory) - 570 nm,

(d) archaerhodopsin-3 (Arch; inhibitory) - 566 nm.

Other optogenetic tools are derived from these fundamental rhodopsin channels, possibly with activation spectra shifted (e.g., eNpHR3.0 is a modified NpHR with activation wavelength of 590 nm).

2.3.1 Activation thresholds

Observed activation thresholds for infrared and optogenetic stimulation of neural actitivity are listed in Tables 2.2 and 2.3, respectively. The activation threshold must be lower than the damage threshold value as it defines the minimum light intensity/fluence delivered to tissue for evoking action potentials. The conventional unit for INS threshold is fluence (J/cm^2) on account of pulsed input typically being used. The threshold is found to be invariable with input pulse width/duration if the threshold is taken as the minimum radiant exposure needed to observe an action potential, regardless of the amplitude [22]. When an action potential amplitude is defined with the threshold fluence, the smallest value is taken because the threshold just increases with longer pulse durations, which is

likely due to decreasing thermal confinement [21, 29]. Meanwhile, there is no consensus on optimal input pulse frequency. Note that INS has always been characterized extraneurally (i.e., from outside neural tissue) such that threshold fluence largely depends on the species and tissue even when operating at the same wavelength. Light would have to get past any deterrent structure to the target region inside the tissue (e.g., epineurium or axons in outer regions of peripheral nerve) and a temperature rise specific to the physiology would have to be reached [22, 30, 31]. For example, Table 2.2 lists wavelengths that exhibit precise tissue optical penetration depth, and it indicates a lower activation fluence for thinner gerbil cochlear nerve than thicker facial nerves. Similarly, wavelengths with shorter penetration depths recruit fewer neurons and generate minimum action potential peaks, while wavelengths with sufficiently longer penetration depth lead to increased responses due to access to a larger number of neurons deeper in tissue [24, 31, 32].

In optogenetics, the conventional unit for excitation/inhibition threshold is intensity (mW/mm^2); input light may be continuous or pulsed. Details on the stimulus duration or frequency are not always reported in literature, and the same is true for the illumination volume or at least the incident beam size. Moreover, there are a number of different definitions for the threshold irradiance as seen in Table 2.3; benchmarks include irradiance at single spike occurrence or irradiance producing 1 Hz spike rate for ChR2, and irradiance for 100% suppression for NpHR [14, 19, 33]. In general, the activation threshold increases with lower rhodopsin expression levels and sparser distribution for the same target volume [34]. Expression levels differ among animal models and gene-delivery methods, while the distribution depends on the cell type or neural network being investigated [34, 35]. The threshold is also influenced by the rhodopsin type and its kinetics.

2.3.2 Illumination volume specifications

The required illumination volume is essentially dictated by the size of the target tissue component/structure. Neuroscience research commonly utilizes the mammalian neocortex, which has six layers of histologically and functionally distinct cells; the relative thickness of each layer varies with the animal model and the region of the cortex (e.g., sensory vs. motor). The cortex is also divided radially into columns that are 200–500 μm in diameter

Table 2.2. Threshold radiant exposure for evoking compound action potentials with *extraneural* infrared neural stimulation.

Species	**Site**	**Wavelength (nm)**	**Threshold fluence (J/cm^2)**	**Spot width (μm)**	**Pulse rate (Hz)**	**Reference**
Rat	sciatic nerve	2120	0.32	~800	<5	[23, 24]
		1870	0.32	~1200	<5	[22]
	thalamocortex	4400	0.19	350 ± 50	30	[36]
		3650	0.2	350 ± 50	30	[36]
	somatosensory cortex	1870	0.14	2000	200	[37]
	cavernous nerve	1873	~1.0	1000	10	[38]
Gerbil	cochlear nerve	2120	~0.018	~100	2	[32]
	spiral ganglion	1855	~0.005	310	2	[39]
	facial nerve	2120	0.71	>600	2	[31]
Cat	cochlear nerve	1860	~0.015	200	10	[40]
Frog	sciatic nerve	2120	~0.9	~1200	<5	[22]
Quail	embryonic heart	1875	~0.8	~620	2	[29]

Table 2.3. Threshold intensity I with optogentic stimulation (illumination volume and duration not thoroughly documented).

Species	**Site**	**Rhodopsin type**	**Threshold I (mW/mm^2)**	**Threshold definition**	**Illumination method**	**Reference**
Mouse	cortex	ChR2	1	occurrence of spike	implanted 200 μm fiber	[19]
	hippocampus	NpHR	21.7	~100% spike suppresion	microscope	[33]
	cortex	Arch	3	~100% spike suppresion	implanted 200 μm fiber	[41]
Rat	hippocampal slice	ChR2 (wild-type)	42	80% success (1 Hz stimuli)	microscope	[42]
		ChR2 (H134R)	23	80% success (1 Hz stimuli)	microscope	[42]
		ChR2 (T159C)	6.7	80% success (1 Hz stimuli)	microscope	[42]
		ChR2 (ET/T159C)	6.7	80% success (1 Hz stimuli)	microscope	[42]
Cat	visual cortex	ChR2	190	spike at 1 mm away	200 μm fiber	[34]
			7	spike at 0.1 mm away	200 μm fiber	[34]
Monkey	cortex	ChR2	2.6	at 1 Hz spike rate	implanted 200 μm fiber	[14, 43]

consisting of several thousand neurons perpendicular to the cortical layers. Columns are interconnected functional units, where member neurons respond to or produce the same characteristic. Desired stimulation volumes may involve illuminating a single cell, a region within a one cortical column in a specific layer, one cortical column through all layers, or an entire cortical layer. For neuroprosthesis, the peripheral nervous system is also of significant interest. In vertebrates, the whole nerve is wrapped in the epineurium, which is a connective tissue sheath. Within the nerve, several fascicles (i.e., bundles) contain axons (i.e., fibers) encased in another connective tissue sheath called the perineurium. Each individual axon is further surrounded by a thin connective tissue sheath called the endoneurium. The illumination volume for selective graded optical neural control of the nerve ideally bypassed the connective sheaths and corresponds to individual neurons or small subpopulations. Figure 2.7 illustrates examples of neural tissue dimensions that may be selectively addressed for various applications [44–48].

Especially in optogenetics, it has become a common notion in literature that the stimulation volume is bounded by the activation threshold [19, 27, 34, 49, 50]. It is true that the volume illuminated with local energy/power levels more than the activation threshold will respond to stimulation, but coinciding the threshold contour with $1/e^2$ fluence/intensity boundary (overview given previously in section 2.1.2) might be a more practical measure of the maximum effective illumination volume to prevent arbitrary amplification of input levels that only weakly extend the stimulation range at the cost of damaging near-surface regions. This volume is measured around the emission point or plane in tissue; if target structures are well beneath the surface, invasive light delivery should be considered to create localized stimulation.

2.4 Light delivery in tissue

The methods by which light at the activation threshold values are delivered into the required illuminations volumes are discussed in this section.

2.4.1 Light delivery for infrared neural stimulation

In-vitro and acute *in-vivo* experiments on INS have been performed to investigate the stimulation parameter space, study the activation mechanism, or demonstrate the suitability

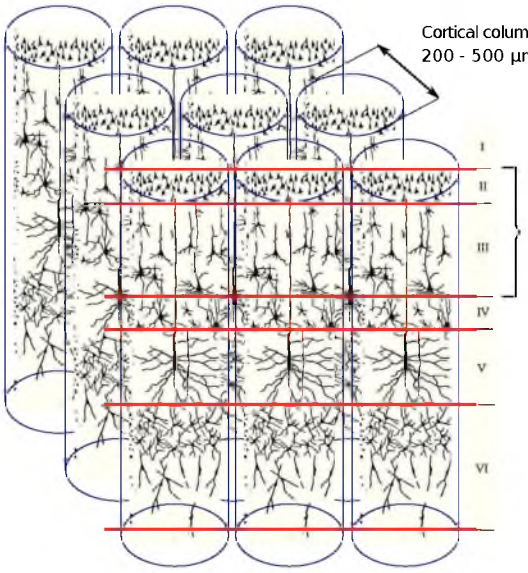

Layer thickness (µm)

Human	Gorilla	Chimp	Macaque	Dog	Ferret	Cat	Rat	G. Pig	Mouse
700	600	500	500	300	100	300	100	100	50
1300	1300	1100	1000	700	700	600	500	450	400
200	200	150	150	100	200	150	100	150	50
500	450	400	400	400	300	250	500	500	300
450	450	400	500	400	300	300	300	450	200

(a)

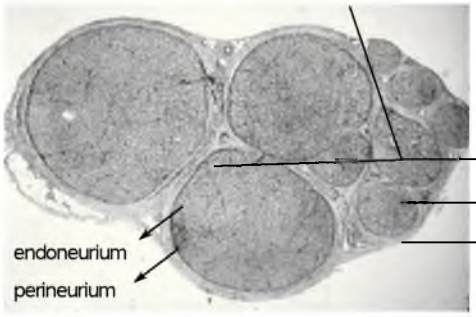

Diameter / thickness (µm)

	Human	Cat	Rat
nerve	25000	4000	2000
fascicle	2000 - 5000	500 - 1500	400 - 800
axon	10 - 25	5 - 20	1 - 10
epineurium		200	50

(b)

Figure 2.7. Schematic of neural structures that are of interest in optical neural control (not to scale): sensory cortical layers with data for 10 species (a) and sciatic nerve with data for 3 species (b). Dimensions must match the volume of illumination from light delivery, which is practically limited by the $1/e^2$ fluence or intensity contour. Invasive light delivery should be considered for structures well beneath the tissue surface to create localized stimulation. Adapted from [44, 45, 48].

of this new modality for various applications (e.g., prosthesis, diagnostics). To date, only noncontact (i.e., noninvasive) light delivery has been pursued, typically accomplished using an optical fiber to illuminate a single spot on the tissue surface.

The initial proof-of-concept and characterization experiments coupled light from a free electron laser into a 500 μm wide hollow waveguide, which was affixed 0.75 mm above exposed rat sciatic nerve [23, 24]. With this stimulation system, the resulting spot size on the nerve exterior was determined as 0.6 mm^2 (i.e., $\sim$870 μm in diameter). Subsequent tests by the same pioneering group utilized a similar spot size from a 600-μm fiber connected to sources such as fiber-coupled Holmium:yttrium aluminum garnet (Ho:YAG) and Capella diode lasers (Lockheed Martin Aculight, Inc.; 1865–1879 nm output wavelength from a 400 μm aperture at tunable pulse energies, widths and rates) [22, 30]. Irradiation of infrared light onto tissue using portable fiber-coupled lasers also proved succesful in the stimulation of brain slices [37], auditory neurons and system [32, 39, 40, 51], facial nerves [31], vestibular system [52], cavernous nerves [38], and heart pacing [29]. All these applications aim to exhibit high spatial selectivity; an investigation of the optimum incident beam size and its spread in tissue for various stimulus parameters and tissue properties (e.g., optical, composition, geometry) is then imperative. To this end, light absorption and temperature profiles in the cochlea introduced by beams from different optical fibers (e.g., varying diameter, NA) have been modeled [53, 54], and the effect of the beam path orientation on stimulation efficacy and location has been experimentally evaluated [55]. Optical beam profiles from an optical fiber were measured in different media relevant to facial nerve stimulation [31]. These set the stage for further understanding of the INS mechanism, stimulation threshold energy, and illumination volume. A more comprehensive experimentation on beam delivery is expected to open up employment of novel optical sources and waveguide systems that will especially benefit INS prosthesis.

2.4.2 Light delivery for optogenetics

Devices and mechanisms for delivering light vary widely with optogenetics as there are many experimental paradigms encompassing different animal models, neural circuits, target cells, time frames, aims, etc. Prominent techniques for visible light transmission onto/into

tissue for optogenetic experiments are listed on Table 2.4. Microscopy tools, optical fibers, light-emitting diodes, modulators, and custom-microfabricated light sources and waveguides are among the reported methods in literature that are discussed in this section.

2.4.2.1 Noninvasive widefield illumination

Transmitting light to an exapanse of tissue (e.g., whole soma, cortical layers, brain section) is especially useful when transduced targets are sparse and/or high-level area-specfic functions are observed [27, 56]. In the simplest protocol, entire cell cultures and tissue slices in a petri dish undergo flood-illumination, typically through widefield microscopes [56–59]. Aside from the technical simplicity, there is capability of utilizing fluorescence imaging for simultaneous optical recording. *In-vivo* noninvasive illumination through a cranial window has also been achieved with microscopy [60], as well as with an optical fiber [61, 62]. Although tissue is not physically disturbed with noninvasive stimulation in live animals, observation is limited to near-surface structures and responses; upper layer structures must be set aside to expose the underlying tissue of interest, which defeats the purpose of noninvasive light delivery. Increasing the incident intensity may cause enough intensity levels at the desired depth, but upper layers will also be stimulated and will likely be damaged. Two-photon excitation is then used if the target is located along a plane below the tissue surface [63–66]; this allows the stimulation intensity to be transmitted and confined within that subsurface plane. However, even with two-photon excitation using 900–920 nm wavelengths (i.e., low absorption window) for ChR2 excitation, optical access was limited to as deep as 240 μm into tissue [63].

2.4.2.2 Penetrating probes

The need to access targeted cells deep into tissue without damaging precedent tissue led to the ultilization of penetrating probes for most *in-vivo* optogenetic experiments. The advantages offered by such structures are are already recognized [19, 67, 69]. Like INS, light has most commonly been delivered via an optical fiber using a fiber-coupled light source [35]. In fact, the first optogenetic neural interface is a 200-μm multimode fiber inserted through a cannula guide [19]. This type of interface was successfully employed in chronic tests with freely moving mice to photostimulate deep brain structures in microsized

Table 2.4. More prominent examples of light delivery methods for optogentic neural control. In theory, these can be one or two-photon stimuli at various/multiple wavelengths with further coupling and emission profile control using additional lenses.

	Optical source/interface	**Illumination volume/area control**	**Patterning**	**Remarks**	**Reference**
Non-invasive, single-spot	microscope	objective NA & magnification; aperture	-	typical for sparse targets, with fluorescence imaging capability	[56]
	optical fiber	NA, size & tip shape	-		[61]
	two-photon	dependent on delivery method (fiber/microscope)	-	higher lateral/axial resolution, deeper transmission	[63, 64]
Penetrating waveguide	optical fiber	NA, size & tip shape		deep-tissue transmission, typically through cannula	[19, 67, 68]
	fiber-electrode assembly	fiber NA, size & tip shape; electrode recording site distance	limited with use of linear electrode arrays	with electrical recording capability, stimulus artifact possible, deep-tissue transmission	[50, 69, 70]
	microfabricated probe	geometry upon fabrication	limited in linear dimension if more than one waveguide is fabricated	deep-tissue transmission, with electrical recording capability if adjacent electrode is fabricated	[71–73]
On-surface patterns	scanning microscope	objective NA & magnification; aperture	pseudorandom, sequential	with fluorescence imaging capability	[60, 74]
	spatial light modulator	geometry	arbitrary	optical source needed	[75–77]
	μLED	geometry; intensity	arbitrary		[78]
	μECoG	geometry	arbitrary	optical source needed, with electrical recording capability	[79]
Deep-tissue patterns	microfabricated waveguide array	geometry upon fabrication	arbitrary	light source may be external or mounted	[80, 81]

volumes [19, 82, 83]. A tungsten electrode can also be glued to the fiber to electrically record proximate activity [84, 85]. Fiber-multielectrode probes were later formed by surrounding microwires around the optical fiber within the cannula [68, 86].

Optical fibers were tapered in subsequent implementations to minimize neuronal damage, thus allowing smooth implantation without the cannula. One of the optical neural interfaces in use today consists of a sharpened 50-μm fiber inserted at a central position within a commercial Utah electrode array [67], which has had a demonstrated chronic implant lifetime of eight months [87] in the neocortex of a transgenic rat; optogenetic excitation in one cortical locality was possible along with the electrical monitoring of the response spread across the surrounding sites.

Spatially-multiplexed photoactivation over multiple sites may be achieved by integrating optical fibers to microelectrode devices that facilitate both implantation and recording. Linear microwire arrays [70] and planar silicon probes [69, 88] of the Michigan architecture (i.e., multiple recording sites along the perimeter of the tip of a single probe) [89] have been used for this purpose, but offer limited selective manipulation and comprehensive monitoring of the activity of individual neurons. In addition, true patterned stimulus transmission requires independent light sources, which becomes impractical with external lasers connected to bulky fiber bundles. A linear array of six 50-μm tapered fibers individually coupled to lightweight diodes was presented as a partial solution and demonstrated spatiotemporal stimulation in a behaving rat [50]. Nevertheless, it has been observed that some fiber-electrode assemblies cause light-induced electrical artifacts that can obscure local field potential and spike recordings; artifacts may be due to a photovoltaic effect from direct interaction between light and metal when immersed in tissue, but have not been investigated in detail [25, 43, 90].

Characterizing the spatial extent of illumination in tissue may help avoid generation of artifacts and more importantly evaluate the aptness of optical fiber output beams for the different optogenetic experiments. If the emanation point of light is placed a distance away from the recording site such that it experiences an intensity level below threshold, stimulus artifacts are then less likely to occur [25, 68, 69]. A thorough cataloging of quantitative estimates of illumination profiles produced by different optical fibers also

gives information on which waveguide properties are appropriate for confined control of specific neuronal/cellular organizations or processes (e.g., a neocortex layer, cholinergenic signaling). The initial beam size, power, and pulse duration may also affect the range of recruitment [34, 49]. Illumination volumes translate into stimulation volumes once the optogentic tools and tissue optical properties are considered. Fiber size, numerical aperture and tip taper, source intensity and wavelength, and tissue type define the volume of tissue recruited during optogenetic experiments [19, 27, 50, 67, 70].

Microfabricated waveguides have also been introduced as customized alternatives to optical fiber neural interfaces. In most devices, an optically transparent material was essentially deposited on a planar silicon neural probe to form straight waveguides running along the electrode. Silicon nitride [71], poylmer (e.g., SU-8) [72, 91], and silicon carbide [92] were used as waveguide core. An optical neural probe without electrical recording capabilities has been surface-micromachined as well [73]. It consists of twelve parallel independent single-mode rectangular waveguides of silicon oxynitride core and oxide cladding that converge into a single probe. Each waveguide ends at a particular target depth with a corner aluminum mirror to perform side-firing; waveguide bending and >5 cm length leads to a low 23 to 33% transmission efficiency with emission profiles undetermined.

2.4.2.3 Two-dimensional patterned illumination

As has been consistently pointed out, precise control of the temporal and spatial distribution of stimulus light allows orderly selective manipulation of neuronal activity in a comprehensive area of tissue. Thus, complex high resolution photoactivation methods have been established with optogenetics, albeit typically limited to volumes near the tissue sample surface. One technique that has been easily adapted to optogenetic experimentation is scanning microscopy (one or two-photon), where light beams are delivered through the objectives. Several works on functional mapping of the cortex took advantage of the rasters or pseudorandom sequences that can be performed by scanning microscopes [59, 60, 74, 93]. Sequential illumination at various spots on the sample was also accomplished by using a point-scanning stage placed under a single collimated beam [90]. These scanning techniques are only capable of sequential stimulation from one spot to the next at a relatively slow

speed (~100 ms) [59, 74].

Several studies have implemented spatial light modulators for simultaneous illumination at different areas to create patterns beyond slow sequential microscope scans. Digital micromirror devices (DMD) offer a fast <1 ms temporal resolution but waste laser power because patterning is accomplished by positioning select pixels to redirect light out of the excitation area. Nonetheless, a projector-based DMD system was able to demonstrate large-scale robust photostimulation of rat retinal tissue underneath the damaged photoreceptor layer of the eye [75]. More recently, light from an Argon laser was projected through a DMD for repeated patterned illumination [76]. A liquid-crystal spatial light modulator (LC-SLM) is more power-efficient, although it has a slower refresh rate that limits the generation of successive intensity patterns. LC-SLM has been integrated in a microscope setup to produce shapes composed of spots of variable size and number to match user-defined areas as a means to control the excitation scope and location [77]. A highly efficient, ultra-fast patterned optical stimulation has been demonstrated using acousto-optic deflectors (AOD), which steer a laser beam for high resolution scanning with the ability to modify exposure time and laser intensity for each neuron [94, 95].

Still, use of spatial light modulators has required external light sources. In theory, a light source may be mounted with these spatial modulators to overcome the limitation of testing only with immobile subjects. Potential high resolution optical neural interfaces for freely moving animal tests may include wirelessly controlled micron-sized optical sources. Arrays of high power gallium nitride micro light-emitting diodes (μLED) were already succesfully used in patterned stimulation of ChR2-expressing neuronal slices [78, 96, 97] and adapted for retinal prosthesis [98]. The emitted beam width from these μLED arrays were also scalable from 3–30 μm using lenses, where the output intensity profiles were represented as lambertian sources [78].

With patterned on-surface stimulation, inclusion of an electrical recording capability has been achieved with a hybrid optical-electrical micro-electrocorticography (μECoG; surface electrodes) [99]; the optically transparent conductor indium tin oxide (ITO) was used. Light transmission in the visible spectrum was measured at >90%, but emission profiles from the ITO pads were not characterized. A hybrid μECoG array has also been embedded with a

μLED array as a step towards fully-integrated optical neural interface systems [79].

2.4.2.4 Three-dimensional architectures for deep-tissue spatiotemporal stimulus patterning

In able to provide both depth access and spatiotemporal stimulus patterns over an area, the optical neural interface must contain a grid of penetrating waveguides—a 3D optrode array. During the time this work was in progress, other 3D optrode arrays were published. First, tens of the long silicon oxynitride neural probe [73] discussed above were manufactured and individually aligned within a comb matrix to create a 3D light delivery system [80]. A laser beam was successively passed through a DMD, a microlens array, a fiber bundle, and the 3D device for arbitrary patterning with hundreds of emission points along the width, length, and depth in tissue. Second, a simpler 4×4 array having tapered polymer waveguides (800 μm height, 50 μm tip diameter, 200 μm base diameter, ~500 μ pitch) was developed to target layer IV in rat primary visual cortex (V1) [81]. The polymer waveguides were made with a mold and stamp process. A separately assembled μLED array (220×270 μm^2 aperture each) was butt-coupled to the polymer array to provide a 460-nm excitation wavelength. The stimulation volume was defined as the scattering boundary of emitted light (measured as ~600 μm deep and ~100 mum wide in a gelatin-based tissue phantom layer); the waveguide effectively confined optical stimulation within the targeted plane.

2.5 References

[1] M. Furuhashi, M. Fujiwara, T. Ohshiro, M. Tsutsui, K. Matsubara, M. Taniguchi, S. Takeuchi, and T. Kawai, "Development of microfabricated tio[sub 2] channel waveguides," AIP Advances **1**, 032102 (2011).

[2] M. Bass, C. DeCusatis, G. Li, V. Mahajan, J. Enoch, E. Stryland, and O. S. of America, *Handbook of Optics: Optical Properties of Materials, Nonlinear Optics, Quantum Optics* (McGraw-Hill, 2009).

[3] L. Tong and E. Mazur, "Glass nanofibers for micro- and nano-scale photonic devices," J. Non-Cryst. Solids **354**, 1240–1244 (2008).

[4] K. Yamada, "Silicon photonic wire wavegudes: fundamental application," in *Silicon Photonics II*, vol. 119 of *Topics in Applied Physics* (Springer-Verlag Berlin Heidelberg, 2011), pp. 1–29.

[5] R. Deri and E. Kapon, "Low-loss III-V semiconductor optical waveguides," IEEE J. Quantum. Electron. **27**, 626–640 (1991).

[6] K. Worhoff, E. Klein, G. Hussein, and A. Driessen, "Silicon oxynitride based photonics," in *Anniversary International Conference on Transparent Optical Networks*, vol. 3 (2008), pp. 266–269.

[7] A. R. Katritzky, S. Sild, and M. Karelson, "Correlation and prediction of the refractive indices of polymers by QSPR," (1998).

[8] R. H. French, J. M. Rodriguez-Parada, R. A. D. M. K. Yang, M. F. Lemon, M. J. Brown, C. R. Haeger, S. L. Samuels, and E. C. Romano, "Optical properties of materials for concentrator photovoltaic systems," Tech. rep., DuPont (2009).

[9] B. L. Booth and J. Fisher, "Practical optoelectronic substrate connectivity," Tech. rep., Optical Interlinks (2007).

[10] G. M. Hale and M. R. Querry, "Optical constants of water in the 200-nm to 200-um wavelength region," Appl. Opt. **12**, 555–563 (1973).

[11] V. Tuchin, *Handbook of Optical Biomedical Diagnostics* (SPIE Press, 2002).

[12] S. Prahl and S. L. Jacques, "Optical properties spectra," http://omlc.ogi.edu/spectra (2001).

[13] A. N. Yaroslavsky, P. C. Schulze, I. V. Yaroslavsky, R. Schober, F. Ulrich, and H.-J. Schwarzmaier, "Optical properties of selected native and coagulated human brain tissues in vitro in the visible and near infrared spectral range," Phys. Med. Biol. **47**, 2059 (2002).

[14] X. Han, "Optogenetics in the nonhuman primate," Prog. Brain Res. **196**, 215–233 (2012).

[15] N. G. Horton, K. Wang, D. Kobat, C. G. Clark, F. W. Wise, C. B. Schaffer, and C. Xu, "In vivo three-photon microscopy of subcortical structures within an intact mouse brain," Nat. Photonics. **7**, 205–209 (2013).

[16] F. Helmchen and W. Denk, "Deep tissue two-photon microscopy," Nat. Methods **2**, 932–940 (2005).

[17] J. G. Bernstein, X. Hana, M. A. Henningera, E. Y. Koa, X. Qiana, G. T. Franzesia, J. P. McConnella, P. Sterne, R. Desimone, and E. S. Boyden, "Prosthetic systems for therapeutic optical activation and silencing of genetically-targeted neurons," Proc. Soc. Photo. Opt. Instrum. Eng. **6854**, 68540H (2008).

[18] L. Wang and S. L. Jacques, *MCML - Monte Carlo modeling of light transport in multi-layered tissues in standard C*, University of Texas M. D. Anderson Cancer Center (USA) (1992).

[19] A. M. Aravanis, L.-P. Wang, F. Zhang, L. A. Meltzer, M. Z. Mogri, M. B. Schneider, and K. Deisseroth, "An optical neural interface: in vivo control of rodent motor cortex with integrated fiberoptic and optogenetic technology," J. Neural Eng. **4**, S143 (2007).

[20] V. V. Tuchin, "Light scattering study of tissues," Physics-Uspekhi **40**, 495 (1997).

[21] A. L. McKenzie, "Physics of thermal processes in laser-tissue interaction," Phys. Med. Biol. **35**, 1175 (1990).

[22] J. Wells, C. Kao, P. Konrad, T. Milner, J. Kim, A. Mahadevan-Jansen, and E. D. Jansen, "Biophysical mechanisms of transient optical stimulation of peripheral nerve," Biophys. J. **93**, 2567–2580 (2007).

[23] J. Wells, C. Kao, K. Mariappan, J. Albea, E. D. Jansen, P. Konrad, and A. Mahadevan-Jansen, "Optical stimulation of neural tissue in vivo," Opt. Lett. **30**, 504–506 (2005).

[24] J. Wells, C. Kao, E. D. Jansen, P. Konrad, and A. Mahadevan-Jansen, "Application of infrared light for in vivo neural stimulation," J. Biomed. Opt. **10**, 064003 (2005).

[25] J. Cardin, M. Carlen, K. Meletis, U. Knoblich, F. Zhang, K. Deisseroth, L.-H. Tsai, and C. I. Moore, "Targeted optogenetic stimulation and recording of neurons in vivo using cell-type-specific expression of Channelrhodopsin-2," Nat. Protoc. **5**, 247–254 (2010).

[26] J. A. Cardin, "Dissecting local circuits in vivo: integrated optogenetic and electrophysiology approaches for exploring inhibitory regulation of cortical activity," J. Physiol. Paris **106**, 104–111 (2012).

[27] O. Yizhar, L. Fenno, T. Davidson, M. Mogri, and K. Deisseroth, "Optogenetics in neural systems," Neuron **71**, 9–34 (2011).

[28] M. G. Shapiro, K. Homma, S. Villarreal, C.-P. Richter, and F. Bezanilla, "Infrared light excites cells by changing their electrical capacitance," Nat. Commun. **3**, 736 (2012).

[29] M. W. Jenkins, A. R. Duke, S. Gu, Y. Doughman, H. J. Chiel, H. Fujioka, M. Watanabe, E. D. Jansen, and A. M. Rollins, "Optical pacing of the embryonic heart," Nat. Photonics. **4**, 623–626 (2010).

[30] J. Wells, P. Konrad, C. Kao, E. D. Jansen, and A. Mahadevan-Jansen, "Pulsed laser versus electrical energy for peripheral nerve stimulation," J. Neurosci. Methods **163**, 326–337 (2007).

[31] I. U. Teudt, A. E. Nevel, A. D. Izzo, J. T. Walsh, and C.-P. Richter, "Optical stimulation of the facial nerve: a new monitoring technique?" The Laryngoscope **117**, 1641–1647 (2007).

[32] A. D. Izzo, C.-P. Richter, E. D. Jansen, and J. T. Walsh, "Laser stimulation of the auditory nerve," Lasers Surg. Med. **38**, 745–753 (2006).

[33] F. Zhang, L.-P. Wang, M. Brauner, J. F. Liewald, K. Kay, N. Watzke, P. G. Wood, E. Bamberg, G. Nagel, A. Gottschalk, and K. Deisseroth, "Multimodal fast optical interrogation of neural circuitry," Nature **446**, 633–639 (2007).

[34] T. J. Foutz, R. L. Arlow, and C. C. McIntyre, "Theoretical principles underlying optical stimulation of a channelrhodopsin-2 positive pyramidal neuron," J. Neurophysiol. **107**, 3235–3245 (2012).

[35] L. Fenno, O. Yizhar, and K. Deisseroth, "The development and application of optogenetics," Annu. Rev. Neurosci. **34**, 389–412 (2011).

[36] J. Cayce, C. Kao, J. Malphrus, P. Konrad, A. Mahadevan-Jansen, and E. Jansen, "Infrared neural stimulation of thalamocortical brain slices," IEEE J. Sel. Topics in Quantum Electron. **16**, 565–572 (2010).

[37] J. M. Cayce, R. M. Friedman, E. D. Jansen, A. Mahavaden-Jansen, and A. W. Roe, "Pulsed infrared light alters neural activity in rat somatosensory cortex in vivo," Neuroimage **57**, 155–166 (2011).

[38] N. Fried, S. Rais-Bahrami, G. Lagoda, A.-Y. Chuang, L.-M. Su, and A. Burnett, "Identification and imaging of the nerves responsible for erectile function in rat prostate, in vivo, using optical nerve stimulation and optical coherence tomography," IEEE J. Sel. Topics in Quantum Electron. **13**, 1641–1645 (2007).

[39] A. Izzo, J. Walsh, E. Jansen, M. Bendett, J. Webb, H. Ralph, and C.-P. Richter, "Optical parameter variability in laser nerve stimulation: a study of pulse duration, repetition rate, and wavelength," IEEE T. Bio-Med. Eng. **54**, 1108–1114 (2007).

[40] S. M. Rajguru, A. I. Matic, A. M. Robinson, A. J. Fishman, L. E. Moreno, A. Bradley, I. Vujanovic, J. Breen, J. D. Wells, M. Bendett, and C.-P. Richter, "Optical cochlear implants: evaluation of surgical approach and laser parameters in cats," Hearing Res. **269**, 102–111 (2010).

[41] B. Y. Chow, X. Han, A. S. Dobry, X. Qian, A. S. Chuong, M. Li, M. A. Henninger, G. M. Belfort, Y. Lin, P. E. Monahan, and E. S. Boyden, "High-performance genetically targetable optical neural silencing by light-driven proton pumps," Nature **463**, 98–102 (2010).

[42] A. Berndt, P. Schoenenberger, J. Mattis, K. M. Tye, K. Deisseroth, P. Hegemann, and T. G. Oertner, "High-efficiency channelrhodopsins for fast neuronal stimulation at low light levels," Proc. Nat. Acad. Sci. **108**, 7595–7600 (2011).

[43] X. Han, X. Qian, J. G. Bernstein, H.-h. Zhou, G. T. Franzesi, P. Stern, R. T. Bronson, A. M. Graybiel, R. Desimone, and E. S. Boyden, "Millisecond-timescale optical control of neural dynamics in the nonhuman primate brain," Neuron **62**, 191–198 (2009).

[44] J. J. Hutsler, D.-G. Lee, and K. K. Porter, "Comparative analysis of cortical layering and supragranular layer enlargement in rodent carnivore and primate species," Brain Res. **1052**, 71–81 (2005).

[45] H. Gray, *Anatomy of the Human Body* (Philadelphia: Lea & Febiger, 1918), 20th ed.

[46] W. Agnew, D. McCreery, T. Yuen, and L. Bullara, "Histologic and physiologic evaluation of electrically stimulated peripheral nerve: considerations for the selection of parameters," Ann. Biomed. Eng. **17**, 39–60 (1989).

[47] H. A. C. Wark, R. Sharma, K. S. Mathews, E. Fernandez, J. Yoo, B. Christensen, P. Tresco, L. Rieth, F. Solzbacher, R. A. Normann, and P. Tathireddy, "A new high-density (25 electrodes/mm 2) penetrating microelectrode array for recording and stimulating sub-millimeter neuroanatomical structures," J. Neural Eng. **10**, 045003 (2013).

[48] J. A. McNulty, "Histology part 6: Neural tissue," http://www.meddean.luc.edu.

[49] P. Schoenenberger, A. Grunditz, T. Rose, and T. G. Oertner, "Optimizing the spatial resolution of channelrhodopsin-2 activation," Brain Cell. Biol. **36**, 119–27 (2008).

[50] E. Stark, T. Koos, and G. Buzski, "Diode probes for spatiotemporal optical control of multiple neurons in freely moving animals," J. Neurophysiol. **108**, 349–363 (2012).

[51] S. M. Rajguru, C.-P. Richter, A. I. Matic, G. R. Holstein, S. M. Highstein, G. M. Dittami, and R. D. Rabbitt, "Infrared photostimulation of the crista ampullaris," J. Physiol. **589**, 1283–1294 (2011).

[52] D. M. Harris, S. M. Bierer, J. D. Wells, and J. O. Phillips, "Optical nerve stimulation for a vestibular prosthesis," Proc. SPIE **5**, 7180–21 (2009).

[53] A. C. Thompson, S. A. Wade, W. G. A. Brown, and P. R. Stoddart, "Modeling of light absorption in tissue during infrared neural stimulation," J. Biomed. Opt. **17**, 0750021–0750026 (2012).

[54] A. C. Thompson, S. A. Wade, P. J. Cadusch, W. G. A. Brown, and P. R. Stoddart, "Modeling of the temporal effects of heating during infrared neural stimulation," J. Biomed. Opt. **18**, 035004–035004 (2013).

[55] L. E. Moreno, S. M. Rajguru, A. I. Matic, N. Yerram, A. M. Robinson, M. Hwang, S. Stock, and C.-P. Richter, "Infrared neural stimulation: beam path in the guinea pig cochlea," Hearing Res. **282**, 289–302 (2011).

[56] E. S. Boyden, F. Zhang, E. Bamberg, G. Nagel, and K. Deisseroth, "Millisecond-timescale, genetically targeted optical control of neural activity," Nat. Neurosci. **8**, 1263–1268 (2005).

[57] M. S. Grubb and J. Burrone, "Channelrhodopsin-2 localised to the axon initial segment," PLoS ONE **5**, e13761 (2010).

[58] M. Valley, S. Wagner, B. W. Gallarda, and P. Lledo, "Using affordable led arrays for photo-stimulation of neurons." J. Vis. Exp. **57**, e3379 (2011).

[59] A. M. Packer, D. S. Peterka, J. J. Hirtz, R. Prakash, K. Deisseroth, and R. Yuste, "Two-photon optogenetics of dendritic spines and neural circuits in 3D," Nat. Methods **9**, 1202C1205 (2012).

[60] R. Hira, N. Honkura, J. Noguchi, Y. Maruyama, G. J. Augustine, H. Kasai, and M. Matsuzaki, "Transcranial optogenetic stimulation for functional mapping of the motor cortex," J. Neurosci. Methods **179**, 258–263 (2009).

[61] B. R. Arenkiel, J. Peca, I. G. Davison, C. Feliciano, K. Deisseroth, G. J. Augustine, M. D. Ehlers, and G. Feng, "In vivo light-induced activation of neural circuitry in transgenic mice expressing channelrhodopsin-2," Neuron **54**, 205–218 (2007).

[62] J. A. Cardin, M. Carlen, K. Meletis, U. Knoblich, F. Zhang, K. Deisseroth, L.-H. Tsai, and C. I. Moore, "Driving fast-spiking cells induces gamma rhythm and controls sensory responses," Nature **459**, 663–667 (2009).

[63] S. K. Mohanty, R. K. Reinscheid, X. Liu, N. Okamura, T. B. Krasieva, and M. W. Berns, "In-depth activation of channelrhodopsin 2-sensitized excitable cells with high spatial resolution using two-photon excitation with a near-infrared laser microbeam," Biophys. J. **95**, 3916–3926 (2008).

[64] J. P. Rickgauer and D. W. Tank, "Two-photon excitation of channelrhodopsin-2 at saturation," Proc. Nat. Acad. Sci. **106**, 15025–15030 (2009).

[65] E. Papagiakoumou, F. Anselmi, A. Begue, V. de Sars, J. Gluckstad, E. Y. Isacoff, and V. Emiliani, "Scanless two-photon excitation of channelrhodopsin-2," Nat. Methods **7**, 848–854 (2010).

[66] B. K. Andrasfalvy, B. V. Zemelman, J. Tang, and A. Vaziri, "Two-photon single-cell optogenetic control of neuronal activity by sculpted light," Proc. Nat. Acad. Sci. **107**, 11981–11986 (2010).

[67] J. Zhang, F. Laiwalla, J. A. Kim, H. Urabe, R. V. Wagenen, Y.-K. Song, B. W. Connors, F. Zhang, K. Deisseroth, and A. V. Nurmikko, "Integrated device for optical stimulation and spatiotemporal electrical recording of neural activity in light-sensitized brain tissue," J. Neural Eng. **6**, 055007 (2009).

[68] P. Anikeeva, A. S. Andalman, I. Witten, M. Warden, I. Goshen, L. Grosenick, L. A. Gunaydin, L. M. Frank, and K. Deisseroth, "Optetrode: a multichannel readout for optogenetic control in freely moving mice," Nat. Neurosci. **15**, 163–170 (2012).

[69] S. Royer, B. V. Zemelman, M. Barbic, A. Losonczy, G. Buzski, and J. C. Magee, "Multi-array silicon probes with integrated optical fibers: light-assisted perturbation and recording of local neural circuits in the behaving animal." Eur. J. Neurosci. **31**, 2279–2291 (2010).

[70] A. V. Kravitz and A. C. Kreitzer, "Optogenetic manipulation of neural circuitry in vivo." Curr. Opin. Neurobiol. **21**, 433–439 (2011).

[71] R. Kobayashi, S. Kanno, S. Sakai, S. Lee, M. Koyanagi, H. Yao, and T. Tanaka, "Development of si neural probe with optical waveguide for highly accurate optical stimulation of neuron," in *Proceedings of the International IEEE/EMBS Conference on Neural Engineering* (2011), pp. 294–297.

[72] M. Im, I.-J. Cho, F. Wu, K. Wise, and E. Yoon, "Neural probes integrated with optical mixer/splitter waveguides and multiple stimulation sites," in *Proceedings of the IEEE Internationa Conference on Micro Electro Mechanical Systems* (2011), pp. 1051–1054.

[73] A. N. Zorzos, E. S. Boyden, and C. G. Fonstad, "Multiwaveguide implantable probe for light delivery to sets of distributed brain targets," Opt. Lett. **35**, 4133–4135 (2010).

[74] H. Wang, J. Peca, M. Matsuzaki, K. Matsuzaki, J. Noguchi, L. Qiu, D. Wang, F. Zhang, E. Boyden, K. Deisseroth, H. Kasai, W. C. Hall, G. Feng, and G. J. Augustine, "High-speed mapping of synaptic connectivity using photostimulation in channelrhodopsin-2 transgenic mice," Proc. Nat. Acad. Sci. **104**, 8143–8148 (2007).

[75] N. Farah, I. Reutsky, and S. Shoham, "Patterned optical activation of retinal ganglion cells," in *Proceedings of the International Conference of the IEEE Engineering in Medicine and Biology Society* (IEEE, 2007), pp. 6368–6370.

[76] H. Takahashi, T. Sakurai, H. Sakai, D. J. Bakkum, J. Suzurikawa, and R. Kanzaki, "Light-addressed single-neuron stimulation in dissociated neuronal cultures with sparse expression of ChR2." BioSystems **107**, 106–112 (2011).

[77] C. Lutz, T. S. Otis, V. DeSars, S. Charpak, D. A. DiGregorio, and V. Emiliani, "Holographic photolysis of caged neurotransmitters," Nat. Methods **5**, 821–827 (2008).

[78] N. Grossman, V. Poher, M. S. Grubb, G. T. Kennedy, K. Nikolic, B. McGovern, R. B. Palmini, Z. Gong, E. M. Drakakis, M. A. A. Neil, M. D. Dawson, J. Burrone, and P. Degenaar, "Multi-site optical excitation using ChR2 and micro-LED array," J. Neural Eng. **7**, 016004 (2010).

[79] K. Y. Kwon, B. Sirowatka, W. Li, and A. Weber, "Opto- uecog array: Transparent uecog electrode array and integrated LEDs for optogenetics," in *Proceedings of the IEEE Biomedical Circuits and Systems Conference* (2012), pp. 164–167.

[80] A. N. Zorzos, J. Scholvin, E. S. Boyden, and C. G. Fonstad, "Three-dimensional multiwaveguide probe array for light delivery to distributed brain circuits," Opt. Lett. **37**, 4841–4843 (2012).

[81] K. Kwon and W. Li, "Integrated multi-LED array with three-dimensional polymer waveguide for optogenetics," in *Proceedings of the International Conference on Micro Electro Mechanical Systems* (2013), pp. 1017–1020.

[82] A. R. Adamantidis, F. Zhang, A. M. Aravanis, and K. D. L. de Lecea, "Neural substrates of awakening probed with optogenetic control of hypocretin neurons," Nature **450**, 420–424 (2007).

[83] F. Zhang, V. Gradinaru, A. R. Adamantidis, R. Durand, R. D. Airan, L. De Lecea, and K. Deisseroth, "Optogenetic interrogation of neural circuits: technology for probing mammalian brain structures." Nat. Protoc. **5**, 439–456 (2010).

[84] I. B. Witten, S.-C. Lin, M. Brodsky, R. Prakash, I. Diester, P. Anikeeva, V. Gradinaru, C. Ramakrishnan, and K. Deisseroth, "Cholinergic interneurons control local circuit activity and cocaine conditioning," Science **330**, 1677–1681 (2010).

[85] V. Gradinaru, K. R. Thompson, F. Zhang, M. Mogri, K. Kay, M. B. Schneider, and K. Deisseroth, "Targeting and readout strategies for fast optical neural control in vitro and in vivo." J. Neurosci. **27**, 14231–14238 (2007).

[86] J. Voigts, J. H. Siegle, D. L. Pritchett, and C. I. Moore, "The flexdrive: An ultra-light implant for optical control and highly parallel chronic recording of neuronal ensembles in freely moving mice," Front. Syst. Neurosci. **7** (2013).

[87] J. Wang, F. Wagner, D. A. Borton, J. Zhang, I. Ozden, R. D. Burwell, A. V. Nurmikko, R. van Wagenen, I. Diester, and K. Deisseroth, "Integrated device for combined optical neuromodulation and electrical recording for chronic in vivo applications," J. Neural Eng. **9**, 016001 (2012).

[88] A. V. Kravitz, B. S. Freeze, P. R. L. Parker, K. Kay, M. T. Thwin, K. Deisseroth, and A. C. Kreitzer, "Regulation of parkinsonian motor behaviours by optogenetic control of basal ganglia circuitry," Nature **466**, 622–626 (2010).

[89] S. Tanghe, K. Najafi, and K. Wise, "A planar iro multichannel stimulating electrode for use in neural prostheses," Sensor. Actuat. B: Chem. **1**, 464–467 (1990).

[90] O. G. S. Ayling, T. C. Harrison, J. D. Boyd, A. Goroshkovy, and T. H. Murphy, "Automated light-based mapping of motor cortex by photoactivation of channelrhodopsin-2 transgenic mice," Nat. Methods **6**, 219–224 (2009).

[91] B. Rubehn, S. B. E. Wolff, P. Tovote, A. Luthi, and T. Stieglitz, "A polymer-based neural microimplant for optogenetic applications: design and first in vivo study," Lab Chip **13**, 579–588 (2013).

[92] J. Register, A. Muller, J. King, E. Weeber, C. L. Frewin, and S. E. Saddow, "Silicon carbide waveguides for optogenetic neural stimulation," in *MRS Proceedings*, vol. 1433 (2012), pp. mrss12–1433–h04–20.

[93] L. Petreanu, D. Huber, A. Sobczyk, and K. Svoboda, "Channelrhodopsin-2cassisted circuit mapping of long-range callosal projections," Nat. Neurosci. **10**, 663–668 (2007).

[94] Y. Liu, Y. Zhao, X. Lv, Y. Li, X. Zhang, J. Zhang, L. Wang, and S. Zeng, "Instrumentation of a compact random-access photostimulator based on acousto-optic deflectors," Rev. Sci. Instrum. **83**, 025116 (2012).

[95] K. Wang, Y. Liu, Y. Li, Y. Guo, P. Song, X. Zhang, S. Zeng, and Z. Wang, "Precise spatiotemporal control of optogenetic activation using an acousto-optic device," PLoS ONE **6**, e28468 (2011).

[96] V. Poher, N. Grossman, G. T. Kennedy, K. Nikolic, H. X. Zhang, Z. Gong, E. M. Drakakis, E. Gu, M. D. Dawson, P. M. W. French, P. Degenaar, and M. A. A. Neil, "Micro-LED arrays: a tool for two-dimensional neuron stimulation," J. Phys. D: Appl. Phys. **41**, 094014 (2008).

[97] B. McGovern, R. Palmini, N. Grossman, E. Drakakis, V. Poher, M. Neil, and P. Degenaar, "A new individually addressable micro-led array for photogenetic neural stimulation," IEEE Trans. Biomed. Circuits. Syst. **4**, 469–476 (2010).

[98] P. Degenaar, N. Grossman, M. A. Memon, J. Burrone, M. Dawson, E. Drakakis, M. Neil, and K. Nikolic, "Optobionic vision - a new genetically enhanced light on retinal prosthesis," J. Neural Eng. **6**, 035007 (2009).

[99] P. Ledochowitsch, E. Olivero, T. Blanche, and M. Maharbiz, "A transparent uecog array for simultaneous recording and optogenetic stimulation," in *Proceedings of the Annual International Conference of the IEEE Engineering in Medicine and Biology Society* (2011), pp. 2937–2940.

CHAPTER 3

CHARACTERIZATION OF A 3D OPTRODE ARRAY FOR INFRARED NEURAL STIMULATION

Publication is reprinted with permission from Biomedical Optics Express

Volume 3 (9), pp. 2200 - 2219, 2012

Characterization of a 3D optrode array for infrared neural stimulation

T.V.F. Abaya,[1] M. Diwekar,[1] S. Blair,[1,2,*] P. Tathireddy,[1] L. Rieth,[1] G.A. Clark,[2] and F. Solzbacher[1,2]

[1] *Department of Electrical and Computer Engineering, University of Utah, Salt Lake City, Utah 84112, USA*

[2] *Department of BioEngineering, University of Utah, Salt Lake City, Utah 84112, USA*

[*] *blair@ece.utah.edu*

Abstract: This paper characterizes the Utah Slant Optrode Array (USOA) as a means to deliver infrared light deep into tissue. An undoped crystalline silicon (100) substrate was used to fabricate 10×10 arrays of optrodes with rows of varying lengths from 0.5 mm to 1.5 mm on a 400-μm pitch. Light delivery from optical fibers and loss mechanisms through these Si optrodes were characterized, with the primary loss mechanisms being Fresnel reflection, coupling, radiation losses from the tapered shank and total internal reflection in the tips. Transmission at the optrode tips with different optical fiber core diameters and light in-coupling interfaces was investigated. At $\lambda = 1.55\,\mu$m, the highest optrode transmittance of 34.7%, relative to the optical fiber output power, was obtained with a 50-μm multi-mode fiber butt-coupled to the optrode through an intervening medium of index $n = 1.66$. Maximum power is directed into the optrodes when using fibers with core diameters of 200 μm or less. In addition, the output power varied with the optrode length/taper such that longer and less tapered optrodes exhibited higher light transmission efficiency. Output beam profiles and potential impacts on physiological tests were also examined. Future work is expected to improve USOA efficiency to greater than 64%.

OCIS codes: (170.3890) Medical optics instrumentation; (220.4610) Optical fabrication; (230.7380) Waveguides, channeled; (260.3060) Infrared.

References and links

1. X. Navarro, T. B. Krueger, N. Lago, S. Micera, T. Stieglitz, and P. Dario, "A critical review of interfaces with the peripheral nervous system for the control of neuroprostheses and hybrid bionic systems," J. Peripher. Nerv. Syst. **10**, 229–258 (2005).
2. A. Branner, R. B. Stein, and R. A. Normann, "Selective stimulation of cat sciatic nerve using an array of varying-length microelectrodes," J. Neurophysiol. **85**, 1585–1594 (2001).
3. A. Branner, R. Stein, E. Fernandez, Y. Aoyagi, and R. Normann, "Long-term stimulation and recording with a penetrating microelectrode array in cat sciatic nerve," IEEE T. Bio-Med. Eng. **51**, 146–157 (2004).
4. R. A. Normann, B. R. Dowden, M. A. Frankel, A. M. Wilder, S. D. Hiatt, N. M. Ledbetter, D. A. Warren, and G. A. Clark, "Coordinated, multi-joint, fatigue-resistant feline stance produced with intrafascicular hind limb nerve stimulation," J. Neural Eng. **9**, 026019 (2012).
5. M. Frankel, B. Dowden, V. Mathews, R. Normann, G. Clark, and S. Meek, "Multiple-input single-output closed-loop isometric force control using asynchronous intrafascicular multi-electrode stimulation," IEEE T. Neur. Sys. Reh. **19**, 325–332 (2011).
6. P. Tathireddy, D. Rakwal, E. Bamberg, and F. Solzbacher, "Fabrication of 3-dimensional silicon microelectrode arrays using micro electro discharge machining for neural applications," in *Proceedings of the International Conference on Solid-State Sensors, Actuators and Microsystems (Transducers)*, (IEEE, 2009), pp. 1206–1209.

#168581 - $15.00 USD Received 15 May 2012; revised 8 Aug 2012; accepted 10 Aug 2012; published 24 Aug 2012

7. R. Normann, D. McDonnall, G. Clark, R. Stein, and A. Branner, "Physiological activation of the hind limb muscles of the anesthetized cat using the Utah Slanted Electrode Array," in *Proceedings of IEEE International Joint Conference on Neural Networks,* (IEEE, 2005), pp. 3103–3108.
8. J. A. McNulty, "Histology part 6: Neural tissue, http://zoomify.lumc.edu/histonew/neuro/neuro_main.htm" .
9. J. Wells, C. Kao, K. Mariappan, J. Albea, E. D. Jansen, P. Konrad, and A. Mahadevan-Jansen, "Optical stimulation of neural tissue in vivo," Opt. Lett. **30**, 504–506 (2005).
10. J. Wells, C. Kao, P. Konrad, T. Milner, J. Kim, A. Mahadevan-Jansen, and E. D. Jansen, "Biophysical mechanisms of transient optical stimulation of peripheral nerve," Biophys. J. **93**, 2567–2580 (2007).
11. M. G. Shapiro, K. Homma, S. Villarreal, C.-P. Richter, and F. Bezanilla, "Infrared light excites cells by changing their electrical capacitance," Nat. Commun. **3**, 736 (2012).
12. J. Wells, P. Konrad, C. Kao, E. D. Jansen, and A. Mahadevan-Jansen, "Pulsed laser versus electrical energy for peripheral nerve stimulation," J. Neurosci. Methods **163**, 326–337 (2007).
13. J. Wells, C. Kao, E. D. Jansen, P. Konrad, and A. Mahadevan-Jansen, "Application of infrared light for in vivo neural stimulation," J. Biomed. Opt. **10**, 064003 (2005).
14. R. G. McCaughey, C. Chlebicki, and B. J. Wong, "Novel wavelengths for laser nerve stimulation," Lasers Surg. Med. **42**, 69–75 (2010).
15. N. Fried, S. Rais-Bahrami, G. Lagoda, A.-Y. Chuang, L.-M. Su, and A. Burnett, "Identification and imaging of the nerves responsible for erectile function in rat prostate, in vivo, using optical nerve stimulation and optical coherence tomography," IEEE J. Sel. Topics in Quantum Electron. **13**, 1641–1645 (2007).
16. A. Izzo, J. Walsh, E. Jansen, M. Bendett, J. Webb, H. Ralph, and C.-P. Richter, "Optical parameter variability in laser nerve stimulation: A study of pulse duration, repetition rate, and wavelength," IEEE T. Bio-Med. Eng. **54**, 1108–1114 (2007).
17. J. M. Cayce, R. M. Friedman, E. D. Jansen, A. Mahavaden-Jansen, and A. W. Roe, "Pulsed infrared light alters neural activity in rat somatosensory cortex in vivo," Neuroimage **57**, 155–166 (2011).
18. J. Zhang, F. Laiwalla, J. A. Kim, H. Urabe, R. V. Wagenen, Y.-K. Song, B. W. Connors, F. Zhang, K. Deisseroth, and A. V. Nurmikko, "Integrated device for optical stimulation and spatiotemporal electrical recording of neural activity in light-sensitized brain tissue," J. Neural Eng. **6**, 055007 (2009).
19. J. Wang, F. Wagner, D. A. Borton, J. Zhang, I. Ozden, R. D. Burwell, A. V. Nurmikko, R. van Wagenen, I. Diester, and K. Deisseroth, "Integrated device for combined optical neuromodulation and electrical recording for chronic in vivo applications," J. Neural Eng. **9**, 016001 (2012).
20. S. Royer, B. V. Zemelman, M. Barbic, A. Losonczy, G. Buzski, and J. C. Magee, "Multi-array silicon probes with integrated optical fibers: light-assisted perturbation and recording of local neural circuits in the behaving animal." Eur. J. Neurosci. **31**, 2279–2291 (2010).
21. A. V. Kravitz and A. C. Kreitzer, "Optogenetic manipulation of neural circuitry in vivo." Curr. Opin. Neurobiol. **21**, 433–439 (2011).
22. A. V. Kravitz, B. S. Freeze, P. R. L. Parker, K. Kay, M. T. Thwin, K. Deisseroth, and A. C. Kreitzer, "Regulation of parkinsonian motor behaviours by optogenetic control of basal ganglia circuitry," Nature **466**, 622–626 (2010).
23. V. Gradinaru, K. R. Thompson, F. Zhang, M. Mogri, K. Kay, M. B. Schneider, and K. Deisseroth, "Targeting and readout strategies for fast optical neural control in vitro and in vivo." J. Neurosci. **27**, 14231–14238 (2007).
24. A. N. Zorzos, E. S. Boyden, and C. G. Fonstad, "Multiwaveguide implantable probe for light delivery to sets of distributed brain targets," Opt. Lett. **35**, 4133–4135 (2010).
25. T. V. F. Abaya, M. Diwekar, S. Blair, P. Tathireddy, L. Rieth, G. A. Clark, and F. Solzbacher, "Optical characterization of the Utah Slant OptrodeAarray for intrafascicular infrared neural stimulation," Proc. SPIE **8207**, 82075M (2012).
26. G. A. Clark, S. L. Schister, N. M. Ledbetter, D. J. Warren, F. Solzbacher, J. D. Wells, M. D. Keller, S. M. Blair, L. W. Rieth, and P. R. Tathireddy, "Selective, high-optrode-count, artifact-free stimulation with infrared light via intrafascicular Utah Slanted Optrode Arrays," Proc. SPIE **8207**, 82075I (2012).
27. R. Bhandari, S. Negi, L. Rieth, and F. Solzbacher, "Wafer-scale processed, low impedance, neural arrays with varying length microelectrodes," in "International Solid-State Sensors, Actuators and Microsystems Conference (Transducers)," (IEEE, 2009), pp. 1210–1213.
28. R. Bhandari, S. Negi, L. Rieth, and F. Solzbacher, "A wafer-scale etching technique for high aspect ratio implantable mems structures," Sens. Actuators, A **162**, 130–136 (2010).
29. M. Bass, C. DeCusatis, G. Li, V. Mahajan, J. Enoch, E. Stryland, and O. S. of America, *Handbook of Optics: Optical properties of materials, nonlinear optics, quantum optics*, Handbook of Optics (McGraw-Hill, 2009).
30. V. Tuchin, *Handbook of optical biomedical diagnostics* (SPIE Press, 2002).
31. D. Mynbaev and L. Scheiner, *Fiber-optic communications technology* (Prentice Hall, 2001).
32. Y.-F. Li and J. W. Y. Lit, "Transmission properties of a multimode optical-fiber taper," J. Opt. Soc. Am. A **2**, 462–468 (1985).
33. S. Tang, L. Wu, F. Li, T. Li, and R. T. Chen, "Compression-molded three-dimensional tapered optical polymeric waveguides for optoelectronic packaging," Proc. SPIE **3005**, 202–211 (1997).
34. Z.-N. Lu, R. Bansal, and P. Cheo, "Radiation losses of tapered dielectric waveguides: a finite difference analysis with ridge waveguide applications," J. Lightwave Technol. **12**, 1373–1377 (1994).

#168581 - $15.00 USD Received 15 May 2012; revised 8 Aug 2012; accepted 10 Aug 2012; published 24 Aug 2012

35. B. K. Garside, T. K. Lim, and J. P. Marton, "Ray trajectories in optical fiber tapered sections," Appl. Opt. **17**, 3670–3674 (1978).
36. R. Deri and E. Kapon, "Low-loss III-V semiconductor optical waveguides," IEEE J. Quantum. Electron. **27**, 626–640 (1991).
37. F. Bahloul, R. Attia, and D. Pagnoux, "Reduction of the overall coupling loss using nonuniform tapered microstructured optical fiber," in *Proceedings of International Conference on Transparent Optical Networks,* (IEEE, 2010), pp. 1–4.
38. S.-C. Hung, E.-Z. Liang, and C.-F. Lin, "Silicon waveguide sidewall smoothing by KrF excimer laser reformation," J. Lightwave Technol. **27**, 887–892 (2009).
39. Q. Xia, P. F. Murphy, H. Gao, and S. Y. Chou, "Ultrafast and selective reduction of sidewall roughness in silicon waveguides using self-perfection by liquefaction," Nanotechnology **20**, 345302 (2009).
40. K. K. Lee, D. R. Lim, L. C. Kimerling, J. Shin, and F. Cerrina, "Fabrication of ultralow-loss Si/SiO2 waveguides by roughness reduction," Opt. Lett. **26**, 1888–1890 (2001).
41. D. Sparacin, S. Spector, and L. Kimerling, "Silicon waveguide sidewall smoothing by wet chemical oxidation," J. Lightwave Technol. **23**, 2455–2461 (2005).

1. Introduction

Electrical stimulation of nerves has been demonstrated as a viable means of neuroprosthesis. Peripheral neuroprostheses typically use interfaces with peripheral nerves or muscles to restore motor and sensory functions [1]. Of these interfaces, the Utah Slant Electode Array (USEA) has been shown to provide comprehensive access to multiple independent motoneuron subpopulations and to effect local stimulation with low current levels, even in a long-term implant [2, 3, 4, 5]. These multielectrode arrays are designed to penetrate deeply into neural tissue, for example, to access the different fascicles within the peripheral nerve, as shown in Fig. 1. A typical USEA can reach up to 1.5-mm deep into tissue, but electrodes as long as 9 mm have been machined using alternative fabrication methods [6]. The variable length intrafascicular electrodes facilitate low stimulation threshold and selectivity with a few electrodes targeting a specific muscle [2]. The electrodes are placed in proximity to the target axons and thus bypass the epineurium and perineurium, which act as insulators that make stimulation from around the nerve (e.g., via cuff electrodes) weaker and less selective. In addition, the high-channel count (i.e., 100 electrodes) allows successive recruitment of neurons to evoke maximal fatigue-resistant forces in various muscles [7]; graded activation of several muscles with the USEA for normal multi-joint motions was demonstrated by producing a graceful feline stance with paralyzed hind limbs of the cat [4].

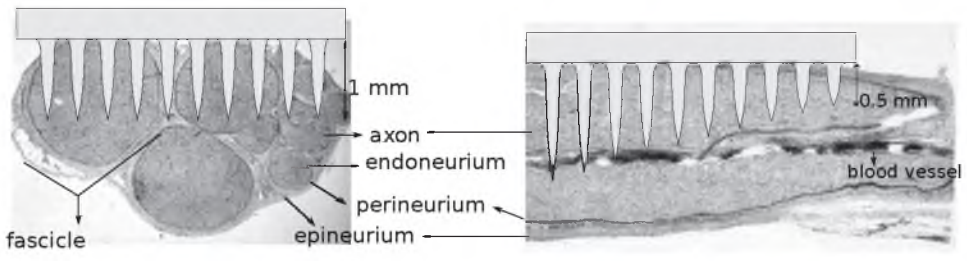

Fig. 1. Utah Slant Electrode/Optrode Array for peripheral nerve stimulation and/or recording. (a) Transverse cross-section of cat sciatic nerve with single row of slant array shown. The microneedles penetrate through epineurium, perineurium and endoneurium to access axons within the fascicle. (b) Longitudinal cross-section showing slant array reaching axons at various depths within the nerve. Adapted from [8].

Electrical signals, on the other hand, cause stimulus artifacts that prevent simultaneous recording and stimulation of adjacent neurons. An alternative modality using infrared light

#168581 - $15.00 USD Received 15 May 2012; revised 8 Aug 2012; accepted 10 Aug 2012; published 24 Aug 2012

as input energy avoids the artifact problem due to the absence of direct charge injection [9]. In the initial study [9], a pulsed IR laser was coupled to a 600-μm diameter optical fiber and the light was incident on a single spot on a rat sciatic nerve surface. Action potentials were selectively evoked without causing histological tissue damage. Stimulation and ablation fluence thresholds were determined for several wavelengths between 2.1 and 6.1 μm. Optimal wavelengths with a safety margin between stimulation and damage threshold for extraneural stimulation of mammalian peripheral nerves was observed to depend on the absorption spectrum of water, the dominant tissue absorber in the IR; damage threshold was strongly affected by the absorption, but stimulation commencement levels varied less. Stimulation at 3 and 6-μm wavelengths, which have very high absorption (i.e., approximately zero penetration depth) as shown in Fig. 2, readily created nerve damage with threshold stimulation fluence; 2.1 and 4-μm wavelengths, which have smaller absorption coefficients, were found to be particularly well suited for infrared neural stimulation (INS). This finding, along with recordings of surface nerve temperatures, suggest that INS acts in nerve via the induction of a spatio-temporal heat gradient in the tissue (4°C at the axonal level) with about 3-mJ/mm^2 extraneural threshold dose [10]. Although the underlying physiological mechanism is still under investigation, the threshold optical dose closely follows the water absorption spectrum. A recent study however, determined that IR is absorbed by water during INS and causes local tissue heating that depolarizes the target cell by changing the membrane electrical capacitance [11].

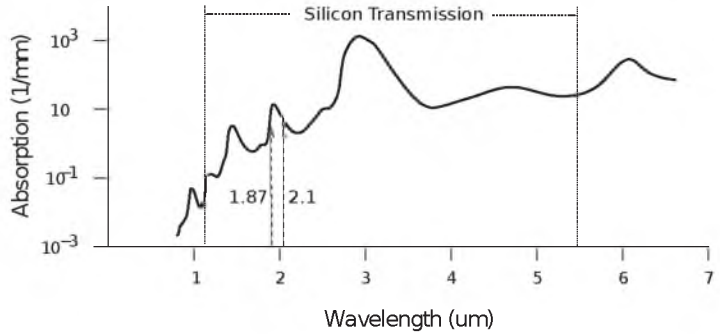

Fig. 2. Water absorption curve for IR wavelengths, which is representative of tissue absorption in the IR. 1.87 μm is recommended for peripheral nerve INS, but 2.1 μm has also been extensively used.

With a 2.12-μm (Ho:YAG laser) input, INS has been demonstrated to achieve a selective excitation volume with respect to extraneural electrical stimulation [12]. A wavelength of 2.12 μm has been extensively used because it causes minimal nerve damage and can be generated from a commercially available Ho:YAG laser that is currently utilized in many clinical applications [9, 13]. This wavelength corresponds to a tissue penetration depth between 300 and 500 μm as supported by Fourier transform infrared spectroscopy results in [12], which is deemed suitable for stimulation based on rat peripheral nerve geometry [13, 12]; a wavelength in the vicinity of 1.87 μm, having similar absorption characteristics as 2.12 μm, has also been shown to stimulate effectively in various applications [14, 15, 16, 17]. However, neural tissue of different types and morphologies may require different wavelengths for optimal stimulation such that the optical penetration depth is matched to the targeted excitable tissue.

As with electrical stimulation, an intrafascicular multiple access approach for INS will likely provide coverage of a large number of independent neuron subpopulations, lower activation energy, and better spatial selectivity than extraneural INS. These advantages may be demonstrated by using *optrode* arrays made from intrinsic silicon (Si), with IR light coupled from a pulsed

#168581 - $15.00 USD Received 15 May 2012; revised 8 Aug 2012; accepted 10 Aug 2012; published 24 Aug 2012

or continuous wave (CW) laser source operating at wavelengths from 1.1 to 5.5 μm, as indicated in Fig. 2. Ultimately, INS with an optrode array is expected to yield a greater separation between stimulation and damage thresholds and permit a wider range of wavelengths to effect a neural response - light does not need to travel through the connective tissues within the nerve in order to reach the axons, potentially allowing wavelengths with high absorption to be used.

Other penetrating probes for optical stimulation have been used in the field of optogenetics, where visible light is delivered to excite genetically targeted neurons expressing light-sensitive channels (e.g., ChR2). Tapered optical fibers serving as tissue-penetrating optical probes have been utilized [18, 19, 20, 21, 22]. A single optrode made of a 50-μm multi-mode fiber was inserted in mouse brain slices to trigger localized epileptiform events in a single cortical site [18]. Simultaneous delivery of visible light to multiple neuronal sites have been achieved by arranging tapered single-mode optical fibers in a 2D array of optrodes [20]; etched fibers were glued to commercially available planar silicon probes, which are an alternative to tungsten electrodes utilized in previous studies [23]. Experiments with ChR2-transfected rat hippocampus demonstrated multiple local stimulation via these 2D arrays. A more sophisticated microfabricated 2D multiwaveguide probe was introduced as an alternative to crude arrays of tapered fibers [24]. The probe targets points along its axis (i.e., stimulation of sites along the depth rather than the lateral direction) using parallel independent single-mode rectangular waveguides of silicon oxynitride core and oxide cladding that converge into a probe structure. Each waveguide ends at a particular target depth with a corner aluminum mirror to perform side-firing; transmission efficiency ranged from 23 to 33% as determined from bench testing.

We have recently developed a micromachined 3D optrode array for infrared neural stimulation. This array covers a wide area of neuronal stimulation sites and reaches targets at varying depths, thereby facilitating high-channel-count optical stimulation. Preliminary optical [25] and *intrafascicular* physiological [26] testing results have been reported. In this paper, we perform detailed characterization of this early-generation Utah Slant Optrode Array (USOA) neural interface. The USOA is designed after the USEA architecture, which has been adapted for numerous physiological requirements, such as nerve dimensions and axon depth, through variation in electrode length and spacing. Note that the same design can be adapted to other transparent substrates for both INS and optogenetic applications.

2. The Utah Slant Optrode Array

The USOA in this paper consists of a 10×10 array of microneedles with lengths varying in one direction from 0.5 mm to 1.5 mm on a 400-μm pitch. Each optrode tapers to a point from a base width of about 180 μm. Fig. 3 is an SEM image of the USOA. Light input to the USOA is provided via optical fibers butt-coupled to the array backside where optrode bases are located. The optrodes act as waveguides and light emitted from the optrode tips stimulates axons in close proximity via local tissue heating.

2.1. Fabrication

Fabrication of the USOA takes advantage of the extensive development of the Utah Slant Electrode Array (USEA) [27]. The arrays are bulk-micromachined from an undoped ($\rho > 20\,\Omega\cdot$ cm) c-Si (100) wafer with 2-mm thickness and 76.2 ± 0.3-mm diameter. This substrate is able to transmit IR at wavelength $\lambda > 1.1\,\mu$m with negligible absorption losses. One wafer yields 49 5×5-mm^2 arrays.

2.1.1. Backside processing

The optical fibers for light input are butt-coupled to a polished side of the Si wafer to minimize any scattering losses. In order to facilitate fiber alignment with the optrode bases, a uniform

#168581 - $15.00 USD Received 15 May 2012; revised 8 Aug 2012; accepted 10 Aug 2012; published 24 Aug 2012

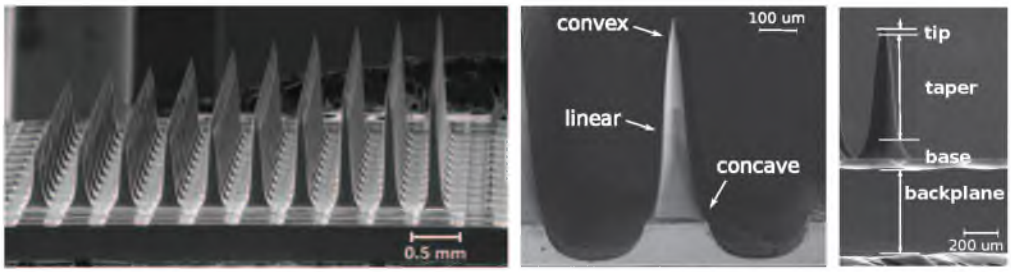

Fig. 3. SEM images of a Utah Slant Optrode Array. The array is bulk-micromachined from intrinsic (100) silicon. (a) Optrode lengths vary from 0.5 to 1.5 mm. (b) Taper profile of the shortest optrode. (c) Definition of optrode sections along the path of light propagation: 500-μm backplane, base extending 120 μm into linearly tapered shank, and $\sim$50-μm tip.

layer of 100-nm Al was deposited with ebeam evaporation on this side and was photolighographically patterned with 10×10 matrices of square windows. These windows were etched into the Al film using aluminum etchant (type A, Transene Co., Inc.). Arrays within the same wafer had different window sizes to accomodate testing with fibers of various core diameters. Part of the backside is shown in Fig. 4, where the windows are $140 \times 140\,\mu\text{m}^2$. This fabrication method is amenable to the integration of an anti-reflection (AR) coating because the AR layer(s) may be deposited before the aluminum.

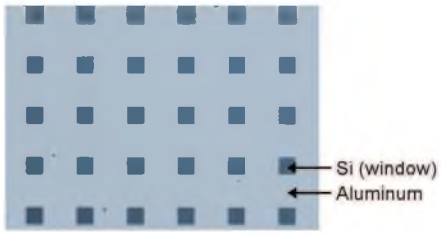

Fig. 4. Optrode backside showing windows in the aluminum layer for fiber alignment

2.1.2. Dicing

A Disco DAD 640 dicing saw was used to form vertical rectangular shanks on the frontside. Fig.5 shows the array transformation during dicing. First, seven sets of twelve cuts of depth gradient from 0.5 mm to 1.5 mm with 0.4-mm spacing are made with a resin blade across the wafer to form a slant in one direction (a). Material in-between the arrays was also removed by dicing before forming the shanks. With a nickel blade, deep kerfs were then diced into the silicon wafer to isolate the varying heights (b), and the same cuts were made in the 90° direction to create pillars (c). Each array had 10 rows of optrodes plus two extra rows on the longest side and three extra rows on the shortest side; in the orthogonal direction, there were two extra rows on each side. The extra rows were sacrifical features designed to enhance uniformity in optrode geometry across the array during wet etching. The average column width after dicing was 240 ± 15 μm.

#168581 - $15.00 USD Received 15 May 2012; revised 8 Aug 2012; accepted 10 Aug 2012; published 24 Aug 2012

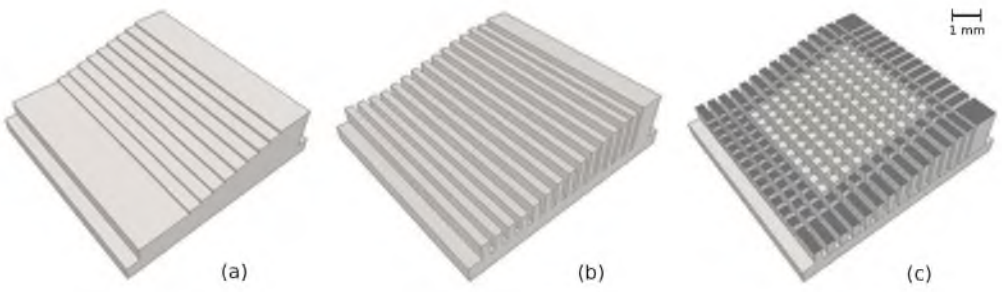

Fig. 5. Array dicing steps. Darker shanks constitute sacrificial regions.

2.1.3. Etching

Wafer-scale etching is a two-step process consisting of dynamic and static etching [28]. Fig. 6 illustrates the principle and Fig. 7 shows the progression of the optrodes during etching. For both steps, the wafer is mounted on a Teflon wafer holder comprised of a top plate and a base plate. The wafer fits into the recess in the base plate, and an O-ring along the edges protects the backside of the wafer from the wet etchant. The top plate is a donut-shaped piece that screws on the base plate and acts as a frame to secure the wafer in place.

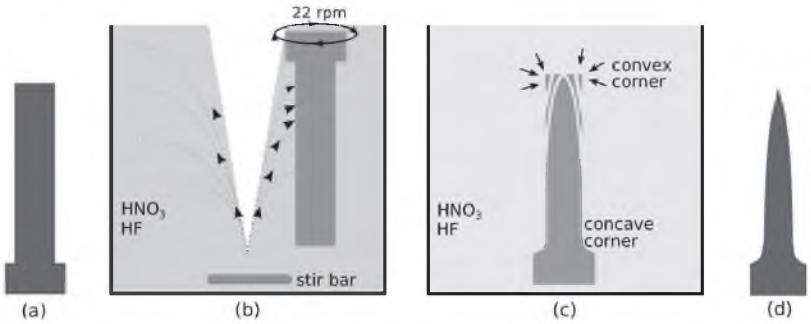

Fig. 6. Etching steps. (a) Initial shape of shanks. (b) Dynamic etching is performed for isotropic thinning. (c) Static etching preferentially sharpens the tips. (d) A missile-shaped optrode is formed. The arrows indicate locations of pronounced etching.

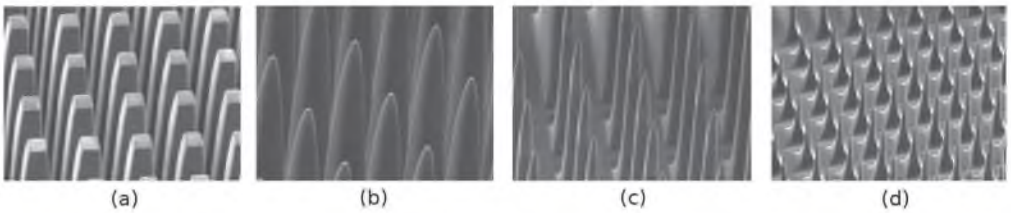

Fig. 7. SEM images showing optrode shape at different stages of the etching process. Dynamic etching narrows the shank (a), while static etching sharpens it (b-d). As etch time progresses, the tips progress from being blunt (b) to missile-shaped (c) to over-etched (d).

During dynamic etching, the wafer is immersed with columns facing down into 1500 ml of 1:19 acid mixture of HF (49%) and HNO_3 (69%). The wafer is rotated clockwise (22 rpm),

#168581 - $15.00 USD Received 15 May 2012; revised 8 Aug 2012; accepted 10 Aug 2012; published 24 Aug 2012

while a magnetic stirrer in the solution rotates counter-clockwise (500 rpm) to cause an aggressive and continuous flow of etchant into the high aspect ratio columns. This leads to uniform etching across the side-walls of the square columns. Apart from the rotation speed, other important dynamic etching parameters are the separation between the magnetic stir-bar and wafer (2 in), temperature of the etching solution (room temperature, but slightly increased because of exothermic etching reaction) and the etch time (5 min).

In static etching, the holder is placed in 750 ml of fresh acid mixture with the columns facing upwards. The diffusion-limited reaction and the relative inactivity at the base of the shanks preferentially etches the top of the columns until a sharp tip is formed. To ensure uniform static etching, a pipette is used to continuously remove byproducts near the top surface and circulate the solution. Static etch time is approximately 5 mins, which is when the optrodes are missile-shaped. Beyond this time, the optrodes become thinner.

2.1.4. Singulation

The last step is to separate the individual arrays from the wafer. A nickel blade was used in the dicing saw to trim the arrays into 10×10 structures by cutting off the sacrificial rows. Then, a resin blade was used to pierce the backside for singulation. The array in Fig. 3 is finally formed.

3. Theoretical loss mechanisms

The geometry of the optrodes and its input and output interfaces dominate the losses in the system. The primary loss mechanisms are expected to be Fresnel reflections (R), mode coupling, radiation, and loss due to reflection towards the source. Fig. 8 shows where these losses occur. The power from the fiber P_{in} is reduced by the transmittance $T_i = (1 - R_i)$ to P'_{in}, which is the power introduced to the Si backplane. P_{back}, P_{base} and P_{shank} are radiation losses, while P_{ref} is the lumped reflection loss from all sections within the device; absorption loss is assumed negligible. The output from the optrode tip is P_{out}. Power coupled into the shank and the power entering the tip is represented by $P_{coupled}$ and P_{tip}, respectively. The variables are related through

$$P_{in} \times (1 - R_i) = P'_{in} = P_{back} + P_{base} + P_{shank} + P_{out} + P_{ref}.$$

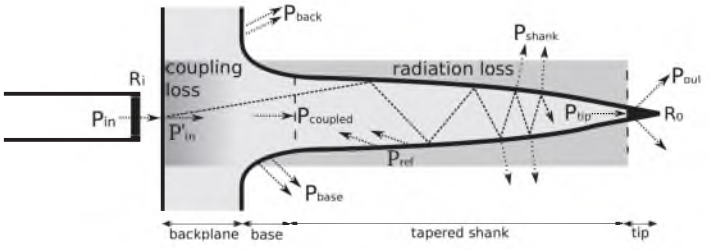

Fig. 8. Loss mechanisms within the optrode include Fresnel reflectance ($R_{i/o}$), coupling, radiation and backreflection losses.

3.1. *Fresnel reflections*

Fresnel reflection loss will occur at both the optrode backside and tip, which are the fiber-to-Si and Si-to-tissue interfaces, respectively. Table 1 lists the refractive indices (n) under consideration, while Table 2 shows relevant reflectance values as computed from

$$R = \left(\frac{n_1 - n_2}{n_1 + n_2} \right)^2, \tag{1}$$

#168581 - $15.00 USD Received 15 May 2012; revised 8 Aug 2012; accepted 10 Aug 2012; published 24 Aug 2012

for a single interface, where n_1 and n_2 are the refractive indices of the materials on either side of the interface. For double interfaces, as in the gap between the fiber and Si backside, this equation is applied twice, using the relation

$$R_{\text{eff}} = 1-(1-R_1)(1-R_2) = R_1+R_2-R_1R_2.$$

Note that interference effects were not considered.

Table 1. Refractive indices at 1.55 μm

Material	n	Reference
Air	1.00	
Silicon	3.48	[29]
Fused Silica (Fiber)	1.44	[29]
Tissue	1.36	[30]

Table 2. Reflectance at interfaces

Interface	Reflectance (R)	Transmittance (1-R)
Fiber-Air-Si	0.329	0.671
Fiber-1.44-Si	0.172	0.828
Fiber-1.66-Si	0.130	0.870
Si-Tissue	0.192	0.808
Si-Air	0.306	0.694

A fiber in contact with bare silicon leaves an air gap junction, which has an overall Fresnel reflectance loss of 32.9%. This gap can effectively be eliminated by using index matching fluid ($n = 1.44$), with index that matches that of the fiber; nevertheless, the remaining single-interface drops reflectance to 17.2%, leaving a theoretical maximum of 82.8% that can be transmitted to tissue. Using a higher refractive index fluid in the gap, such as $n = 1.66$, further reduces the reflectance loss to ~13%. In principle, an anti-reflection (AR) coating could be designed to minimize reflection loss at the input interface, but fiber index matching fluid would still be used to fill-in the air gap.

3.2. Mode coupling

Due to its high refractive index, the Si optrode is highly multi-moded. Losses in the coupling between two multi-mode waveguides are described in most textbooks on fiber optics [31], and are geometrical in nature. Extrinsic losses are due to alignment, including lateral displacement and end separation.

The intrinsic losses are due to mismatches in the core cross-sectional area (A) and numerical aperture (NA) between the fiber and optrode. The coupling efficiency (η) resulting from these losses may be quantified as

$$\eta_A = \frac{A_O}{A_F} \tag{2}$$

and

$$\eta_{\text{NA}} = \left(\frac{\text{NA}_\text{O}}{\text{NA}_\text{F}}\right)^2, \tag{3}$$

#168581 - $15.00 USD Received 15 May 2012; revised 8 Aug 2012; accepted 10 Aug 2012; published 24 Aug 2012

where the subscripts O and F signify the optrode and fiber waveguides, respectively. The effective numerical aperture of a tapered waveguide (for meridional rays) is given by

$$\mathrm{NA} = \frac{d_{min}}{d_{max}} cos\theta \sqrt{n_1^2 - n_2^2}, \tag{4}$$

where d_{max} and d_{min} are the diameters of the larger and smaller ends of the taper, n_1 and n_2 are the core and cladding indices, and θ is the angle of the taper slope with respect to the propagation direction [32].

Although the use of lensed fibers or external lenses may increase coupling efficiency, our studies were performed by direct fiber to optrode coupling for simplicity. Given the large refractive index contrast of the optrodes and the relatively small coupling fiber NA, we don't expect NA mismatch to be a significant source of loss.

3.3. Radiation and scattering loss

Radiation loss for the optrode is expected to result from its taper; higher-order guided modes are transformed into radiation modes as the diameter of the optrode decreases along its length. A simplified mathematical relationship that provides insight on how taper affects waveguide efficiency has been derived for a multi-mode to single-mode tapered slab using coupled-mode theory [33, 34]

$$P_{rad} = \left(\frac{3n}{8\pi} \frac{d_{max}^2 - d_{min}^2}{\lambda z} \right)^2, \tag{5}$$

where P_{rad} is the power loss normalized by the input power, n is the waveguide effective refractive index, λ is the wavelength, z is the propagation distance, and d_{max} and d_{min} are the maximum and minimum taper diameters, respectively. It is clear that more tapered waveguides (i.e., higher taper slope or angle) suffer from higher radiation loss. This is consistent with ray optics, from which it has been shown that higher taper slopes result in fewer total internal reflection (TIR) points along the waveguide wall and thus leak more power out as radiation [35]. It has been further shown that it is the higher order modes that significantly contribute to the loss [34], which correspond to the larger ray angles.

Likewise, 2D conical waveguides are expected to lose more power with increasing taper slope. Analysis on ray trajectories in multi-mode cylindrical linearly tapered optical fibers reveals that the total light transmitted from both meridional and skew rays is quadratically proportional to the effective numerical aperture of the taper (Eq. 4) [32]. Large diameter and high refractive index contrast silicon waveguides, such as the optrodes, are highly multi-moded and require extensive ray tracing analysis for accurate prediction of taper loss, but we will make use of Eq. 5 to provide qualitative insight.

Light may also be scattered inside the optrode when the guided modes interact with the etched waveguide surface. Scattering due to surface roughness is exacerbated by high refractive index contrast. For instance, the scattering loss for a symmetric slab waveguide with core index n_1 and cladding index n_2 has been modeled as [36]

$$P_s = \frac{\sigma^2 k_0^2 h}{\beta} (n_1^2 - n_2^2) E_S^2, \tag{6}$$

where σ is the roughness, k_0 is the free space wavenumber, h is transverse propagation constant in the cladding, β is the mode propagation constant and E_S is the normalized electric field amplitude at the core-cladding interface. Furthermore, light scattering may be more significant from an optrode in tissue due to the inherent inhomogeneity of tissue.

#168581 - $15.00 USD Received 15 May 2012; revised 8 Aug 2012; accepted 10 Aug 2012; published 24 Aug 2012

4. Characterization results and discussion

In all experiments, the optrode arrays were tested in air with a bare fiber mechanically aligned to one aluminum window on the backside at a time; the fiber was in contact with, but not attached to, the optrode base. Multiple measurement conditions were used to assist in separating the losses from the different regions of the optrode, as indicated in Fig 9. To isolate the output power, the optrode tips were punched through a thin aluminum foil (producing a 10×10 matrix of holes) in order to expose only the last 50 μm of each optrode to block light radiation from anywhere else along the propagation path (a); an IR detector was used to compare the light transmitted through the tip with the light transmitted through the coupling fiber. The optrodes were also inserted all the way through until the foil rests against the backplane in order to collect taper loss (b). Light leaking through the base region, which extends 120 μm from the backplane, was measured by covering only the backplane area between the optrodes using a 50-μm thick aluminum plate with pre-drilled holes that are 300 μm in diameter (c). Backplane radiation was included in the measurements by exposing all sections of the optrode (d). All radiation data were determined with an IR integrating sphere that captures light transmitted through the device at large angles, with the results normalized to the fiber output also measured with the integrating sphere. A 1550-nm continuous wave input is used for all measurements, except as noted with the Capella laser. A wavelength within the telecommunications band was used because of the availability of instrumentation that operates in this band. Telecommunications wavelengths have been demonstrated effective for INS [14].

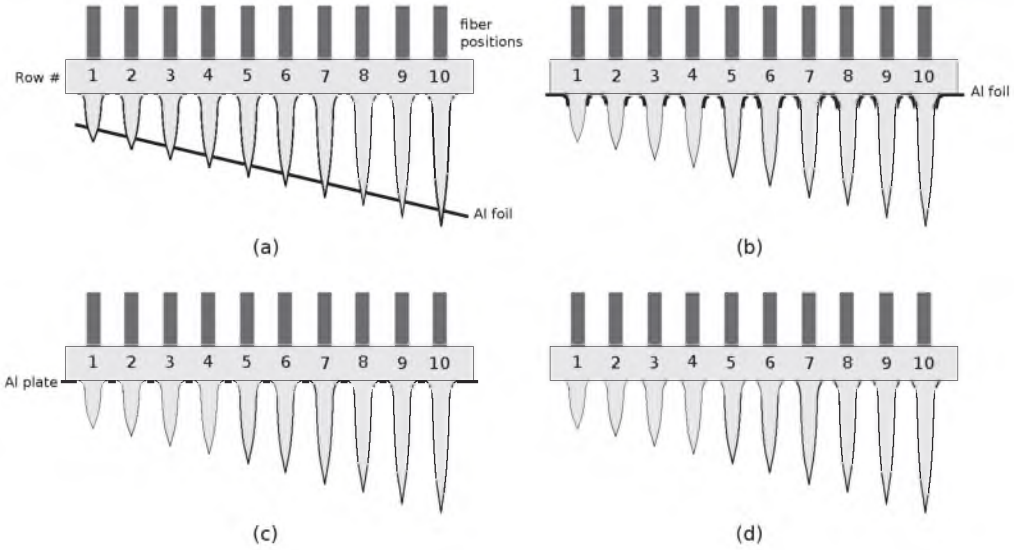

Fig. 9. Experimental setup. (a) Measuring output power from optrode tips. (b) Measuring taper loss from the shank. (c) Measuring base radiation. (d) Measuring backplane radiation.

4.1. Accounting for the backplane Fresnel loss

To verify the contribution of Fresnel reflection (R) at the input to the overall loss, the refractive index of the fiber to Si gap was varied ($n = 1.66, 1.44, 1.0$) with the use of index matching fluids. A 50-μm fiber with 0.22 NA delivered light to the optrode in these three sets of measurements. Light out of each optrode tip was collected by an IR photodetector. The fraction of power transmitted from fiber tip to optrode tip is shown in Fig 10(a). The three lines correspond to the different refractive indices used. The data points are plotted against the rows in the slant

#168581 - $15.00 USD Received 15 May 2012; revised 8 Aug 2012; accepted 10 Aug 2012; published 24 Aug 2012

array, which are aligned to the actual optrode length scale above the graph; Row 10 contains the longest optrodes as labeled in Fig. 9. The variation of the transmittance with optrode length is discussed in the next section.

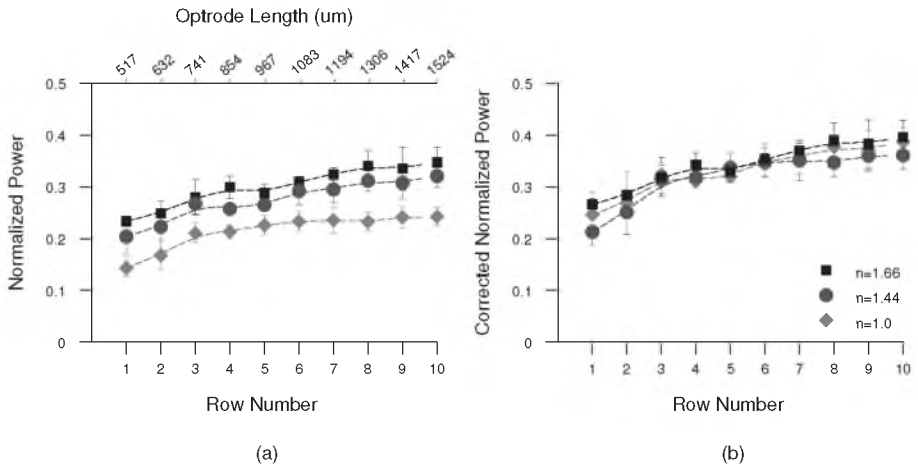

Fig. 10. Normalized output power from optrode tips with varying refractive index at the input interface using a 50-μm fiber with 0.22 NA.

The theoretical reflectance losses at the input with $n = 1.66$, $n = 1.44$ and air ($n = 1.0$) interfaces are 0.130, 0.172 and 0.329, respectively, resulting in an input transmittance value of $T_i = 0.87$ for the $n = 1.66$ interface. Without the input reflectance, the transmitted power for all cases should be equal because the remaining losses depend only on the fiber and optrode geometries. The output values, removing the input reflectance loss, are plotted in Figure 10(b). The line plots overlap within error, thus confirming the contribution of backside reflection loss as an independent factor. Note that if an AR coating were applied on the backside, the maximum efficiency attained would be about 39%, suggesting that it is more beneficial to reduce the remaining loss mechanisms.

4.2. Identifying other loss mechanisms

In order to assess the remaining loss mechanisms, transmission measurements from multi-mode fibers of different core sizes were performed. Fibers with 0.22 NA with diameters 50, 105, 200 and 400 μm were used to couple light to the optrodes through an n=1.66 medium. To separate the backplane reflection from all other sources of loss, T_i is factored out from all subsequent data; the resulting values are equivalent to the normalized output power with respect to the amount of power entering the device P'_{in}. Fig. 11(a) and (b) show normalized measurements for the different optrode lengths by coupling with 50 and 105-μm fibers, respectively. The lowest curve is the transmittance through the optrode tips, measured as before using the aluminum foil to block all other radiated light. The upper curve represents all of the light that passes through the USOA device (i.e., all of the light that does not reflect back towards the source or that is waveguided within the backplane). The same line plot is also the light measured by the sphere when the backplane is blocked with the aluminum plate. The middle curve is measured after further covering the base region. The set of curves reveal that the difference in the output power across different optrode lengths results from the varying taper slope; this is not surprising since the backplane and base geometry is the same for all optrodes. Note that these results will vary slightly when the optrode is applied *in vivo*, as the receiveing medium will go from $n = 1$ to $n = 1.34$ (i.e., tissue); the associated critical angle will increase and the

#168581 - $15.00 USD Received 15 May 2012; revised 8 Aug 2012; accepted 10 Aug 2012; published 24 Aug 2012

reflectance will decrease, both of which may allow higher transmission through the tips. Ray tracing simulations verify that the output power increases in a higher index medium.

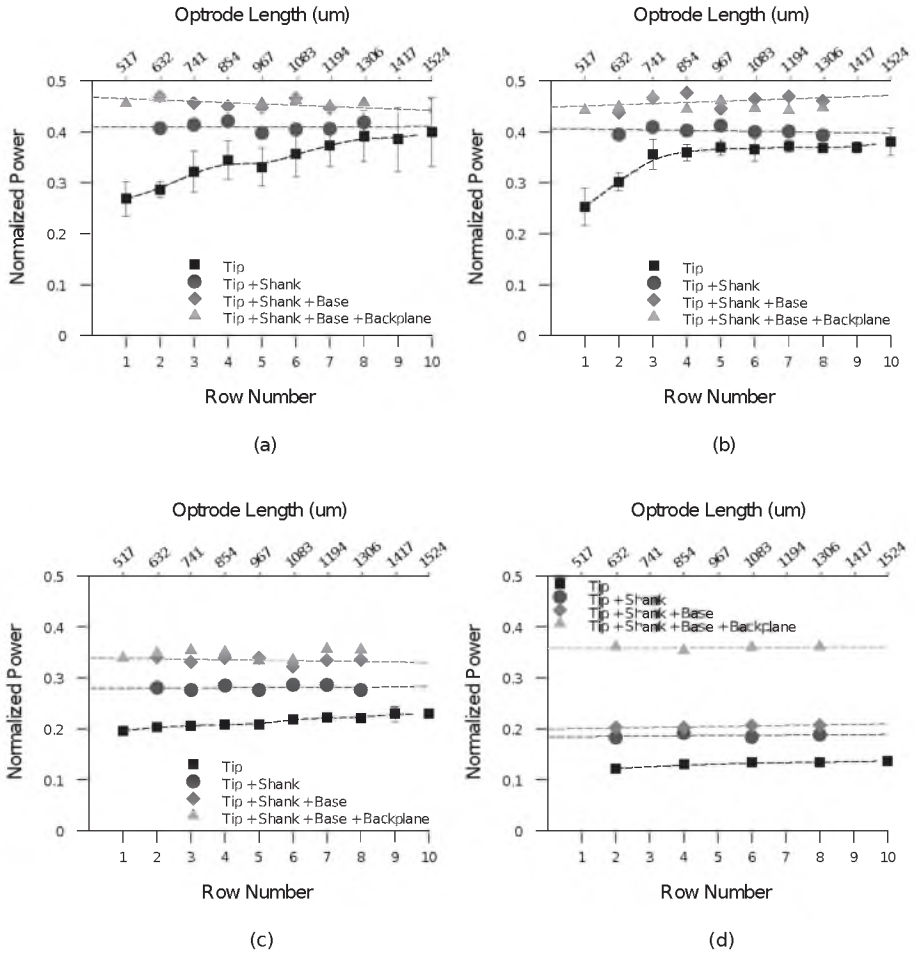

Fig. 11. Measurements to isolate coupling and taper losses with T_i factored out. Normalized tip output and radiation measurements from integrating sphere are shown. Fibers of 0.22 NA with 50-μm (a), 105-μm (b), 200-μm (c) and 400-μm (d) core diameters are coupled to the input.

The same measurements coupling from 200 and 400-μm optical fibers are shown in Fig. 11(c) and (d). Note that because the optrode pitch is 400 μm, alignment windows for the 400-μm fiber were placed only on even rows. In the case of the 400-μm fiber, there are two distinct upper curves, which signify that light is transmitted through the backplane.

The amount of power leaking through the backplane is largely due to the mismatch between the beam spot size and the base area; the NA mismatch between the fiber and optrode is not expected to represent a significant source of loss because $\mathrm{NA}_F < \mathrm{NA}_O$. The beam diameter at the optrode base is widened within the USOA backplane because of the NA of the fiber. Beam profiles of the coupling fibers were determined (section 4.3) and with the 0.5-mm backplane thickness, the effective beam sizes (i.e., width at $1/e^2$ of peak power) at the optrode base are estimated to be 89, 132, 253, and 433 μm for the 50, 105, 200, and 400-μm diameter fibers. Because the optrode base width is about 300 μm, we expect only light from the 400-μm fiber to

#168581 - $15.00 USD Received 15 May 2012; revised 8 Aug 2012; accepted 10 Aug 2012; published 24 Aug 2012

transmit through the backplane. The backplane radiation, which is derived from the difference between the *Tip+Shank+Base+Backplane* and *Tip+Shank+Base* curves of Fig. 11, supports this hypothesis as negligible backplane radiation is observed for fibers smaller than 400 μm. From the area mismatch (Eq. 2), 52% of the beam power from the 400-μm fiber will not be coupled into the base. Only 17% of the power falling outside the base region is measured as radiation, where 35% is expected otherwise. With the concaved backplane surface between the optrodes and the beam size larger than the pitch, rays outside of the base are likely to strike a curvature, undergo TIR and further backreflect towards the source.

Next, the loss due to base radiation is taken from the the difference of the *Tip+Shank+Base* and *Tip+Shank*, which is about 5% except for a 400-μm fiber. For the 400-μm fiber however, upon considering that only 48% of the power is coupled into the base according to previous theoretical analysis, the fractional base radiation loss with respect to the power entering the base is close to 5% as well. The base, like the shank and tip regions, is tapered. Fig. 3 shows the change in the optrode taper from a highly concave shape at the base to convex near the tip; from the effective aperture area above the base up to just below the tip, the optrode tapers linearly. These tapered regions reduce the overall transmission due to radiation and reflection losses. Radiation losses result from rays that don't satisfy TIR conditions, while rays that propagate at steep angles with respect to the optical axis can reflect back towards the source. The base is expected to act as a bottleneck for transmission since highly concave tapered waveguides have been found to exhibit higher propagation loss based on numerical studies [37]; in the case of the optrodes, the small input beams and the short base section prevents the huge loss. In theory, the 50 and 100-μm fibers should not incur base radiation as the optrode width into the shank is still larger than the beam size. However, even a few microns input misalignment will cause the small measured radiation. For bigger fibers with rays striking the base, the number of TIR reflections is decreased as propagation continues in the shank. A collimated input beam may be directed into the optrode shank in order to reduce the losses.

Shank loss depends on optrode length. Shanks inherently have different taper shapes and angle because optrodes of different lengths essentially have the same base shape and taper to about the same diameter at the tip. Shorter optrodes then result in a larger taper angle with respect to the propagation direction. This consequence is discernible in Fig. 3. Transmission through the shank, which is reduced primarily due to radiation loss, can be quantified and compared with theory. The steeper taper of the shorter optrodes causes more power loss, as briefly discussed in section 3.3. This is supported by the difference between the *Tip+Shank* and *Tip* curves of Fig. 11, which estimates the fraction of P'_{in} is radiated out of the optrode shanks. Results with larger input fibers exhibit greater loss and less variation with optrode length because most of the rays that have been directed into the shank have smaller angles with respect to the optical axis.

In order to compare the results with the simple coupled mode theory (CMT) approximation in Eq. 5, which is normalized to the power entering the taper (i.e., $P_{coupled}$), the CMT equation is fitted to the measured data with a single normalization factor. In this way, the loss trend is readily apparent. The matched data are plotted in Fig. 12. CMT predicts the change in radiation loss with varying taper slope for the smaller coupling fibers. Note that the CMT estimate is derived for a multi-mode to single-mode slab and accurate for low index contrast waveguide, whereas optrodes are highly multi-moded high index contrast 3D waveguides. Thus, with the data-fitting, the results presented in Fig. 12 reflect the slope to which the radiation is affected by the taper rather than the comparison between actual and theoretical radiation loss; although 3D waveguides are typically approximated as slabs, CMT underestimates the loss in multimode-to-multimode waveguides [34] and has its limitations when applied to high index contrast interfaces.

#168581 - $15.00 USD Received 15 May 2012; revised 8 Aug 2012; accepted 10 Aug 2012; published 24 Aug 2012

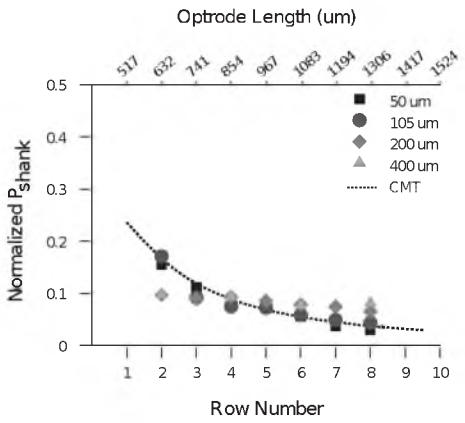

Fig. 12. Radiation loss through the tapered shank after factoring out T_i and fitting the CMT estimate. Fibers of 0.22 NA with varying core diameters are coupled to the input.

Scattering of light inside the shank due to sidewall roughness was considered. The surface roughness of the etched optrode walls was measured using atomic force microscopy (AFM) with an angled tip; the RMS roughness is determined to be 4.4 nm, which is considered optically smooth when compared with previously published results on silicon waveguides. Nevertheless, surface roughness may further be reduced by sidewall smoothing techniques. Lasers (e.g., KrF and XeCl excimer) have been used to decrease roughness via surface reflow in ridge waveguides; the laser selectively melts the sidewall edge, which flows under surface tension and solidifies into a smooth rounded layer [38, 39]. Creating a blanket layer of oxide (e.g., by wet oxidation) over the waveguide and subsequently etching it has also been proven to lower surface roughness [40]. For the high-contrast optrode, repeated wet oxidation and etching is perhaps the most practical approach [41].

The loss unaccounted for by the measurement results (i.e., $\sim 54\%$) is taken as the lump sum of reflection losses P_{ref} from all sections of the optrode. From the results and previous discussion, it is estimated that reflection losses at the tip dominate the system loss; this includes both the Fresnel reflectance on transmitted rays and rays that undergo two TIR's and are completely backreflected. P_{ref} for the smaller fibers is mainly due to reflection at the tips, whereas reflection from the base and backplane is included with values for the larger fibers.

4.3. Beam profiling

Beam profiling was performed to measure the effective spot size and divergence of the light exiting the optrode tips. Table 3 shows values of the beam width ($2W_0$) calculated at 13.5% ($1/e^2$) of the peak power at the optrode tip for different lengths, while Table 4 lists the far-field full divergence angle (ϕ). The measurements were made with 0.22 NA fibers of different core sizes at the input side without any index matching fluid.

The optrode output beam exhibits an approximate gaussian profile (1.56 M^2 fit on average) similar to that in Fig. 13; M^2 fit values of the profiles are also listed, in parentheses, in Table 3. Precise values of the beam width across different rows for the same input fiber were measured. For increasing fiber diameter, it appears that the beam width increases as well. However, values for the 200-μm fiber seem anomalous, which might be an effect of the higher divergence of this particular fiber as measured from the beam profiler.

The beam divergence depends on the divergence of the input fiber as well. More importantly, it varies with the optrode length/taper; the beam diverges more from the more tapered shorter

#168581 - $15.00 USD Received 15 May 2012; revised 8 Aug 2012; accepted 10 Aug 2012; published 24 Aug 2012

Table 3. Beam width ($2W_0$) in μm at 13.5% of peak power and M^2 fit.

Fiber Core Diameter (μm)	Fiber $2W_0$	Optrode $2W_0$ (M^2)		
		Row 4	Row 6	Row 8
50	41.4	46.3 (1.33)	44.0 (1.11)	45.2 (1.28)
105	71.9	51.7 (1.52)	54.7 (1.92)	50.2 (1.54)
200	188.0	71.4 (2.60)	63.2 (1.56)	66.2 (1.25)
400	378.0	66.8 (1.34)	65.4 (1.80)	61.7 (1.51)

Table 4. Beam far-field full divergence angle (ϕ) in $^\circ$ and Rayleigh distance (z_R) in μm.

Fiber Core Diameter (μm)	Fiber ϕ	Optrode ϕ (z_R)		
		Row 4	Row 6	Row 8
50	18.9	16.3 (163)	14.5 (174)	14.0 (185)
105	23.9	17.9 (165)	16.8 (187)	14.2 (202)
200	26.1	20.1 (204)	19.7 (184)	15.7 (241)
400	22.1	17.8 (215)	14.7 (255)	13.6 (260)

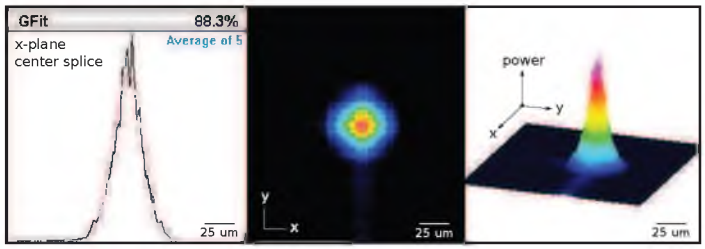

Fig. 13. Beam profile of a Row 6 optrode with a 105-μm input fiber of 0.22 NA. Power is relative to peak; widths vary according to row number and input fiber size.

optrodes. This observation may be explained using simple ray tracing analysis, as illustrated in Fig. 14, which is also supported by wave optics [35]. As light travels down the taper, its propagation angle θ_z increases after each wall reflection. This creates a smaller angle of incidence θ_i at the core-cladding interface that eventually loses total internal reflection. Because the taper angle ω is larger for shorter optrodes, θ_z increases more rapidly and rays exit away farther from the tips, which leads to a wider beam divergence.

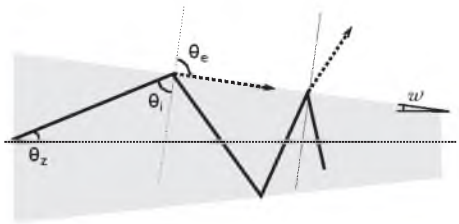

Fig. 14. Ray trajectory in a tapered waveguide. Because there is a faster increase in the propagation angle of a ray travelling through shorter optrodes, the rays exit away farther from the tip, which leads to a wider beam divergence.

The spatial divergence profile of the beam from an optrode in Row 6 with a 105-μm input

#168581 - $15.00 USD Received 15 May 2012; revised 8 Aug 2012; accepted 10 Aug 2012; published 24 Aug 2012

fiber is shown in Fig. 15; the beam width is plotted against the propagation distance along the z-plane. The plot is generated by using an M-squared fit for the beam width curve from measurement points of the beam profiler. The beam waist at the tip (i.e., 0 mm position) is 54.7 μm and broadens to 297.6 μm at a distance 1 mm away. Another important parameter in the z-profile is the Rayleigh distance (z_R), which defines the volume of effective energy deposition within the receiving medium. The Rayleigh distance defines how far the beam can travel before expanding considerably, beyond which the full angle divergence is measured; it is distance along the propagation direction where the minimum beam width increases by a factor of $\sqrt{2}$. The beam does not immediately diverge out from the optrode tip and is rather focused, but its energy quickly spreads beyond z_R. In Fig. 15, the beam energy extends 187 μm from the tip into the medium without significant divergence. Table 4 lists z_R for all beams; less divergent beams have a greater focus depth.

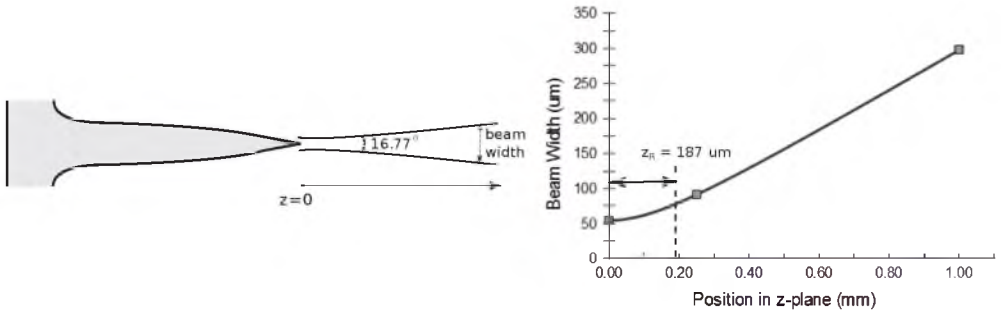

Fig. 15. Changes in beam width with propagation distance from an optrode in Row 6 of the array with a 105-μm input fiber of 0.22 NA.

The output beam divergence and width is predicted to decrease *in vivo* because of the higher refractive index of tissue; this is confirmed by ray tracing simulation results.

4.4. Coupling with the Capella laser

For physiological testing, a Capella laser (Aculight Corporation Infrared Neural Stimulator), with a pulsed output in the wavelength range of 1865 – 1879 nm, is used [26]. Thus, it is important to compile transmission characteristics from the Capella as well. Output power for all measurements were collected using a thermopile sensor. The wavelength chosen for the tests is 1875 nm, pulsed at 10 Hz with a duration of 17 μs to allow the use of the Coherent LabMax-TOP power meter.

4.4.1. Coupling efficiency from laser to fiber

The Capella laser has a ~400-μm emission aperture. A 400-μm fiber is then expected to collect a large fraction of light emitted by the laser. Halving the fiber core diameter is expected to reduce the output power from the fiber to one-fourth as the effective collecting area decreases by the same amount. Table 5 lists the power coupled from the Capella to multi-mode fibers of different diameters. Notice that the output power is about 25% of the value in the next row (i.e., when the core diameter is doubled), which is in accord with expectation.

4.4.2. Coupling efficiency from fiber to optrode

The 200 and 400-μm fibers were used to couple the laser to an optrode with an $n = 1.66$ gap interface. The percentage transmission is shown in Fig. 16 for both fibers across all rows. Note that the trend is consistent with the results in section 4.2, but with slightly lower values. The

#168581 - $15.00 USD Received 15 May 2012; revised 8 Aug 2012; accepted 10 Aug 2012; published 24 Aug 2012

Table 5. Transmitted power from the Capella laser to multi-mode fibers of different diameters

Core Diameter (μm)	Input Power (W)	Output Power (W)	Transmittance (%)
100	5	0.30	6.0
200	5	1.28	25.6
400	5	4.70	94.0

$< 2\%$ decrease between the 1550 to 1875 nm results may possibly be due to a difference in the distribution of modes in the multi-mode fibers. The laser source at 1550 nm is single mode, while the Capella is multi-moded, so launching conditions at the input are different. Moreover, we used short ($\sim$1 m) lengths of optical fiber, which are likely shorter than the equilibrium length, which is the length at which the power distribution across the modes stops changing. The slight discrepancy in the results might also simply be due to variations in the measurement setup; a pyroelectric sensor with a 10-mm wide aperture was used; the optrode shanks were positioned normal to the active area by resting the array on a frame atop the detector. The distance between an optrode tip and the detector depends on the optrode length, but reference measurements reveal that there is only about 0.25% decrease in the power detected for a 1-mm increase in the distance.

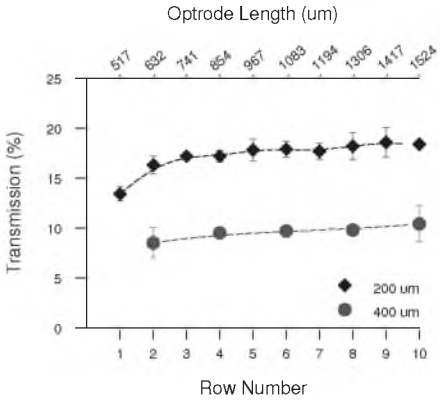

Fig. 16. Transmission through the optrode tips with 200 and 400-μm fibers using the Capella laser (1875 nm). The input coupling interface has n=1.66.

4.4.3. Overall system efficiency

The efficiency of the entire stimulation system for physiological experiments is computed by multiplying the results in sections 4.4.1 and 4.4.2. Table 6 shows a breakdown of the system efficiency and the output power expected to be delivered by the longest optrodes when the Capella emits 5 W. The maximum transmission is obtained using a 400-μm fiber. However, the overall efficiency is only 9.6%, producing 0.48 W of power from the optrode tips.

5. Improving the USOA efficiency

The efficiency of the USOA may be increased with techniques as outlined in Table 7. The table also summarizes the relevant losses determined from bench testing in air, as discussed throughout the paper, and the predicted loss after it is minimized. Fresnel reflection is taken as the theoretical value, while taper, base and backplane losses are computed from measurement

#168581 - $15.00 USD Received 15 May 2012; revised 8 Aug 2012; accepted 10 Aug 2012; published 24 Aug 2012

Table 6. Total efficiency (%) of coupling light from the Capella to the longest optrodes with varying fiber core sizes. Output power from the optrode tips is listed for a Capella emitting 5 W. For the 105-μm fiber, the overall efficiency and output power are estimated at $\lambda = 1550\,nm$.

Core Diameter (μm)	Laser-Fiber Efficiency	Optrode Efficiency at 1875 (1550) nm	Overall Efficiency	Output Power (mW)
100	6	— (33.0)	(1.98)	(99)
200	25.6	18.2 (20.0)	4.66	233
400	94	10.2 (11.8)	9.59	480

results from the integrating sphere with respect to the power entering the silicon. Antireflective coatings will eliminate the input and output Fresnel losses, while better in-coupling via lenses to collimate or focus the light into the effective aperture of the shank will reduce the backplane and base losses; note that the use of single-mode coupling fibers would in principle allow better control over the input beam properties. Taper losses and TIR within the tips may be reduced with more efficient shank and tip design, although there may be tradeoffs between optical performance and probe insertion properties. Ray tracing simulations will aid in studying alternative tip shapes. With tip losses minimized only by means of an AR layer and assuming the worst case improvement by taking a 31% Fresnel reflectance at the tip interface (i.e., Si-Air), the total laser to optrode transmission efficiency may be improved to a maximum of 64% given a laser source with aperture of $\leq$100 μm.

Table 7. Expected normalized power loss of the longest optrode when using a 50-μm input fiber with loss-minimization techniques. Optimizing tip shape is not yet considered.

	Current Loss	Solution	Expected Loss
Input interface	0.13	AR coating	~0
Backplane radiation	~0	focus/collimate	~ 0
Base radiation	0.05	focus/collimate	~0
Taper radiation	0.03	remove taper	~0
Tip losses	0.54	AR coating	0.36
Total	**0.62**		**0.36**

6. Conclusion

A neural interface for deep-tissue IR stimulation has been designed and tested. The Utah Slant Optrode Array, consisting of 10×10 varying length microneedle waveguides, was fabricated based on electrode array processing with key features altered to facilitate light transmission instead. Output power was measured from the optrode tips under various settings to characterize transmission efficiency; the optrodes exhibited losses from Fresnel reflection, mode coupling, radiation due to the tapered geometry and total internal reflection in the tips. Fresnel loss at the in-coupling interface contributed an independent reduction in transmittance, which is small compared to other loss mechanisms. Only coupling loss from a 400-μm fiber is significant, but light interactions with the base sidewall from using larger fibers cause more taper losses. Taper losses increased with shorter optrodes in accordance to the CMT model. Scattering loss is included in taper loss, but is deemed insignificant. In addition to the output power measurements, the effect of the optrode taper on the loss was established with beam profiling, where it was evident that power loss and divergence is greater for shorter, more tapered optrodes. With a

#168581 - $15.00 USD Received 15 May 2012; revised 8 Aug 2012; accepted 10 Aug 2012; published 24 Aug 2012

100-μm fiber delivering 1550-nm light to the optrode, the beam width at the tip is about 55 μm and diverges in the far-field at a full angle of 17°. The majority of the system loss for smaller input fibers is attributed to tip losses, which includes both Fresnel and total internal reflection.

Similar tests were performed with more direct relevance to physiological studies using the Capella laser. The coupling losses from the laser to fibers of smaller than 400-μm diameter dominate the overall system loss, overcoming the gain in fiber to optrode coupling efficiency offered by the smaller diameter fibers. A maximum system efficiency of only about 10% is obtained with the 400-μm fiber. Greater system efficiencies can be obtained using light sources with effective emission apertures smaller than 400 μm.

Improvements such as AR coating, focusing/collimating the input beams and removing the taper will increase the efficiency of the optrode array to a maximum of 64%. Taking into account the actual (i.e., higher) reflectance loss inside the tips and redesigning the tip shape will yield even higher efficiency values.

Acknowledgements

This work was funded by the University of Utah Research Foundation. We also acknowledge support by Lockheed Martin Aculight.

#168581 - $15.00 USD Received 15 May 2012; revised 8 Aug 2012; accepted 10 Aug 2012; published 24 Aug 2012

CHAPTER 4

A 3D GLASS OPTRODE ARRAY FOR OPTICAL NEURAL STIMULATION

Publication is reprinted with permission from Biomedical Optics Express

Volume 3 (12), pp. 3087 - 3104, 2012

Spotlight paper (January 2013)

A 3D glass optrode array for optical neural stimulation

T.V.F. Abaya,[1] S. Blair,[1,2,*] P. Tathireddy,[1] L. Rieth,[1] and F. Solzbacher[1,2]

[1] *Department of Electrical and Computer Engineering, University of Utah, Salt Lake City, Utah 84112, USA*

[2] *Department of BioEngineering, University of Utah, Salt Lake City, Utah 84112, USA*

[*] *blair@ece.utah.edu*

Abstract: This paper presents optical characterization of a first-generation SiO_2 optrode array as a set of penetrating waveguides for both optogenetic and infrared (IR) neural stimulation. Fused silica and quartz discs of 3-mm thickness and 50-mm diameter were micromachined to yield 10×10 arrays of up to 2-mm long optrodes at a 400-μm pitch; array size, length and spacing may be varied along with the width and tip angle. Light delivery and loss mechanisms through these glass optrodes were characterized. Light in-coupling techniques include using optical fibers and collimated beams. Losses involve Fresnel reflection, coupling, scattering and total internal reflection in the tips. Transmission efficiency was constant in the visible and near-IR range, with the highest value measured as 71% using a 50-μm multi-mode in-coupling fiber butt-coupled to the backplane of the device. Transmittance and output beam profiles of optrodes with different geometries was investigated. Length and tip angle do not affect the amount of output power, but optrode width and tip angle influence the beam size and divergence independently. Finally, array insertion in tissue was performed to demonstrate its robustness for optical access in deep tissue.

OCIS codes: (170.3890) Medical optics instrumentation; (220.4610) Optical fabrication; (230.7380) Waveguides, channeled; (170.3660) Light propagation in tissues

References and links

1. K. Deisseroth, "Optogenetics," Nat. Methods **8**, 26–29 (2011).
2. G. Nagel, T. Szellas, W. Huhn, S. Kateriya, N. Adeishvili, P. Berthold, D. Ollig, P. Hegemann, and E. Bamberg, "Channelrhodopsin-2, a directly light-gated cation-selective membrane channel," Proc. Natl. Acad. Sci. U. S. A. **100**, 13940–13945 (2003).
3. F. Zhang, L.-P. Wang, M. Brauner, J. F. Liewald, K. Kay, N. Watzke, P. G. Wood, E. Bamberg, G. Nagel, A. Gottschalk, and K. Deisseroth, "Multimodal fast optical interrogation of neural circuitry," Nature **446**, 633–639 (2007).
4. F. Zhang, M. Prigge, F. Beyrire, S. P. Tsunoda, J. Mattis, O. Yizhar, P. Hegemann, and K. Deisseroth, "Red-shifted optogenetic excitation: a tool for fast neural control derived from volvox carteri," Nat. Neurosci. **11**, 631–633 (2008).
5. J. Y. Lin, M. Z. Lin, P. Steinbach, and R. Y. Tsien, "Characterization of engineered channelrhodopsin variants with improved properties and kinetics," Biophys. J. **96**, 1803–1814 (2009).
6. E. S. Boyden, F. Zhang, E. Bamberg, G. Nagel, and K. Deisseroth, "Millisecond-timescale, genetically targeted optical control of neural activity," Nat. Neurosci. **8**, 1263–1268 (2005).
7. X. Li, D. V. Gutierrez, M. G. Hanson, J. Han, M. D. Mark, H. Chiel, P. Hegemann, L. T. Landmesser, and S. Herlitze, "Fast noninvasive activation and inhibition of neural and network activity by vertebrate rhodopsin and green algae channelrhodopsin," Proc. Natl. Acad. Sci. U. S. A. **102**, 17816–17821 (2005).

#174062 - $15.00 USD Received 9 Aug 2012; revised 18 Oct 2012; accepted 23 Oct 2012; published 1 Nov 2012

8. T. Ishizuka, M. Kakuda, R. Araki, and H. Yawo, "Kinetic evaluation of photosensitivity in genetically engineered neurons expressing green algae light-gated channels," Neurosci. Res. **54**, 85–94 (2006).
9. G. Nagel, M. Brauner, J. F. Liewald, N. Adeishvili, E. Bamberg, and A. Gottschalk, "Light activation of channelrhodopsin-2 in excitable cells of caenorhabditis elegans triggers rapid behavioral responses," Curr. Biol. **15**, 2279–2284 (2005).
10. J. Wells, C. Kao, K. Mariappan, J. Albea, E. D. Jansen, P. Konrad, and A. Mahadevan-Jansen, "Optical stimulation of neural tissue in vivo," Opt. Lett. **30**, 504–506 (2005).
11. R. Fork, "Laser stimulation of nerve cells in Aplysia," Science **171**, 907–908 (1971).
12. J. Wells, C. Kao, E. D. Jansen, P. Konrad, and A. Mahadevan-Jansen, "Application of infrared light for in vivo neural stimulation," J. Biomed. Opt. **10**, 064003 (2005).
13. A. Izzo, J. Walsh, E. Jansen, M. Bendett, J. Webb, H. Ralph, and C.-P. Richter, "Optical parameter variability in laser nerve stimulation: A study of pulse duration, repetition rate, and wavelength," IEEE T. Bio-Med. Eng. **54**, 1108–1114 (2007).
14. M. W. Jenkins, A. R. Duke, S. Gu, Y. Doughman, H. J. Chiel, H. Fujioka, M. Watanabe, E. D. Jansen, and A. M. Rollins, "Optical pacing of the embryonic heart," Nat. Photonics. **4**, 623–626 (2010).
15. J. M. Cayce, R. M. Friedman, E. D. Jansen, A. Mahavaden-Jansen, and A. W. Roe, "Pulsed infrared light alters neural activity in rat somatosensory cortex in vivo," Neuroimage **57**, 155–166 (2011).
16. N. Fried, S. Rais-Bahrami, G. Lagoda, A.-Y. Chuang, L.-M. Su, and A. Burnett, "Identification and imaging of the nerves responsible for erectile function in rat prostate, in vivo, using optical nerve stimulation and optical coherence tomography," IEEE J. Sel. Topics in Quantum Electron. **13**, 1641–1645 (2007).
17. J. Wells, C. Kao, P. Konrad, T. Milner, J. Kim, A. Mahadevan-Jansen, and E. D. Jansen, "Biophysical mechanisms of transient optical stimulation of peripheral nerve," Biophys. J. **93**, 2567–2580 (2007).
18. M. G. Shapiro, K. Homma, S. Villarreal, C.-P. Richter, and F. Bezanilla, "Infrared light excites cells by changing their electrical capacitance," Nat. Commun. **3**, 736 (2012).
19. J. Yao, B. Liu, and F. Qin, "Rapid temperature jump by infrared diode laser irradiation for patch-clamp studies," Biophys. J. **96**, 3611–3619 (2009).
20. J. G. Bernstein, P. A. Garrity, and E. S. Boyden, "Optogenetics and thermogenetics: technologies for controlling the activity of targeted cells within intact neural circuits," Curr. Opin. Neurobiol. **22**, 61–71 (2012).
21. A. C. von Philipsborn, T. Liu, J. Y. Yu, C. Masser, S. S. Bidaye, and B. J. Dickson, "Neuronal control of drosophila courtship song," Neuron **69**, 509–522 (2011).
22. N. C. Peabody, J. B. Pohl, F. Diao, A. P. Vreede, D. J. Sandstrom, H. Wang, P. K. Zelensky, and B. H. White, "Characterization of the decision network for wing expansion in drosophila using targeted expression of the TRPM8 channel," J. Neurosci. **29**, 3343–3353 (2009).
23. H. Takahashi, T. Sakurai, H. Sakai, D. J. Bakkum, J. Suzurikawa, and R. Kanzaki, "Light-addressed single-neuron stimulation in dissociated neuronal cultures with sparse expression of ChR2." BioSystems **107**, 106–112 (2011).
24. N. Grossman, V. Poher, M. S. Grubb, G. T. Kennedy, K. Nikolic, B. McGovern, R. B. Palmini, Z. Gong, E. M. Drakakis, M. A. A. Neil, M. D. Dawson, J. Burrone, and P. Degenaar, "Multi-site optical excitation using ChR2 and micro-LED array," J. Neural Eng. **7**, 016004 (2010).
25. O. Yizhar, L. Fenno, T. Davidson, M. Mogri, and K. Deisseroth, "Optogenetics in neural systems," Neuron **71**, 9–34 (2011).
26. A. Vogel and V. Venugopalan, "Mechanisms of pulsed laser ablation of biological tissues," Chem. Rev. **103**, 577644 (2003).
27. T. Durduran, R. Choe, W. B. Baker, and A. G. Yodh, "Diffuse optics for tissue monitoring and tomography," Reports on Progress in Physics **73**, 076701 (2010).
28. L. Fenno, O. Yizhar, and K. Deisseroth, "The development and application of optogenetics," Annu. Rev. Neurosci. **34**, 389–412 (2011).
29. A. M. Aravanis, L.-P. Wang, F. Zhang, L. A. Meltzer, M. Z. Mogri, M. B. Schneider, and K. Deisseroth, "An optical neural interface: in vivo control of rodent motor cortex with integrated fiberoptic and optogenetic technology," J. Neural Eng. **4**, S143 (2007).
30. A. R. Adamantidis, F. Zhang, A. M. Aravanis, and K. D. L. de Lecea, "Neural substrates of awakening probed with optogenetic control of hypocretin neurons," Nature **450**, 420–424 (2007).
31. F. Zhang, V. Gradinaru, A. R. Adamantidis, R. Durand, R. D. Airan, L. De Lecea, and K. Deisseroth, "Optogenetic interrogation of neural circuits: technology for probing mammalian brain structures." Nat. Protoc. **5**, 439–456 (2010).
32. A. V. Kravitz and A. C. Kreitzer, "Optogenetic manipulation of neural circuitry in vivo." Curr. Opin. Neurobiol. **21**, 433–439 (2011).
33. A. V. Kravitz, B. S. Freeze, P. R. L. Parker, K. Kay, M. T. Thwin, K. Deisseroth, and A. C. Kreitzer, "Regulation of parkinsonian motor behaviours by optogenetic control of basal ganglia circuitry," Nature **466**, 622–626 (2010).
34. P. Anikeeva, A. S. Andalman, I. Witten, M. Warden, I. Goshen, L. Grosenick, L. A. Gunaydin, L. M. Frank, and K. Deisseroth, "Optetrode: a multichannel readout for optogenetic control in freely moving mice," Nat. Neurosci. **15**, 163–170 (2012).

#174062 - $15.00 USD Received 9 Aug 2012; revised 18 Oct 2012; accepted 23 Oct 2012; published 1 Nov 2012

35. J. Wang, F. Wagner, D. A. Borton, J. Zhang, I. Ozden, R. D. Burwell, A. V. Nurmikko, R. van Wagenen, I. Diester, and K. Deisseroth, "Integrated device for combined optical neuromodulation and electrical recording for chronic in vivo applications," J. Neural Eng. **9**, 016001 (2012).
36. J. Zhang, F. Laiwalla, J. A. Kim, H. Urabe, R. V. Wagenen, Y.-K. Song, B. W. Connors, F. Zhang, K. Deisseroth, and A. V. Nurmikko, "Integrated device for optical stimulation and spatiotemporal electrical recording of neural activity in light-sensitized brain tissue," J. Neural Eng. **6**, 055007 (2009).
37. S. Royer, B. V. Zemelman, M. Barbic, A. Losonczy, G. Buzski, and J. C. Magee, "Multi-array silicon probes with integrated optical fibers: light-assisted perturbation and recording of local neural circuits in the behaving animal." Eur. J. Neurosci. **31**, 2279–2291 (2010).
38. V. Gradinaru, K. R. Thompson, F. Zhang, M. Mogri, K. Kay, M. B. Schneider, and K. Deisseroth, "Targeting and readout strategies for fast optical neural control in vitro and in vivo." J. Neurosci. **27**, 14231–14238 (2007).
39. E. Stark, T. Koos, and G. Buzski, "Diode probes for spatiotemporal optical control of multiple neurons in freely moving animals," J. Neurophysiol. **108**, 349–363 (2012).
40. A. N. Zorzos, E. S. Boyden, and C. G. Fonstad, "Multiwaveguide implantable probe for light delivery to sets of distributed brain targets," Opt. Lett. **35**, 4133–4135 (2010).
41. T. V. F. Abaya, M. Diwekar, S. Blair, P. Tathireddy, L. Rieth, G. A. Clark, and F. Solzbacher, "Characterization of a 3D optrode array for infrared neural stimulation," Biomed. Opt. Express **3**, 2200–2219 (2012).
42. T. V. F. Abaya, M. Diwekar, S. Blair, P. Tathireddy, L. Rieth, G. A. Clark, and F. Solzbacher, "Optical characterization of the utah slant optrode array for intrafascicular infrared neural stimulation," Proc. SPIE **8207**, 82075M (2012).
43. G. A. Clark, S. L. Schister, N. M. Ledbetter, D. J. Warren, F. Solzbacher, J. D. Wells, M. D. Keller, S. M. Blair, L. W. Rieth, and P. R. Tathireddy, "Selective, high-optrode-count, artifact-free stimulation with infrared light via intrafascicular utah slanted optrode arrays," Proc. SPIE **8207**, 82075I (2012).
44. R. Bhandari, S. Negi, L. Rieth, and F. Solzbacher, "A wafer-scale etching technique for high aspect ratio implantable mems structures," Sens. Actuators, A **162**, 130–136 (2010).
45. P. Srinivasan, J. Fred R. Beyette, and I. Papautsky, "Micromachined arrays of cantilevered glass probes," Appl. Opt. **43**, 776–782 (2004).
46. M. Bass, C. DeCusatis, G. Li, V. Mahajan, J. Enoch, and E. Stryland, *Handbook of Optics: Optical properties of materials, nonlinear optics, quantum optics* (McGraw-Hill, 2009).
47. *Cargille Laboratories Refractive Index Fluid Typical Characteristics Sheet.*
48. V. Tuchin, *Handbook of optical biomedical diagnostics* (SPIE Press, 2002).
49. D. Mynbaev and L. Scheiner, *Fiber-optic communications technology* (Prentice Hall, 2001).
50. H. Bennett, "Scattering characteristics of optical materials," Opt. Eng. **17**, 480–488 (1978).
51. N. Farah, I. Reutsky, and S. Shoham, "Patterned optical activation of retinal ganglion cells," in *Proceedings of the International Conference of the IEEE Engineering in Medicine and Biology Society,* (IEEE, 2007), pp. 6368–6370.
52. C. Lutz, T. S. Otis, V. DeSars, S. Charpak, D. A. DiGregorio, and V. Emiliani, "Holographic photolysis of caged neurotransmitters," Nat. Methods **5**, 821–827 (2008).
53. V. Poher, N. Grossman, G. T. Kennedy, K. Nikolic, H. X. Zhang, Z. Gong, E. M. Drakakis, E. Gu, M. D. Dawson, P. M. W. French, P. Degenaar, and M. A. A. Neil, "Micro-LED arrays: a tool for two-dimensional neuron stimulation," J. Phys. D: Appl. Phys. **41**, 094014 (2008).

1. Introduction

Optical methods are well established in the fields of neuroscience, medical imaging and diagnostics, etc. Optogentics, for example, despite being a nascent field of study, was named the "Method of the Year 2010" by Nature Methods. Optogenetics is an approach to trigger gain or loss of function of explicit events in specific cells in tissue with temporal precision in the millisecond-scale, which is achieved through the use of light-sensitive control tools that may be targeted by gene delivery [1]. The control tools are mainly light-gated ion channels in the microbial opsin family; microbial opsins characterized for optogenetics include channelrodopsin-2 (ChR2; responsive to blue light for neuronal excitation), halorhodopsin (NpHR; responsive to yellow light for inhibition), channelrhodopsin from *Volvox carteri* (VChR; activated by green light), and ChR2 chimeras [2–5]. Optogenetics was first demonstrated using ChR2 in scattered hippocampal neurons in mammalian brain; non-invasive delivery of brief pulses of blue light prompted neuronal depolarization at the resolution of single spikes [6]. Similar experiments validating optogenetic induction of action potentials and control of synaptic transmission followed [7–9].

#174062 - $15.00 USD Received 9 Aug 2012; revised 18 Oct 2012; accepted 23 Oct 2012; published 1 Nov 2012

A method of optical excitation without requiring genetic manipulation is infrared neural stimulation (INS), where IR is applied as input energy. Like all other optical stimulation techniques, INS does not produce signal artifacts in electrical recordings due to the absence of direct charge injection [10]. Nerve stimulation with infrared light at 1064 nm was demonstrated in Aplysia in 1971 [11], but INS was first systematically analyzed in 2005 using rat sciatic nerve [10, 12]. In these experiments, a laser-coupled 600-μm optical fiber emitted a pulsed laser beam on a single spot on the sciatic nerve surface. Stimulation and ablation fluence thresholds were determined for several wavelengths between 2.1 and 6.1 μm; wavelengths with lower absorption coefficients had larger safety margins, while those having high absorption only stimulated at energies above the damage threshold. Other applications (e.g., stimulation of the cochlea, embryonic heart pacing) emerged using non-contact delivery of pulsed light via fibers as well [13–16]. Wavelengths of $\sim$1.87 and 2.12 μm, which exhibit similar absorption characteristics, have been extensively used across different applications, but other types of tissue may require different wavelengths for optimal stimulation such that the optical penetration depth is matched to the targeted excitable tissue. INS is believed to act via the induction of a spatio-temporal heat gradient in tissue [17], although the underlying physiological mechanism is still under investigation [18]. Infared-triggered temperature changes have been demonstrated to activate thermal transient receptor potential (TRP) ion channels [19], which can be genetically targeted to perform thermogenetic stimulation (similar to rhodopsins for optogenetic stimulation); these TRP channels are $\sim 1000\times$ more sensitive than optogenetic tools (i.e., lower expression levels required) and have mainly been useful in the study of the relationship between specific neuronal activation to behavioral outputs in fruit flies, which does not require high temporal resolution [20–22].

For highly effective optical stimulation, development of light delivery techniques is necessary to further effect deep tissue targets, utilize lower input energy and provide different spatio-temporal activation patterns; likely solutions include tissue penetration and use of more than one light guide or source during stimulation. In separate studies, light from an Argon laser projected through a digital micro-mirror device (DMD) and an array of high power micro light-emitting diodes (micro-LED) generated patterned excitation of neuronal slices expressing ChR2 [23, 24]. Still, these patterns were incident on the sample surface. The intrinsic tissue absorption and scattering limit light penetration to $\sim$1 mm and require higher energies at the surface to maintain threshold stimulation levels within the target volume underneath. Research with the mammalian brain with illumination at $\lambda = 473$ on the brain surface from a 100-μm fiber of 0.22 NA estimates that the irradiance decreases rapidly to 10% of the value on the surface within only 300 μm depth [25]. Fig. 1 plots a typical tissue attenuation spectrum, which is the combined scattering and absorption. Scattering is typically described by a combination of Rayleigh and Mie scattering; Rayleigh scattering scales as $1/\lambda^4$, while the scaling of Mie scattering is generally inverse with wavelength, with the power determined by the effective particle size. Tissue absorption is dominated by amino acids, nucleic acids, and fats below 450-nm wavelength, while absorption is dominated by (oxy)hemoglobin and melanin between 450 and 700 nm; beyond about 1400 nm, the dominant chromophore is water [26]. Overall, scattering dictates the light transport for wavelengths in the visible range, while water absorption prevails in the infrared. Although wavelengths in the near-IR window of 650-950 nm have been used in imaging to reach centimeters below the tissue surface due to very low absorption, the dominant scattering effect makes the detected signal at those depths very weak; spatial and temporal information about tissue activity and composition can still be determined as the techinique relies on variations in absorption and scattering within the volume [27]. This method, which is statistically modeled as a diffusion process, cannot be applied in optical stimulation mainly due to two reasons: (1) the wavelength range is not suitable for either optogenetics and INS, and (2)

#174062 - $15.00 USD Received 9 Aug 2012; revised 18 Oct 2012; accepted 23 Oct 2012; published 1 Nov 2012

most results are gathered from scattering data whereas the intensity of light concentrated in a defined area is of interest in optical stimulation. Indeed, higher light intensity incident on cells expressing channelrhodopsin variants result in higher levels of action potential recordings [5]. Results of extraneural INS also reveal that effective stimulation in tissue requires wavelengths at relative valleys of the absorption spectrum; wavelengths having approximately zero penetration depths easily created nerve damage with threshold stimulation fluence, and wavelengths with very low absorption (i.e., absolute valleys in the spectrum) will likely fail to deliver sufficient amounts of energy to evoke a response [12].

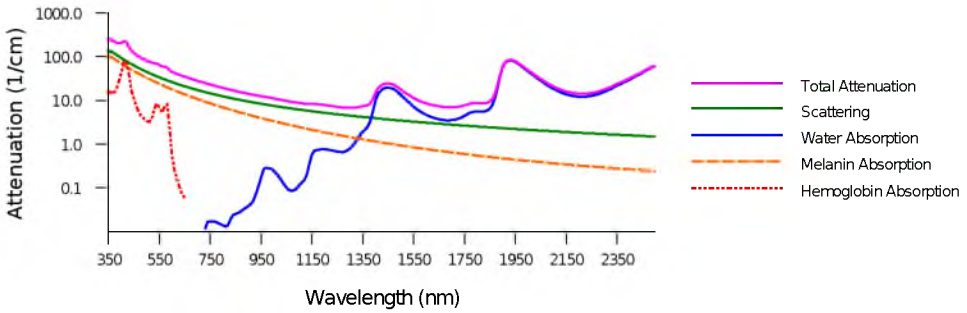

Fig. 1. Tissue attenuation spectrum. Light transport of wavelengths in the visible range is more strongly affected by scattering, while absorption is dominant in the infrared. Penetration depth (i.e., depth where intensity falls to $1/e$ of surface value) is limited to about 1 mm.

To circumvent tissue attenuation, penetrating optical probes have been designed. In the field of optogenetics, visible light has most commonly been delivered *in vivo* via a single laser-coupled optical fiber [28]. A 200-μm multimode fiber inserted through a cannula guide has been used for photostimulation of deep brain structures in freely moving mice [29–31]. For simultaneous awake stimulation and recording, an optical fiber through a zirconia ferrule was attached to a microwire array [32]. Similar commercially available optical probe packages, such as those from NeuroNexus (50 or 105-μm core fiber attached to a linear silicon probe with 16 electrical recording sites) [33], and an optetrode consisting of four microwires surrounding a multimode optical fiber [34] were also utilized successfully. Use of tapered optical fibers has been reported as well. A sharpened 50-μm fiber coated with gold was inserted in mouse brain slices to trigger localized epileptiform events; the same optrode was later integrated into a recording silicon multi-electrode array, replacing the center electrode for optical excitation of cells in a single cortical site [35, 36]. To provide 2D spatio-temporal control over multiple sites, tapered fibers were glued to a linear array of 4 or 8 commercially available planar silicon probes [37], which are an alternative to tungsten electrodes utilized in similar studies [38]. Experiments with ChR2-transfected rat hippocampus using these 2D arrays demonstrated multiple local stimulation with extensive recording of neurons. Optical and spatiotemporal stimulation characteristics of a 2D array of diode-coupled 50-μm tapered fibers in freely moving rat was presented as well [39]. Multi-site stimulation using a microfabricated multiwaveguide probe has also been proposed [40]. The device consists of parallel independent single-mode rectangular waveguides of silicon oxynitride core and oxide cladding that converge into a single probe; the paths end at different target depths along the probe axis and side-fires using a corner aluminum mirror. Transmission efficiencies are in the range of 23 to 33% as determined from bench testing.

For INS, a microfabricated 3D silicon waveguide array has been characterized [41, 42]. The 10×10 array has tapered microneedles with lengths varying in one direction from 0.5 mm to

#174062 - $15.00 USD Received 9 Aug 2012; revised 18 Oct 2012; accepted 23 Oct 2012; published 1 Nov 2012

1.5 mm in a 400-μm pitch. Its architecture provides intrafascicular access across the width and depth of the peripheral nerve. Light input from an optical fiber was coupled to the backside and output was recorded from the tips. Normalized output power ranged from 0.23 to 0.35 with longer optrodes performing at higher efficiencies; output beams had a nominal beam width and far-field full-angle divergence of 55 μm and 17°, respectively [41]. Despite the low efficiency, optrodes were able to stimulate responses in cat sciatic nerve [43]. Different optrodes activated different muscles and exhibited selectivity between different muscles innervated by different nerve branches (e.g. tibialis anterior and gastrocnemius (MG/LG)), between different muscles innervated by the same nerve branch (e.g. MG/LG and soleus (SOL) from the tibial nerve) and between presumed same nerve fascicle (e.g. MG and SOL). Comparable within-branch selectivity has not been reported for extraneural INS.

In this paper, we present a first-generation 3D glass penetrating waveguide array, which can be used for both optogenetics and INS for high-channel count patterned stimulation of independent neuron subpopulations. Two-level stimulation and flood illumination of multiple optrodes with overlapping output beams to effect a wider plane in tissue is possible as well. With these SiO_2 optrode arrays, nearly all modes of optical excitation (e.g., visible, infrared, multi-photon excitation) can be achieved with the penetration depth determined by the optrode length and not by wavelength. The device has application in basic and applied neuroscience research (e.g., studying information processing, neural control prosthetics), as well as in highly selective photodynamic therapy and deep tissue imaging for diagnostics and therapy. Detailed characterization of the optrode array is reported in this work. Note that optrode design features such as length, width, tip angle and spacing can be modified to suit a specific application.

2. Glass optrode array

The SiO_2 optrode array described in this paper consists of waveguide probes of constant length in a 10×10 grid with a 400-μm pitch. The optrodes, which have been fabricated in lengths ranging from 0.5 to 2-mm, are rectangular columns with pyramidal tips. The array is set upon a 1-mm thick backplane. Fig. 2 shows scanning electron micrographs of the glass array. Each optrode receives light from an aligned light source (e.g., edge-coupled optical fiber, collimated beam) to the backside; optrode tips emit light that is locally delivered to tissue. The backplane in between optrodes may also allow light to pass through for shallower targets.

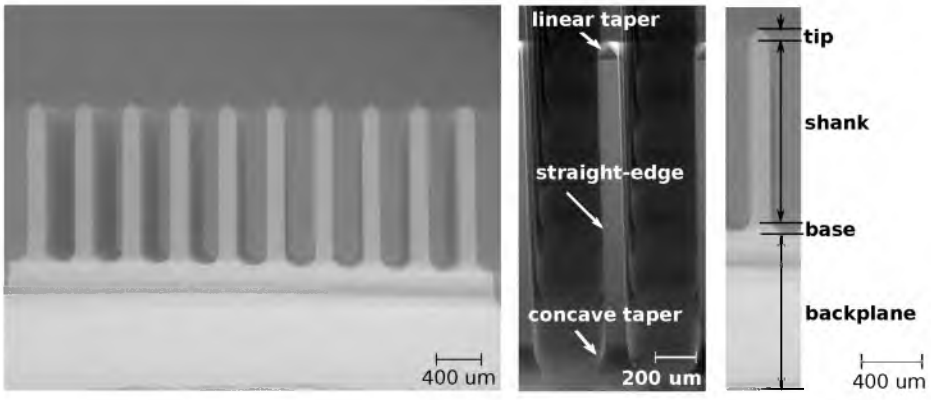

Fig. 2. SEM image of a 3D optrode array made from glass. (a) 10×10 rows of 1.5-mm long and 150-μm wide optrodes. (b) Profile of optrode geometry. (c) Definition of optrode sections along path of light propagation: 1-mm backplane, base extending 100 μm into straight-edge shank and 120-μm long linearly tapered tip.

#174062 - $15.00 USD Received 9 Aug 2012; revised 18 Oct 2012; accepted 23 Oct 2012; published 1 Nov 2012

2.1. *Fabrication*

Fabrication of these 3D glass arrays rely heavily on bulk-micromachining. Glass (fused silica or quartz) wafers with 3-mm thickness and 50-mm diameter are used as substrates; such material allows transmission of wavelengths both within the visible spectrum and the near-IR range. One wafer yields 23 arrays.

2.1.1. Tip formation

The tips were formed using a Disco DAD 640 dicing saw with a bevel blade. The blade is essentially a v-shaped blade with its vertex clipped into a flat that separates the bevels. The angle of the bevel defines the tip taper angle (i.e., angle of taper with respect to the optical axis). Shallow cuts spaced 400 μm apart (i.e. optrode spacing) were made on the wafer surface in orthogonal directions; each cut creates a face of the pyramidal tip on two adjacent optrodes. Fig. 3 shows the initial array structure after bevel dicing. Here, each face of the pyramidal tip tapers off at 45°.

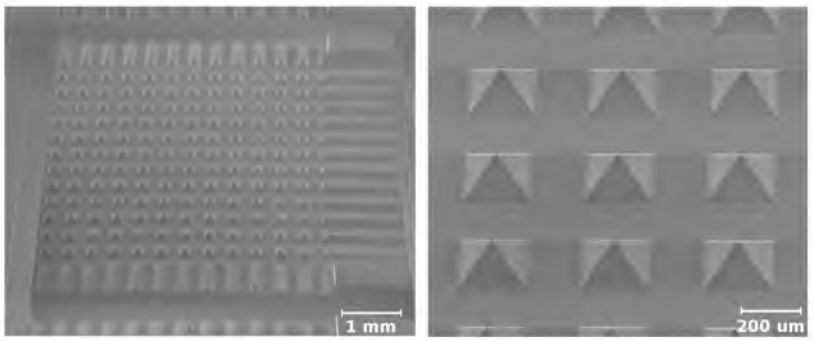

(a) (b)

Fig. 3. Array after bevel dicing (a) to form pyramidal tips (b).

Note that the tips of these glass optrodes were shaped with dicing rather than the etching technique in silicon optrodes fabrication [41, 44]. Etching silicon can be a diffusion-limited process; as the etching reaction proceeds, the byproducts impede the etchant interaction with the shank surface within the array such that the more exposed column tips are preferentially etched. In glass however, the much slower etch rate (one-tenth of the Si etch rate) creates a reaction-limited process that uniformly etches the optrode along its length and thus does not sharpen the tips.

2.1.2. Shank dicing

The shanks were then defined by column dicing; deep kerfs were made in between the pyramids to create rectangular pillars. An extra row on all sides of each array is placed to maintain uniformity in optrode geometry within the 10×10 grid during subsequent wet etching. The average column width after dicing was $240\pm15\mu$m. The resulting optrode architecture consists of a pyramid atop a rectangular shank, as pictured in Fig. 4.

2.1.3. Etching

Etching the arrays thins the shanks. The dynamic etching technique of the Utah Electrode Array was adapted [44]. The glass wafer was secured with wax onto a Teflon sheet, which was screwed on a Teflon base plate. The wafer was then immersed with columns facing down into 1500 ml of 49% HF; the wafer was rotated clockwise at (22 rpm) at the same time a magnetic

#174062 - $15.00 USD Received 9 Aug 2012; revised 18 Oct 2012; accepted 23 Oct 2012; published 1 Nov 2012

Fig. 4. Shank formation. Array after column dicing (a) has optrodes with pyramidal tips atop rectangular shanks (b). Array after etching (c) has thinner optrodes with the same shape as before.

stirrer in the solution was propelled counter-clockwise (500 rpm). The stirring action allow the continuous, aggresive etching of the high aspect ratio optrodes that minimizes surface scalloping by preventing the accumulation of the byproducts that tend to precipitate on the sidewalls. The etch rate is about 2.5 μm/min at room temperature. Fig. 4(a) shows the thinned optrodes having the same shape as before etching.

2.1.4. Annealing

The wafer was annealed at 1150°C for 6 hours to further reduce surface roughness of the shanks that resulted from both dicing and etching [45]. Surface roughness must be minimized to avoid significant scattering loss for light transmission. Annealing also relieves internal stresses in the glass. Fig. 5 shows a sample glass surface before and after annealing; etching produces the scalloping, which is greatly reduced by subjecting the arrays to the anneal temperature at extended hold times. The resulting RMS surface roughness was measured by atomic force microscopy (AFM) as 22 nm.

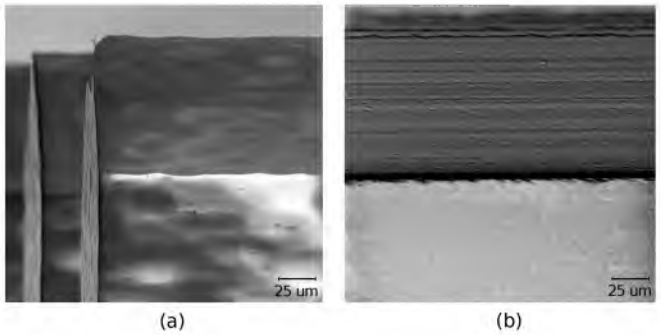

Fig. 5. Side-by-side comparison of same glass surface after dicing and HF wet etching (a), and subsequently after annealing (b) to reduce surface roughness. RMS surface roughness after annealing is measured as 22 nm by AFM.

2.1.5. Singulation

The extra rows acting as sacrificial features were diced out using a resin blade to yield 10×10 arrays. Individual arrays were finally separated from the wafer by dicing through the backside. Fig. 2(a) shows a singulated array.

#174062 - $15.00 USD Received 9 Aug 2012; revised 18 Oct 2012; accepted 23 Oct 2012; published 1 Nov 2012

3. Theoretical loss mechanisms

System losses in the optrode are expected to include Fresnel reflectance (R), coupling, back-reflection and scattering. Reflection inside the optrode tips is suspected to be the dominant loss mechanism, especially since the tapered tip of silicon optrodes has been determined as the major contributor of loss in silicon arrays [41]. Fig. 6 shows where each type of loss occurs. The source power P_{in} reduces to $P_{in}^{'}$ by the transmittance $T_i = (1 - R_i)$ upon entering the glass backplane. The power exiting the optrode tips is P_{out}. P_{back} and P_{base} are radiation losses that constitute part of the coupling loss; the power coupled into the shanks is $P_{coupled}$. P_{ref} is the lump sum of reflected power towards the source from all sections within the device, while P_{scat} is the scattering loss due to the sidewall roughness. Absorption loss is assumed negligible. The variables are related through

$$P_{in} \times (1 - R_i) = P_{in}^{'} = P_{back} + P_{base} + P_{out} + P_{ref} + P_{scat}.$$

The glass optrodes do not suffer from radiation loss through the shanks unlike tapered silicon optrodes [41]. Consequently, glass optrodes of different lengths are expected to exhibit the same transmission efficiency because there is no taper slope difference to consider.

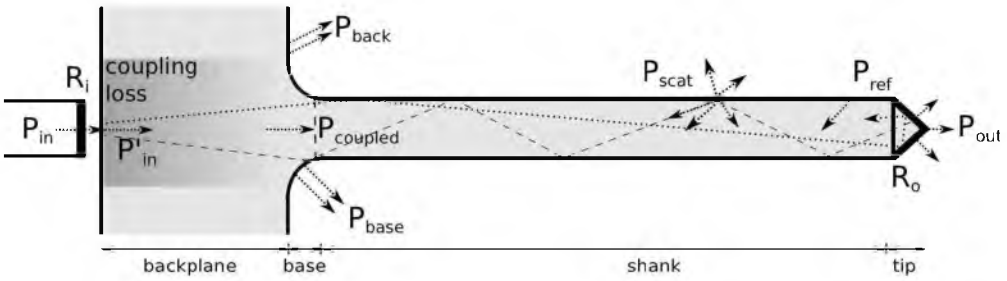

Fig. 6. Loss mechanisms within the glass optrode include Fresnel reflectance ($R_{i/o}$), coupling, backreflection and scattering.

3.1. *Fresnel reflections*

Refractive index contrast between the array and the surrounding medium (e.g., air, tissue) results in Fresnel reflection at the optrode backside and tip (i.e., input and output interfaces). Table 1 lists relevant refractive indices (n) at visible and near-IR wavelengths. Although an in-coupling optical fiber closely matches the index of the glass array, it leaves an air gap junction with the array backside during edge-coupling; the gap forms a double interface that suffers from a larger Fresnel reflection loss. Table 2 shows approximate reflectance values as computed from

$$R = \left(\frac{n_1 - n_2}{n_1 + n_2}\right)^2 \tag{1}$$

and

$$R_{\text{eff}} = 1 - (1 - R_1)(1 - R_2) = R_1 + R_2 - R_1 R_2$$

for single and double interfaces, respectively. Variables n_1 and n_2 are the refractive indices on either side of the interfaces, while R_1 and R_2 are determined from Eq. 1. As computed, the loss due to Fresnel reflection is relatively small and may further be reduced with the use of index matching fluid at the input side to fill the air gap.

#174062 - $15.00 USD Received 9 Aug 2012; revised 18 Oct 2012; accepted 23 Oct 2012; published 1 Nov 2012

Table 1. Refractive Indices at Visible and Near-IR Wavelengths.

Material	$n_{visible}$	$n_{near-IR}$	Reference
Air	1.00	1.00	
Fused silica (optrode/fiber)	1.46	1.44	[46]
Quartz (optrode)	1.54	1.52	[46]
Index matching fluid	1.45	1.44	[47]
Tissue	1.36	1.36	[48]

Table 2. Nominal Reflectance at Interfaces

Interface	Reflectance (R)	Transmittance (1-R)
Fiber - Air - Optrode	0.065	0.935
Fiber - Index fluid - Optrode	0.001	0.999
Optrode - Tissue	0.004	0.996
Optrode - Air	0.034	0.966

3.2. *Coupling loss*

Mismatch and misalignment between the optical source and the optrode waveguide result in coupling losses. Mismatch is considered an intrinsic loss caused by differences in core cross-sectional area (A) and numerical aperture (NA); the coupling efficiency (η) accounting for these losses are presented in most textbooks in fiber optics [49]. For a fiber coupled to an optrode for instance,

$$\eta_A = \frac{A_O}{A_F} \tag{2}$$

and

$$\eta_{\mathrm{NA}} = \left(\frac{\mathrm{NA_O}}{\mathrm{NA_F}}\right)^2, \tag{3}$$

where the subscripts O and F indicate the optrode and fiber, respectively. Misalignment arises as an extrinsic loss from lateral and angular displacement as well as end separation. Using lenses may couple more light into the optrode, but bench testing results in this paper were extracted by direct-coupling the source to the optrode for simplicity.

3.3. *Scattering*

Surface scattering may also contribute to transmission losses within the optrode. The amplitude and the spatial periodicity of the sidewall roughness after dicing and etching cannot be completely eliminated by annealing and thus may attenuate guided mode propagation due to light scattering. The concept of total integrated scatter (TIS) mathematically models the total amount of light scattered by a surface from a single reflection as [50]

$$TIS = R\left\{1 - exp\left[-\left(\frac{4\pi\sigma \cdot cos(\theta_i)}{\lambda}\right)^2\right]\right\}, \tag{4}$$

where R is the theoretical surface reflectance (100% under total internal reflection conditions), σ is the RMS surface roughness, θ_i is the incidence angle of the ray with respect to the normal of the surface, and λ is the wavelength. This equation suggests that: reflective surfaces inherently scatter more light, shorter wavelengths scatter more than longer wavelengths, and maximum scattering occurs when light strikes the surface at normal incidence.

#174062 - $15.00 USD Received 9 Aug 2012; revised 18 Oct 2012; accepted 23 Oct 2012; published 1 Nov 2012

TIS will accumulate based on the total number of reflections experienced during propagation, which may be estimated for a meridional ray in a straight waveguide as

$$N_R = \frac{L}{t \cdot cot(\theta_m)}. \tag{5}$$

where L is the length of the waveguide, t is its thickness, and $\theta_m = 90^\circ - \theta_i$ is the ray propagation angle with respect to the optical axis. For a ~100 micron-sized waveguide, the number of reflections is limited; smooth sidewalls then contribute to little surface scattering. However, when inserted into tissue, inhomogeneity at the optrode-tissue interface will contribute to additional scattering loss.

3.4. Total internal reflection in the tips

With the use of smaller fibers from which a large fraction of the light will be coupled into the shank, backreflected power is expected to come from the tips (additional backreflection will result from the backplane and the base when using larger diameter beams). Due to the tapered geometry of the tips, not all rays will be able to exit and instead reflect back towards the source. The angle of total internal reflection (TIR) for the glass-air interface is about 40°.

4. Optical characterization results and discussion

Output from the optrode tips was measured and profiled in air. In most measurements, a single bare fiber was mechanically aligned to the array backside through an intervening medium of $n \approx 1.45$; the matching index medium eliminates the air gap (i.e., reflection losses) resulting from the fiber being only in contact with (i.e., not attached to) the array. The fiber is moved from one optrode to the next across the array, with the optrode tips inserted through aluminum foil, as shown in Fig. 7(a); the foil blocks radiation and scattering from the shank, base and backplane. Fig. 7(b) is a similar setup, except the foil is brought up to the backplane to expose the shanks during the measurements; this allows collection of any scattered light from the shank. Power from collimated beams was also coupled into the optrode shanks, but transmission through the backplane in between optrodes was assessed by removing the foil, as illustrated in Fig. 7(c). Three fiber-coupled lasers at wavelengths 640 nm, 1550 nm and 1875 nm, and a white light source provided the optical input. Planar photodetectors, an integrating sphere or a beam profiler collected the output in various experimental setups. Output power is normalized with respect to the power of the beam incident on the optrode backside.

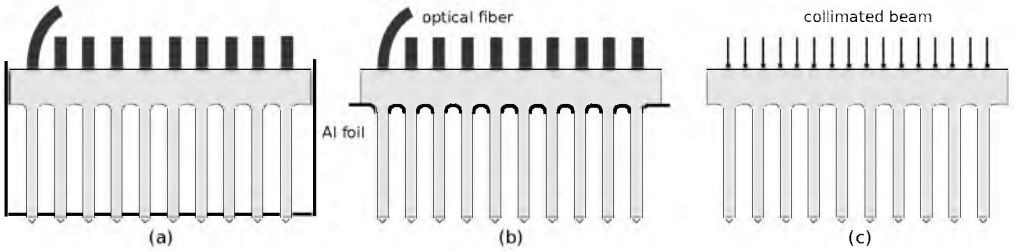

Fig. 7. Experimental Setup. (a) Determining output power and beam profile from optrode tips using in-coupling fibers. (b) Determining output power from optrode shanks and tips using in-coupling fibers to estimate shank losses. (c) Measuring transmission through optrode tips and array backplane using a collimated beam.

#174062 - $15.00 USD Received 9 Aug 2012; revised 18 Oct 2012; accepted 23 Oct 2012; published 1 Nov 2012

4.1. *Coupling from different fiber sizes*

Fused silica fibers with 0.22 NA and core diameters 50, 105, 200 and 400 μm coupled the optical source to optrodes having 150-μm wide, 1.5-mm long shanks and 45° tip taper. The setup in Fig. 7(a) was first utilized. Transmission about the visible spectrum (e.g., 375 - 750 nm) through the optrodes was quantified by using a broadband light source as input and an integrating sphere attached to a spectrometer as readout interface. Discrete wavelengths were also transmitted and the power emitted by the optrode tip was measured with corresponding photodetectors positioned normal to the optrode shank. Fig. 8 plots the resulting normalized output power from the tips with using different in-coupling fibers. The highest transmission attained is about 71% for fiber sizes less than the shank cross-sectional area. The scaling down of the output power with larger fibers follows the fraction of Eq. 2, which puts a limit on the amount of power coupled into the shanks from the incident beam. The optrode arrays transmit the spectrum from visible to near-IR approximately with the same efficiency. Note that optrodes implanted in tissue are likely to exhibit a slightly higher efficiency as the lower refractive index mismatch causes a decrease in output Fresnel reflectance and an increase in the critical angle to allow more power to exit out the tips.

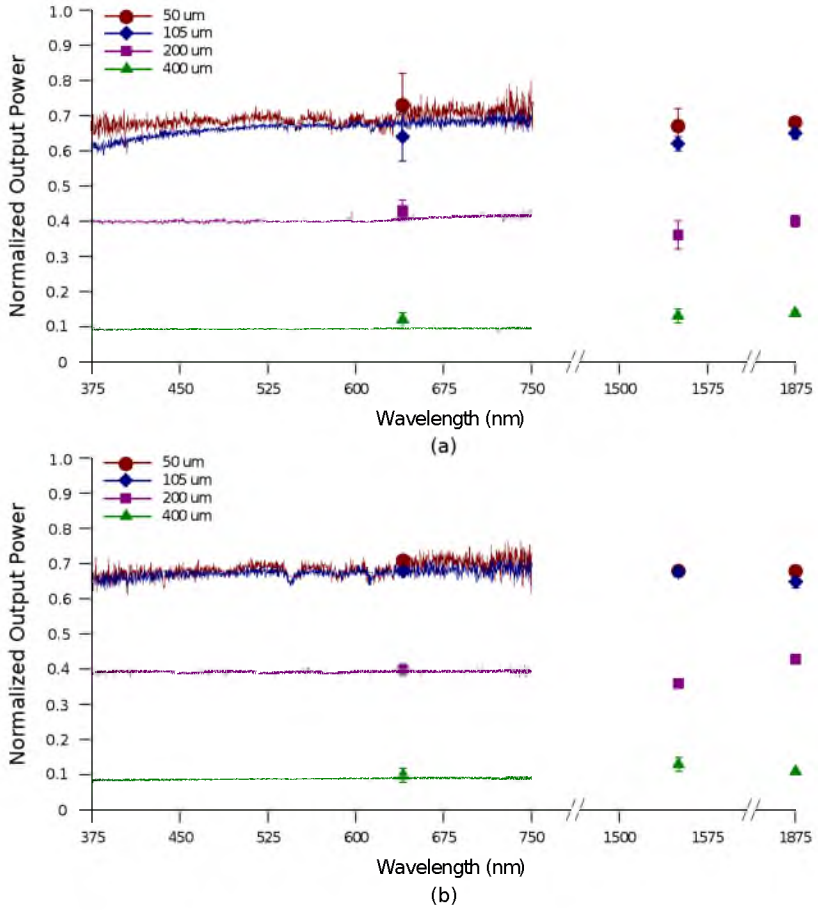

Fig. 8. Transmission of a broadband light source and several discrete wavelengths through the optrodes (150-μm wide, 1.5-mm long shanks and 45° tip taper). In-coupling fibers of different core sizes with 0.22 NA were used. Optrode output from only the tips (a) and from both shanks and tips (b) was measured relative to power from fiber.

#174062 - $15.00 USD Received 9 Aug 2012; revised 18 Oct 2012; accepted 23 Oct 2012; published 1 Nov 2012

Normalized output power from both optrode shanks and tips are plotted in Fig. 7(b) to determine shank losses from either radiation or scattering; any additional power measured in this configuration with respect to the results in Fig. 8(a) constitutes the shank loss. Comparison reveals that the difference between the data points of Fig. 8(a) and (b) is 0.002 (on the 0 to 1 scale) on average, suggesting negligible radiation and scattering from the optrode shanks. Radiation from the shanks is not expected since the shanks are not tapered; scattering is established as an insignificant loss, especially upon consideration of the optrode lengths in use (i.e., less than 1 cm propagation).

4.2. *Illumination with a collimated beam*

Instead of delivering light in smaller beams via fibers, a 4-mm wide collimated beam was used to shine light on the entire array backside in the setup of Fig. 7(a) to evaluate potential use of flood illumination with matrix switching (e.g, DMD, LCD) [51, 52]. To simplify testing, apertures were used to allow light through a localized area. Fig. 9(a) shows the power of the visible spectrum from the optrode tips normalized to the power of the beam out of the aperture as measured with an integrating sphere; the 2-mm aperture coupled light into 25 optrodes, while only 4 optrodes were illuminated with the use of a 1-mm aperture. Regardless of how many optrodes were illuminated, the efficiency remains the same. Note that if there were only one flood light as source, and optrodes were selected for transmission using a spatial light modulator, the efficiency would be the same except that the total output power would be less due to parts of the input beam being blocked.

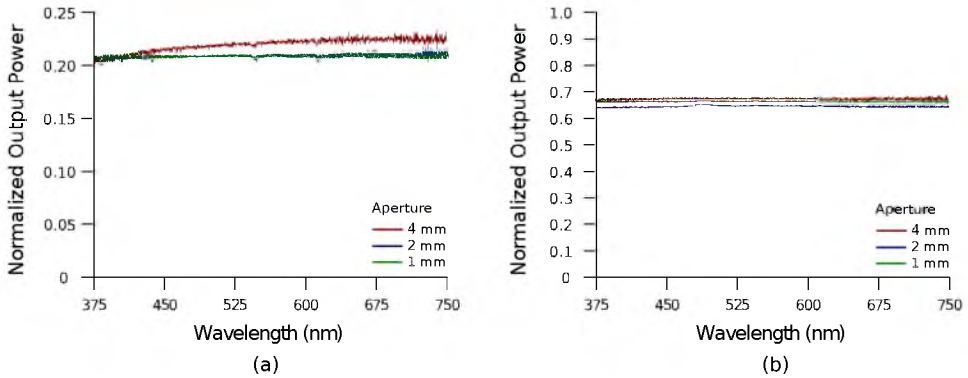

Fig. 9. Transmission of a broadband light source through optrodes (150-μm wide, 1.5-mm long shanks and 45° tip taper). A 4-mm wide collimated beam was used as input and restricted with apertures of different diameters. Light from optrode tips (a) and through backplane (b) were measured relative to the beam power through the aperture.

Due to interest in multilevel excitation, the transmission through the backplane was measured as it may deposit light in a shallow region of tissue near the surface. Fig. 9(b) plots the normalized transmitted power from the backplane alone, which was calculated by measuring the output power using the setup of Fig. 7(c) (i.e., array without blocker foil) and substracting the results of Fig. 9(a). Since light scattering from the shanks is negligible, as verified by the results in section 4.1, the additional power detected when the foil is removed is due almost entirely to transmission through the backplane. More power passes through the backplane than the tips as the interstitial space of the backplane occupies a greater area in the array. Futhermore, TIR does not occur at the backplane-air interface.

#174062 - $15.00 USD Received 9 Aug 2012; revised 18 Oct 2012; accepted 23 Oct 2012; published 1 Nov 2012

4.3. *Transmission vs. optrode geometry*

Geometrical features of a single optrode are its width, length and tip taper angle. To test the effect of the optrode geometry on its transmission, the setup in Fig. 7(a) was utilized with a 50-μm fiber coupling the white light source or single wavelength lasers to the optrodes. From the results discussed in section 4.1, it is evident that a change in the shank width, much like a change in fiber size, will scale the normalized output power from the tips according to Eq. 2. Thus, less power can be coupled into a narrower optrode shank and less output power will be measured consequently. For shanks having larger cross-sectional areas than the fiber core, output power is the same; for instance, a 95-μm wide optrode outputs the same amount of power as a 150-μm wide shank when using a 50-μm in-coupling fiber, as shown in Fig. 10 On the other hand, shank length does not affect transmission efficiency, as corroborated by the results in Fig. 10; this also supports the absence of scattering within and radiation out of the optrode shanks. Optrodes with a 45° tip taper of lengths (L) 0.5, 1.0, 1.5 and 2.0 mm were used. The normalized output power remains constant with varying optrode length because the shanks are straight and retain total internal reflection with negligible losses; this characteristic is contrary to that of tapered silicon optrode shanks, where the length defines the taper and ultimately determines the efficiency [41]. Lastly, the influence of the tip taper angle (θ) on the output power was observed. Fig. 11 shows tips with a taper angle of 45° and 30°. There was no conclusive difference between the results from 30° and the 45° tips. Although more rays theoretically undergo TIR in the sharper 30° tips, not all of these rays contribute to losses; some rays instead refract out through side firing as discussed in section 4.5.

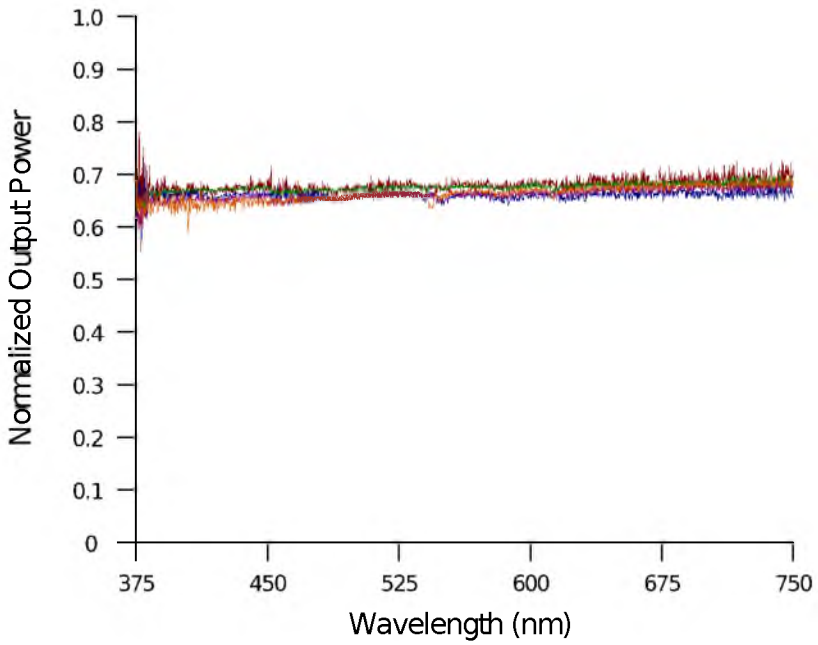

Fig. 10. Transmission of a broadband light source and several discrete wavelengths through the optrodes of varying length L, tip taper angle θ and width W. 50-μm core in-coupling fiber with 0.22 NA was used. Output from optrode tips were measured relative to power from fiber.

The results, along with those presented in section 4.5, suggests that the optrode width, length and tip taper angle are independent variables that may be customized during the fabrication process in order to manipulate optical characteristics of the optrode.

#174062 - $15.00 USD Received 9 Aug 2012; revised 18 Oct 2012; accepted 23 Oct 2012; published 1 Nov 2012

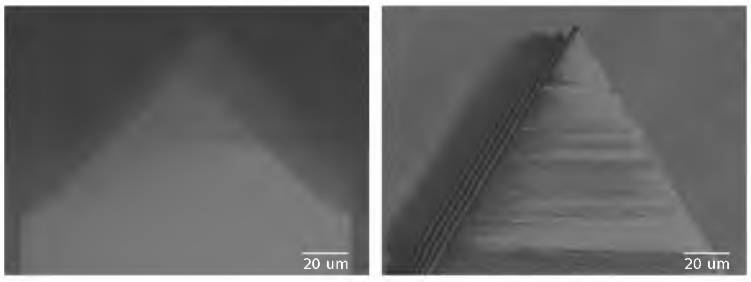

Fig. 11. Optrode tips with 45° (a) and 30° (b) taper angle with respect to the the progation direction (i.e., vertical axis). Shank width is 150 μm.

4.4. *Identifying system losses*

From the results of the previous sections, loss at the input side is almost entirely due to coupling. Still, 30% of the input power is not transmitted out of the tips when coupling from fibers smaller than the shank cross-sectional area; this is true whether the array used for measurement is poked through foil or not. This loss is then due to scattering from the shank and/or TIR in the tip.

The experimental results indicate that scattering in the shank is an insignificant source of loss for the glass optrode. This is supported by considering Eq. 4. Based upon the NA of the fibers used, the largest ray angle with respect to the optical axis is $\theta_m \sim 9°$. Given the dimensions of the optrodes (i.e, width and length), the distance between reflections is about 1 mm for the 150 μm wide shank and 600 μm for the 95 μm shank; therefore, at most three reflections may occur inside the optrode shank. The surface roughness of the optrode measured by the AFM is 22 nm, which is relatively smooth for optogenetics and INS wavelengths according to the Rayleigh scattering criterion $\sigma < \lambda/(8cos\theta_i)$. With this σ value, the total integrated scatter (TIS) associated with a ray striking the shank sidewall is 0.8% (assuming a wavelength $\lambda = 475$ nm and $\theta_i = 81°$). The estimated maximum scattering loss from the shank is then about 2-3%, which is greater than the experimental estimates. The conclusion is that the dominant loss mechanism is the loss of rays transmitting through the tips due to TIR.

4.5. *Beam profiling*

Output beam profiles were obtained to determine the effective spot size, divergence and excitation volume of the light from the optrode tips. Profiles were taken from three sets of optrodes, which differ in width (i.e., 95 or 150 μm) and/or tip taper angle (i.e., 45 or 30°). Tables 3 and 4 shows values of parameters characterizing the profiles, which includes the beam width ($2W_0$) at 13.5 % of peak power, far-field full divergence angle (ϕ) and Rayleigh distance (z_R). Fibers of different core sizes with 0.22 NA were used to couple IR (1550 nm) and red (640 nm) light into the optrode backside.

Output beams take a near-Gaussian form much like the power profile shown in Fig. 12 measured from a 150-μm wide optrode with 45° tip taper angle using a 105-μm in-coupling fiber. The optrode width appreciably affects the output beamwidth, which does not change significantly with tip angle and input wavelength. On the other hand, the output divergence is consistent regardless of optrode width, but significantly changes with the tip taper angle. The spatial divergence of the same optrode used in Fig. 12 is plotted against the propagation distance along the z-plane in Fig. 13; an optrode of the same width but having a 30° tip angle diverges 40° more. An advantage of having the $\phi = 56°$ full angle divergence instead of 16° is that light can be delivered to a continuous plane at about 150 μm depth from the tip when a block of optrodes in the array is excited. A lower tip taper angle causes more rays to undergo TIR, and

#174062 - $15.00 USD Received 9 Aug 2012; revised 18 Oct 2012; accepted 23 Oct 2012; published 1 Nov 2012

Table 3. Output beam width ($2W_0$) in μm at 13.5% of peak power for different optrode geometries (tip taper angle of 45° or 30° and shank width of 95 μm or 150 μm) at two wavelengths (IR and visible). In-coupling fibers of various core diameters (d_f) were used.

	Optrode $2W_0$					
	$\lambda = 1550nm$			$\lambda = 640nm$		
d_f (μm)	45° 95 μm	45° 150 μm	30° 150 μm	45° 95 μm	45° 150 μm	30° 150 μm
50	60	123	118	62	127	119
105	68	122	124	62	125	113
200	73	136	123	63	137	127
400	81	145	123	88	144	121

Table 4. Output beam far-field full angle divergence (ϕ) in ° and Rayleigh range (z_R) in μm for different optrode geometries (tip taper angle of 45° or 30° and shank width of 95 μm or 150 μm) at two wavelengths (IR and visible). In-coupling fibers of various core diameters (d_f) were used.

	Optrode ϕ (z_R)					
	$\lambda = 1550nm$			$\lambda = 640nm$		
d_f (μm)	45° 95 μm	45° 150 μm	30° 150 μm	45° 95 μm	45° 150 μm	30° 150 μm
50	13.7 (245)	16.1 (438)	56.6 (119)	16.5 (220)	17.5 (413)	61.3 (111)
105	15.8 (255)	15.5 (462)	55.9 (128)	18.9 (194)	18.7 (388)	57.0 (113)
200	16.2 (257)	20.0 (390)	69.1 (102)	19.2 (188)	21.0 (372)	76.5 (95)
400	19.9 (233)	20.7 (404)	83.0 (85)	22.7 (224)	22.9 (361)	102.7 (68)

these reflections most likely strike opposite faces of the tip that lead to a greater occurrence of side-firing and hence the higher divergence observed. It then follows that the Rayleigh distance for the 30° tip is much shorter. The Rayleigh distance represents the distance over which the beam width increases by a factor $\sqrt{2}$, and, along with the beam width, roughly defines the volume of maximum energy deposition into the tissue (provided that z_R is smaller than the tissue attenuation length). Because the optrode width only influences the beam width and the tip taper angle only modifies the divergence of the beam exiting the tips, these two geometric parameters can be set independently of each other to get the desired output beam profile. Note that this characteristic is not applicable to the Si optrode as its width and taper are concurrently set by the etching process [41].

When comparing the divergence of the IR and red beams, the divergence is slightly increased for red. The slightly higher refractive index of glass at shorter wavelengths may explain this observation; the higher refractive index at the input side accompanies a higher angle of refraction at the output. In tissue, the beam divergence is expected to be smaller according to Snell's law for both visible and near-IR wavelengths because the refractive index on the output side increases to $n = 1.34$. In addition, the critical angle increases and the output of an optrode with 30° tip taper may due to light refracted through the first interface, instead of side-firing through the second interface due to TIR at the first. Consequently, the beam width may be smaller.

#174062 - $15.00 USD Received 9 Aug 2012; revised 18 Oct 2012; accepted 23 Oct 2012; published 1 Nov 2012

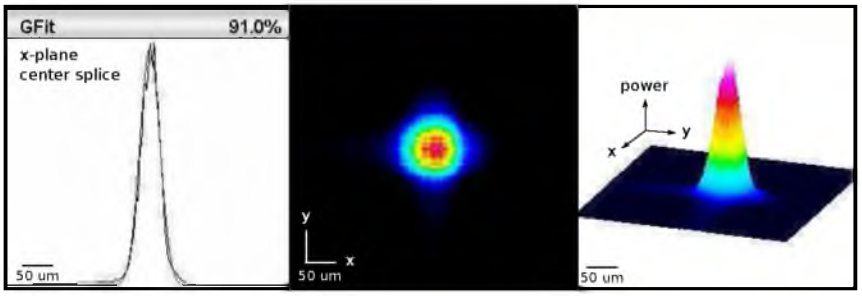

Fig. 12. Beam profile from 150-μm wide optrode with 45° tip taper angle using a 105-μm in-coupling fiber. Power is relative to peak.

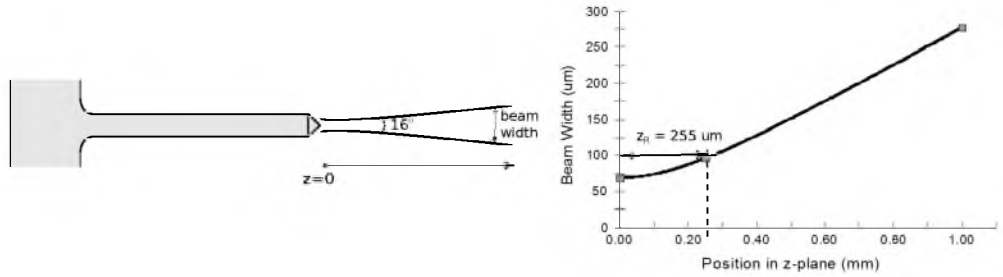

Fig. 13. Changes in beam width with propagation distance from 150-μm wide optrodes with 45° tapered tips; λ=1550 nm was coupled to a 105-μm in-coupling fiber of 0.22 NA.

5. Optrode insertion in tissue

The feasibility of using glass optrode arrays for tissue penetration was tested, but only the ease of implantation and durability of the arrays were examined (i.e., tissue trauma has not been studied with histological data). Three arrays, consisting of 150-μm wide and 1.5-mm long optrodes with 45° tips, were tested in 2% agarose; the same arrays were later inserted post mortem in cat brain (dura removed) and sciatic nerve. Each insertion was repeated at least three times. To begin, the array was rested on the surface of the tissue with the tips facing down. Next, a pneumatic wand inserter was positioned against the optrode backside, where an impulse of force was exerted depending on the desired insertion depth (e.g, 1.5 mm in this case). Fig. 14 illustrates the wand, insertion setup and the implanted arrays. The arrays penetrated the brain and sciative nerve smoothly. However, the curvature of the brain caused difficulty in setting the array in position immediately. In addition, a mechanical support (e.g., ruler) underneath the sciatic nerve was needed to keep the nerve in place during insertion. The arrays were then removed and inspected; the backplane did not fracture and all 100 optrodes were intact after all tests. Overall, all arrays were able to withstand the impact of insertion into tissue.

6. Conclusion

First-generation penetrating glass waveguide arrays for optical stimulation (e.g., optogenetics, INS) have been designed and tested. SiO_2 wafers were used to fabricate a set of arbitrarily-sized (e.g., 10 × 10) arrays by dicing, etching and annealing. Optrode spacing, length, width and tip angle may be independently altered to obtain varying spatial resolution, depth access, output beam width and output divergence, respectively. Output power was measured from the optrode tips; fibers of different core sizes were coupled one at a time to an optrode. Input

#174062 - $15.00 USD Received 9 Aug 2012; revised 18 Oct 2012; accepted 23 Oct 2012; published 1 Nov 2012

Fig. 14. A pneumatic wand inserter was used to fully implant the optrode arrays into 2% agarose (a), cat brain (b) and cat sciatic nerve (c). Arrays were intially rested on top of the tissue with the tips facing down; optrodes smoothly penetrated tissue. Optrodes are 150-μm wide and 1.5-mm long with 45° tips

Fresnel loss with a butt-coupled fiber is computed as 6.5%, but may be eliminated with an index-matching medium. The maximum transmission efficiency obtained was approximately constant at 70% with a 50-μm or 100-μm fiber for wavelengths in the visible spectrum, at 1550 nm, and at 1875 nm. About the same level of output power was measured for varying optrode length and tip taper angle. The decrease in output power with larger fibers follows the limit imposed by coupling efficiency due to area mismatch. As an alternative to in-coupling fibers, a 4-mm collimated beam of white light was used as input to determine the feasibility of implementing flood illumination with optrode selective switching. Applying the same 4-mm beam, transmission through the base was also tested, where majority of the light incident on the array backside passes through.

Shank losses were trivial compared to coupling. Taper losses are not present in the optrode shank, while scattering is considered insignificant because light travels at a grazing incidence along a relatively smooth shank. With an input fiber smaller than the optrode shank, the majority of system loss is determined to come from the tips, where total internal reflection towards the source dominates over Fresnel loss and scattering. However, total internal reflection may also lead to side-firing in less tapered tips such that a wider output beam divergence is observed. The beam divergence is much greater for 30° tips, while the beam width is proportional to the shank width regardless of tip angle. Using a 105-μm fiber, a 150-μm wide optrode with a 45° tip taper emits a $\lambda = 1550$ nm beam with 122 μm diameter and 16° far-field full angle divergence.

Repeated optrode insertion in brain and nerve tissue demonstrated the suitability of the arrays as a neural interface in terms of depth access and durability. The current efficiency of these glass arrays does not leave much room for improvement, except to possibly modify the tip shape and apply an anti-reflection layer to the tip surfaces to reduce Fresnel losses.

Acknowledgements

This work is supported by the University of Utah Research Foundation. We also acknowledge support by Lockheed Martin Aculight and partial support by NSF MRSEC grant DMR 1121252.

#174062 - $15.00 USD Received 9 Aug 2012; revised 18 Oct 2012; accepted 23 Oct 2012; published 1 Nov 2012

CHAPTER 5

DEEP-TISSUE LIGHT DELIVERY VIA OPTRODE ARRAYS

We establish performance characteristics of needle-type waveguides in 3D array architectures as light delivery interfaces into deep tissue for applications such as optogenetic and infrared neural stimulation. A single optrode waveguide achieves as high as 90% transmission efficiency, even at tissue depths >1 mm. Throughout the visible and near-infrared spectrum, the effective light attenuation through the waveguide is ~3 orders of magnitude smaller than attenuation in tissue/water, as confirmed by both simulation and experimental results. Light emission profiles from the optrode tips into tissue were also measured. Beam widths of 70–150 μm and full-angle divergence ranging from 13–40° in tissue can be achieved. These beam characteristics satisfy a wide range of requirements for targeted illumination in neural stimulation.

5.1 Introduction

Intrinsic absorption and scattering limit the penetration of light within tissue and thus places barriers on applications such as optical imaging, diagnostics, and therapy. Recently, tools and techniques have been developed for optical neural stimulation based upon visible [1] and infrared (IR) light [2, 3]. Neural stimulation based on optogenetic techniques utilizes light-activated ion channels that respond to visible or two-photon IR wavelengths [4]; infrared neural stimulation (INS) is another method that is believed to evoke neural signals by heat induced changes in membrane capacitance [5, 6]. When light is delivered externally in these applications, tissue attenuation hinders access to neural structures in deeper layers of cortex or subcortical structures of the brain, or the innermost regions of large nerves.

Optical neural stimulation has gained a lot of interest in the study of neuronal information processing, neuroprosthesis, etc. Cell-type specificity (for optogenetics), long-term viability and the lack of stimulus artifact are several reasons that make optical methods more appealing than electrical-based strategies [2, 7]. Targeted spatiotemporal triggering is desired for comprehensive systematic neural activation, as has been demonstrated with the Utah electrode array for electrical stimulation [8]. For optical stimulation, prominent neural interfaces either involve single/few probes for deep localized light delivery or micro-LED arrays for spatially-adressed high-resolution patterned surface illumination [7, 9, 10]. Recently, 3D multiwaveguide arrays combining deep-tissue and increased multisite light delivery have been reported [11–13]; these devices have yet to be characterized and tested in tissue. Here, we demonstrate that the Utah optrode array devices effectively mitigate the optical attenuation by media into which the arrays may be implanted and produce emission profiles suitable for neural stimulation.

5.2 Optrode array architectures

Silicon and fused silica (glass) optrode arrays shown in Figure 5.1 were previously manufactured and bench-tested [11, 12]. Geometrical aspects of the arrays can be tailored for specific applications, but typical array sizes are 10×10 on a 400 μm pitch, with optrode widths of about 100 μm and lengths ranging from 0.5 mm to several mm's. Based upon current fabrication methods, glass arrays have constant optrode length within the array, but optrodes in silicon arrays can be of constant length or can vary in length along one direction (e.g., forming a "slant" array). When fabricated with methods adopted from electrical arrays [14], silicon optrodes are missile-shaped with little design flexibilty. However, modifications on this fabrication method were needed for glass optrodes [12], which have square shanks with pyramidal tips and can take on any combination of width, length, and tip angle. This modified process can be adapated to silicon optrodes as well. The light transmission efficiency and profiles projected into air were previously characterized, but these properties may change when arrays are implanted in tissue. Optrode arrays are intended to circumvent attenuation in tissue while delivering spatially-addressable light patterns. Each optrode acts as an indepdenent optical waveguide, but as currently implemented, these waveguides lack

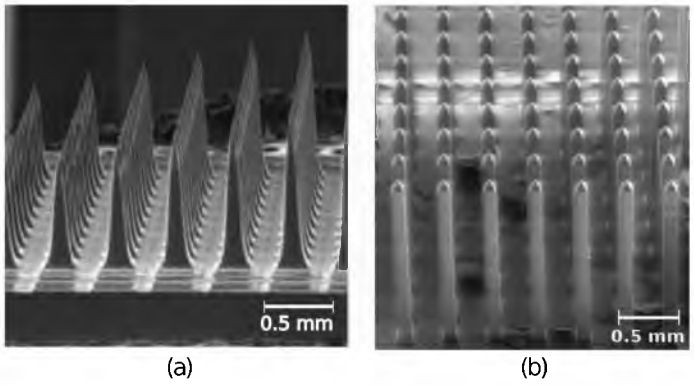

Figure 5.1. Micromachined silicon (a) and glass (b) optrode arrays to facilitate spatially-addressable patterned deep-tissue light delivery.

cladding layers which serve to reduce interface scattering losses and isolate the guided mode from external media. Nevertheless, we show that even without a cladding layer, optrodes transmit light through tissue with high efficiency. In principle, various optical sources such as fiber-coupled lasers, micro-LED arrays, light through spatial light modulators and lensed arrays, and scanning microscopes can be used with these optrode devices.

5.3 Optrodes transmit light through tissue with high efficiency

Glass arrays with optrodes of 120 μm width were implanted in slices of fixed mouse brain, fresh mouse brain, frog sciatic nerve, and agarose. The thickness of each slice was slightly less than the length of the optrodes (1.5 mm), such that the optrode tips were exposed to air. The tips were then inserted through aluminum foil in order to isolate the power emitted from just the tips. White light was coupled through the 170 μm thick array backplane into individual optrodes via a 50 μm core, 0.22 NA multimode optical fiber. The output power from the tips was captured by an integrating sphere and normalized to the power emitted from the in-coupling fiber alone. Figure 5.2 plots the resulting normalized output power from optrodes surrounded by various media. These results demonstrate that transmission is relatively independent of the surrounding tissue optical properties, which means that light penetration depth is primarily dictated by the optrode length. From a physiological perspective, the small reduction in the transmission can be compensated by increasing the source power with minimal risk of tissue damage or spurious stimulation.

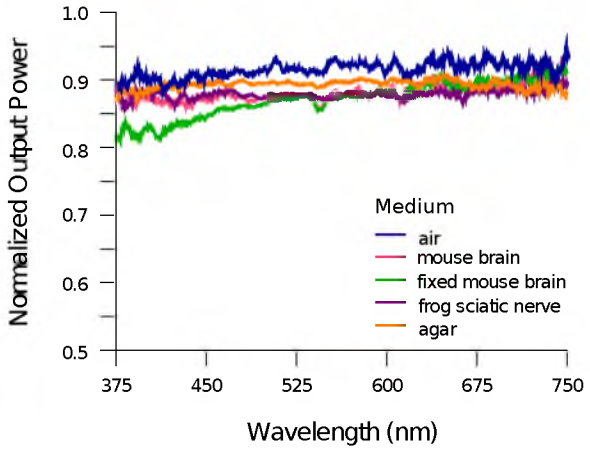

Figure 5.2. Transmission efficiency through optrodes implanted into different tissues and phantoms. A 1.5-mm long glass optrode emits ~90% of the input light through the tip nearly independent of the surrounding medium or input wavelength. Each trace is the average of transmission through 10 independent optrodes.

In the absence of penetrating waveguides, light propagation through tissue was previously shown to drastically attenuate with depth and vary with wavelength; blue and red light through 1 mm-thick mouse brain were shown to decrease to 8% and 27% of the input power, respectively [15].

Although there appear to be only minor differences among the transmission measurements, closer analysis reveals that the transmission through the optrodes actually mirrors the attenuation spectrum of the implantation medium, but with 2 to 4 orders of magnitude reduced effect. This is verified by the experimental measurements and simulation results shown in Figure 5.3. Measurements were taken in the same manner as in Figure 5.2, but normalized to the transmission through optrodes in air to factor out extrinsic losses; a white light source and a tunable telecom laser were used for these measurements. Loss predictions were performed by considering the fraction of the optical mode power that lies outside the optrode (i.e., evanescent), and thus can interact with tissue; Section 5.3.1 discusses the model in detail.

Tissue absorption and scattering leads to loss; tissue chromophores absorb light and scattering occurs due to mismatches in refractive indices of different tissue components and structures. Scattering from the optrode sidewalls due to surface roughness also adds to the attenuation. Nevertheless, the effect of tissue attenuation on light propagation through

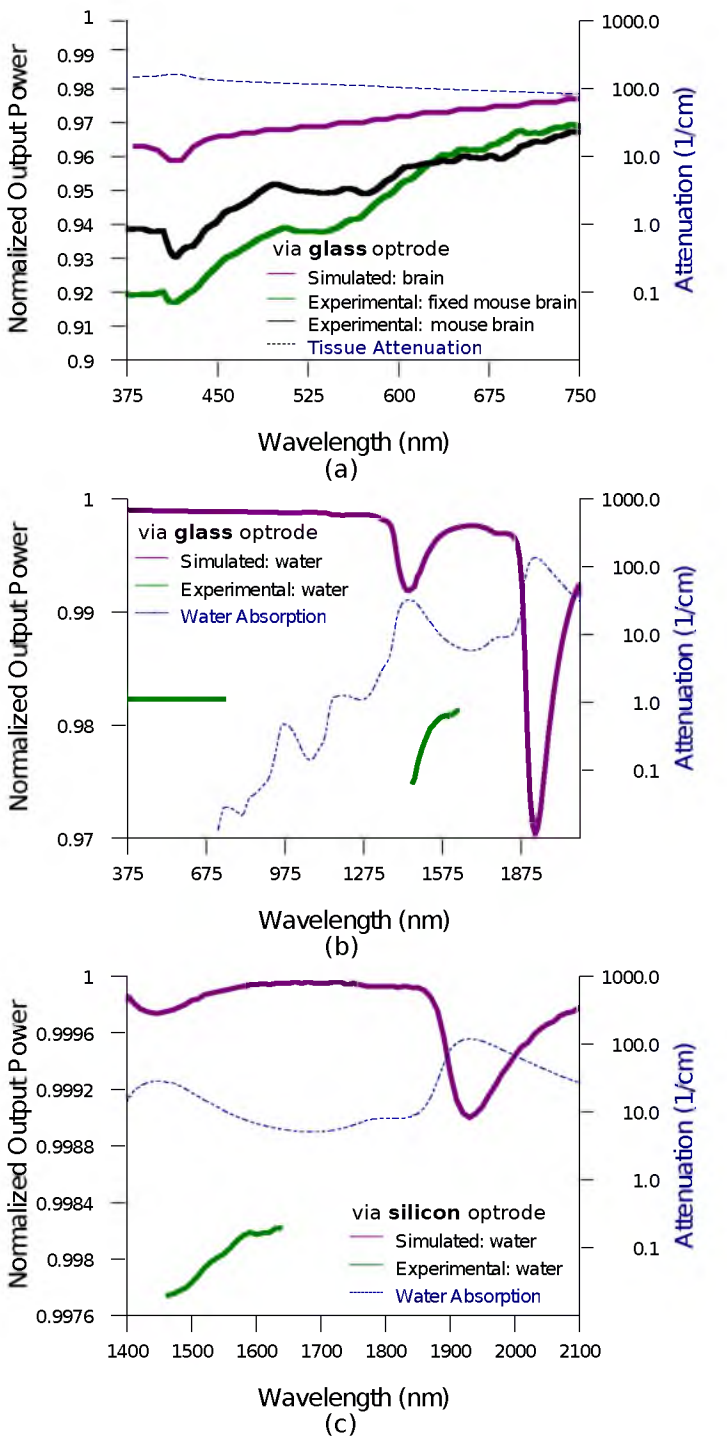

Figure 5.3. Simulation and measurement results for transmission through 1.5-mm long optrodes in tissue/water normalized to optrode transmission into air (left axis). Light attenuation in tissue/water without optrodes is also plotted (right axis). Optrodes reduce the effective attenuation of light by tissue by 2–4 orders of magnitude.

an optrode is reduced by 2–4 orders magnitude, as evident in Section 5.3.2. The effect of the surrounding medium on light transmission is much smaller for silicon optrodes because the high refractive index of silicon confines more power within the optrode. Even though there is some discrepency between the calculated and measured results, there is qualitative agreement between the two in that features due to hemoglobin absorption (around 410 nm; see Section 5.3.2) are clearly evident, and the scaling of attenuation with wavelength due to tissue scattering is consistent. Therefore, the model is useful in predicting the attenuation of light through optrodes in various media, and in predicting the performance of optrodes in potential applications of tissue spectroscopy.

5.3.1 Modeling optrode transmission

In the analysis, the 2D waveguide geometry was reduced to that of a symmetric 1D slab waveguide in order to simplify the eigenvalue problem of solving for guided modes. For different wavelengths, the confinement factor Γ of each guided mode was calculated. Reduced attenuation constants were computed by multiplying the tissue attenuation (i.e., combined absoprtion and scattering) by $(1 - \Gamma)$; the maximum expected optrode sidewall scattering coefficients [16] were then added to derive effective attenuation coefficients (α). Optical properties of the optrode materials and surrounding media (e.g, refractive index, absorption) were maintained in a look-up table according to wavelength [17–23]. The fractional power emitted with each mode was determined using Beer-Lambert's Law with the corresponding α. For tapered silicon optrodes, ray angles along the waveguide continually increase after each reflection, creating radiation loss along the taper due to leaky rays; the radiation loss fraction [24] per mode was also deducted from the transmission. The overall transmission through an optrode is then the weighted average of the modes, calculated according to the source power angular distribution which determines the mode excitation distribution.

The angular source distribution is determined by measurement results from the actual in-coupling optical fiber. The fiber has a 50-μm core diameter with a measured numerical aperture (NA) of 0.17. The angular distribution of the input power is modeled as a Gaussian in the form

$$I \propto e^{-k^2/\sigma^2}, \tag{5.1}$$

where

$$k = \frac{2\pi n \sin\theta}{\lambda} \tag{5.2}$$

and

$$\sigma = \frac{2\pi \mathrm{NA}}{\lambda}. \tag{5.3}$$

Here, n is the optrode refractive index, θ is the angle with respect to the optical axis, λ is the input wavelength and NA is the numerical aperture of the source (i.e., the in-coupling fiber in this case). When the appropriate parameters are used, this model approximates the measured angular distribution of the actual input. Figure 5.4 shows the model closely fitting the measurements in air with input wavelengths of 640 and 1550 nm taken at discrete angles.

To obtain the normalized output power with respect to the power delivered by the fiber (i.e., not to the power entering the optrode), the fraction of power from the source that directly couples to leaky rays was subtracted from the overall transmission. All simulation results were further normalized to the corresponding calculations in air.

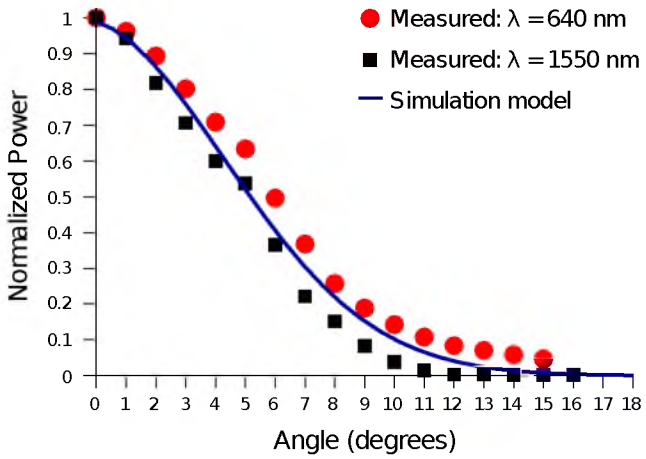

Figure 5.4. Angular distribution of input power from 50-μm in-coupling fiber with a measured 0.17 NA. Data points are measurements with 640 and 1550 nm input wavelengths (λ) in air; line is Gaussian model used for simulations.

5.3.2 Attenuation of light through optrodes in tissue

The predicted optrode sidewall surface scattering coefficient from simulations is plotted in Figure 5.5. Scattering is higher for rougher surfaces and greater refractive index contrast; glass and silicon optrode sidewalls have 22 nm and 4.4 nm root-mean-square (RMS) surface roughness, respectively, as measured by atomic force microscopy. Although the silicon-tissue interface has a significantly higher index contrast, the higher surface roughness of glass optrode shanks contributes considerably more to scattering. The scattering coefficient also decreases with the wavelength, which means that more scattering occurs when using shorter wavelenghts. Regardless, surface scattering is still negligible compared to the multiple scattering and absorption of representative tissue components. The attenuation spectrum for mouse brain is also plotted in Figure 5.5 from data in [20–23]. Mouse brain is modeled as consisting of water, lipids and hemoglobin, but its attenuation of light is dominated by water absorption in the near-infrared. The effective attenuation of light when transmitted through optrodes becomes 2–4 orders of magnitude lower, also shown in Figure 5.5; this supports both simulation and experimental results, where a larger percentage of light can penetrate much deeper in tissue via optrodes.

5.4 Optrode emission profiles fulfill illumination requirements for neural stimulation

Emission profiles from the optrodes were reconstructed from output beam images captured by a CCD camera or a beam profiler at varying distances from the tips. Optrode arrays implanted into tissue, with tips exposed, were again used, but for these measurements the optrode tips were inserted in an additional 100–500 μm slices of fixed mouse brain, from which the 2D spatial power distributions of light at the air interface were imaged. For the purposes of optical neural stimulation, we define the illumination volume by the volume where the intensity is greater than $1/e^2$ of its maximum value at the tip exit. This volume necessarily depends on the beam width at the tip, the beam divergence, and tissue attenuation.

The beams projected from the optrode tips were assumed to propagate as Gaussian beams, where the 2D power profiles measured at different distances from the tip were

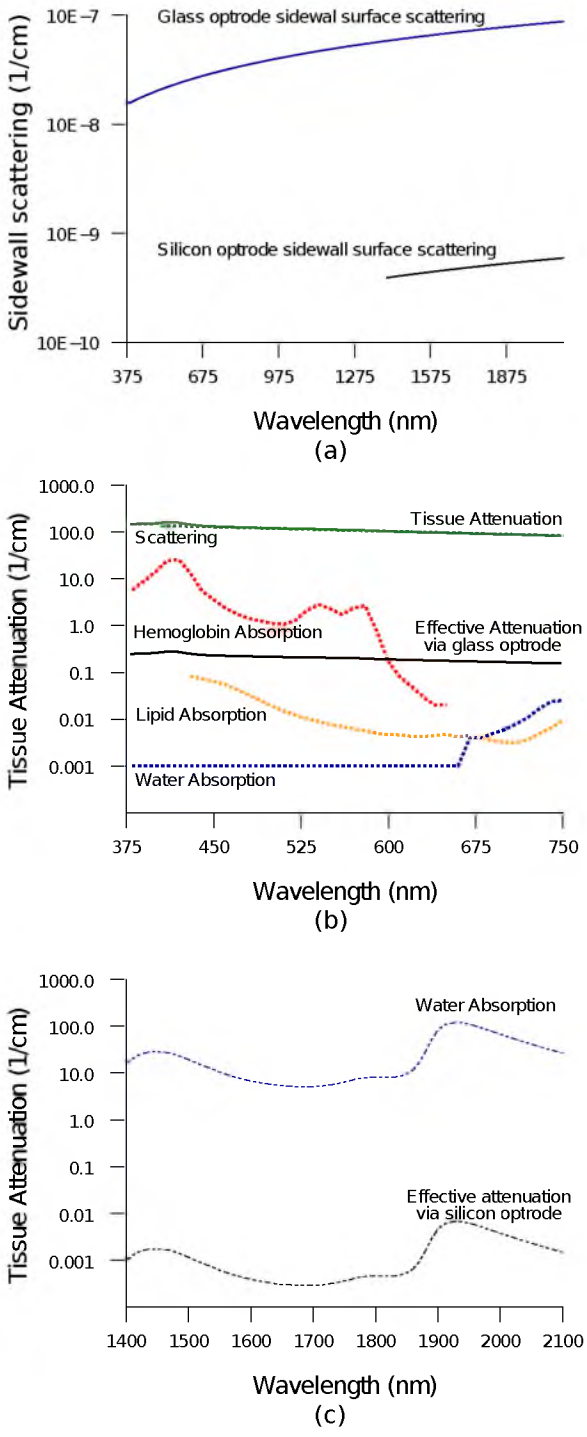

Figure 5.5. Estimated attenuation of light when transmitted in tissue vs. via optrodes in tissue. Scattering coefficient of optrodes due to sidewall surface roughness (a). Absorption and scattering (i.e., attenuation) spectrum of tissue components compared with effective attenuation of light when transmitting through glass (b) and silicon (c) optrodes.

used in fitting the parameters of Gaussian beam propagation. Section 5.4.1 details the Gaussian beam properties and output beam reconstruction. Measured data points and Gaussian-fit approximations for different wavelengths are shown in Figure 5.6 for three sets of optrodes, including silicon and 150-μm wide glass with 45° and 30° (sharper; tip half-angle with respect to optical axis) tips. The estimated beam propagation in a lossless homogeneous n$\approx$1.36 medium is also plotted in Figure 5.6 (with divergence length z_o) for reference extrapolated from beam profile measurements in air (beamwidth smaller than the measurements in tissue due to tissue scattering). Note that, while the fits are based on data only up to depths where measurements were made (400 μm maximum depth), extrapolation is presumed accurate up to the *transport* scattering length (l_t), where scattering becomes truly random. Because tissue components (e.g., cells) are of comparable size to visible-IR wavelengths, scattering is mostly in the forward direction; brain tissue scattering length (l_s; average distance between scattering events) is 50–200 μm from the blue to NIR range and anisotropy (g; amount of forward direction retained) is high at ~0.9, which leads to $l_t = l_s/(1-g)$ of 0.5–2 mm [21, 25]. At depths beyond l_t, light intensity is expected to diminish drastically, and we truncate the Gaussian fit at that distance (e.g., ~0.5 mm for blue and ~0.9 mm for yellow [15]). However, Monte Carlo simulations in tissue, especially in mouse brain illuminated by a divergent light source, suggest that light propagation follows a Gaussian model (i.e., beam width broadens according to Gaussian propagation) even beyond l_t and at depths where normalized intensity falls to <1% [26, 27].

The wider beam and its faster broadening for shorter wavelengths are indications of the higher scattering in tissue (also previously observed in Monte Carlo simulations and experimental data [15, 26]). The results show that 45°-tip glass optrodes provide a more uniform illumination volume through the tissue depth with a divergence length about twice that of the sharper glass optrodes; 30°-tip glass optrodes are suitable for wider and shallower illumination. Note that the fabrication method used for glass optrodes enables a high degree of customization because the output beam width can be varied independently from the divergence by changing the optrode width and tip angle, respectively [12].

We define an effective stimulation volume based upon the exponential intensity decay along the lateral and axial directions from the optrode tips. While ultimately determined

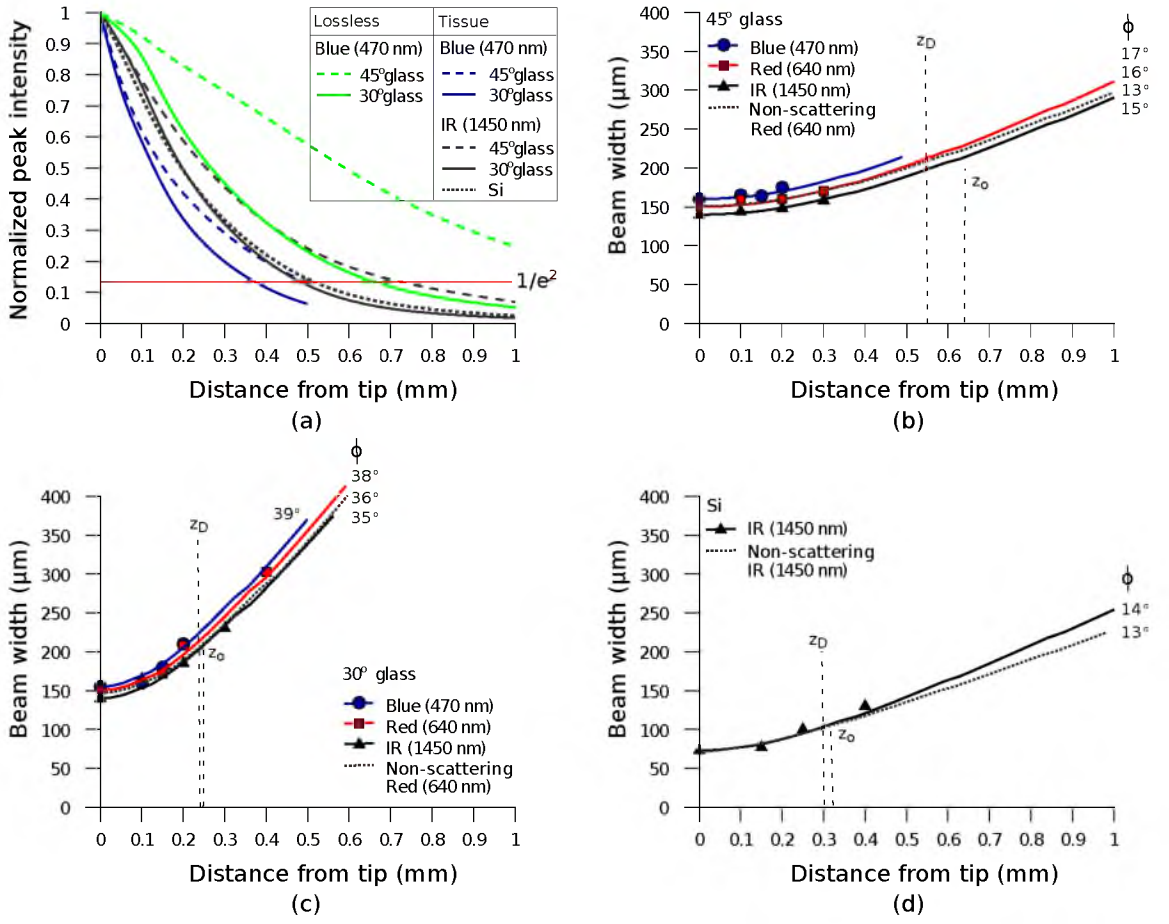

Figure 5.6. Reconstructed beam profiles into fixed mouse brain for different wavelengths emitted by 45°-tip glass (b), 30°-tip glass (c), and silicon (d) optrodes. Effective stimulation volume is dependent on both illumination volume and incident power; intensity decays (exponential fit) into the medium at different rates for various wavelengths, optrode geometry, and tissue properties (a). In the beamwidth plots, symbols are measured data and lines are Gaussian-fit extrapolations (terminated at the transport scattering length; see line for 470 nm). Full-angle divergence (ϕ) and divergence length (z_D, within ± 3 μm across all wavelengths) are indicated. Expected propagation for loss $n \approx 1.36$ medium extrapolated from bench tests in air is also shown in dotted lines (z_D labeled as z_o).

by the local intensity compared to the threshold intensity for activation, the maximum practical depth of stimulation is approximately the $1/e^2$ intensity distance or the transport scattering length, whichever is shorter. Beyond this distance, achieving above-threshold intensity would require large increases in incident power that could cause damage near the tip and only lead to marginal increase in stimulation depth. Normalized intensity with respect to the tip (i.e., 0 mm distance) at various depths changes with the optrode and wavelength used, as shown in Figure 5.6. Notice that a smaller (Si compared with 45° glass) or more divergent (30° glass compared with 45° glass) incident beam results in a greater intensity decay rate, which is consistent with theory. The plots in Figure 5.6 provide the beam spread and intensity decay characteristics and the effective stimulation volumes summarized in Table 5.1. Beam profile requirements vary by application, but optrodes are able to offer various stimulation area and depth combinations; some examples are presented in Section 5.4.2.

5.4.1 Gaussian beam reconstruction of optrode output beams

Single mode Gaussian beam propagation follows

$$w(z) = w_0\sqrt{1+\left(\frac{z}{z_0}\right)^2} \tag{5.4}$$

with

$$z_0 = \left(\frac{\pi w_0^2}{\lambda}\right), \tag{5.5}$$

where w is the radius of the $1/e^2$ contour along the propagation distance z, w_0 is the beam waist (i.e, smallest beam radius at $z = 0$), z_0 is the Rayleigh distance, and λ is the operating wavelength. Note that for a multimode Gaussian-like beam, Equation 5.5 does not strictly hold; the "Rayleigh distance" does not necessarily depend on the beam waist, but we refer to a divergence length as a multimode analogue to the Rayleigh length, which is the distance at which the starting beam width increases by a factor of $\sqrt{2}$.

From experimental measurements using tissue slices of different thicknessses, the beam width at $1/e^2$ peak power is extracted from the 2D beam profiles and plotted against the propagation distance; data points are then fitted into a Gaussian beam model using w_0 and z_0 to project the full-angle divergence. Example 2D profiles imaged in tissue are

Table 5.1. Summary of tip output beam width ($2w_0$) at 13.5 % of peak power, divergence length (z_D), divergence angle (ϕ), $1/e^2$ intensity depth (z_{1/e^2}), and beam width at $1/e^2$ intensity depth (w_{1/e^2}) for transmission of wavelengths of 470, 640 and 1450 nm. Different optrodes (tip taper angle of 45° or 30° with 150 μm shank width glass optrode and 1-mm long silicon optrodes) and an in-coupling fiber of 50 μm was used.

	$\lambda = 470\,nm$					$\lambda = 640\,nm$					$\lambda = 1450\,nm$				
	$2w_0$ μm	z_D μm	ϕ °	z_{1/e^2} μm	w_{1/e^2} μm	$2w_0$ μm	z_D μm	ϕ °	z_{1/e^2} μm	w_{1/e^2} μm	$2w_0$ μm	z_D μm	ϕ °	z_{1/e^2} μm	w_{1/e^2} μm
45° glass	160	548	17	500	210	150	551	16	670	230	140	548	15	720	225
30° glass	155	230	39	380	290	150	227	38	430	320	140	231	35	660	440
Si											70	300	14	510	140

shown in Figure 5.7. Further, Figure 5.8 shows the Gaussian-fitted propagation with an intensity gradient of 45°-tip glass optrode emission profile for the wavelength 640 nm in scattering tissue plotted against both radius and depth of propagation; propagation from the same optrode in lossless n ≈ 1.36 medium is also shown for comparison. The intensity maps are derived from the Gaussian-fit beam spreading and the power vs. depth measurements plotted in Figure 5.9. The Gaussian approximation of propagation is accurate for both lossless and scattering media, but scattering noticeably affects the spatial extent of illumination.

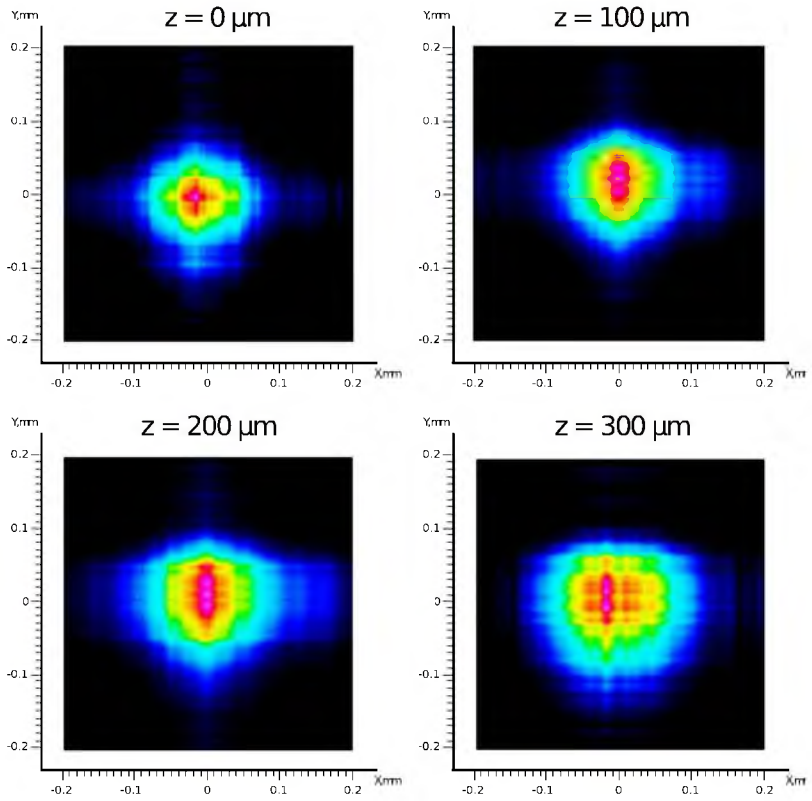

Figure 5.7. Output 2D power profiles imaged by the beam profiler in fixed mouse brain at planes perpendicular to propagation. The tip is located at $x, y, z = 0, 0, 0$. Example images shown are for 45°-tip glass optrodes using a wavelength of 640 nm; x, y scale is from -200 to 200 μm.

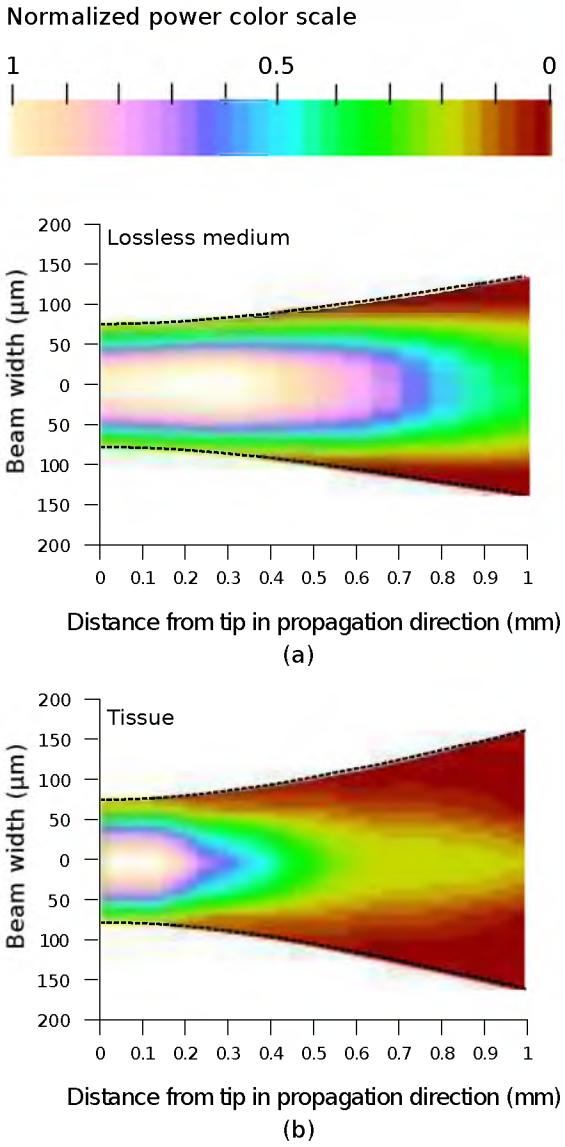

Figure 5.8. 2D intensity gradient of 45°-tip glass optrode output along radius and depth of propagation in both lossless $n \approx 1.36$ medium (a) and scattering tissue (b) at wavelength of 640 nm. Gaussian-fit propagation is outlined.

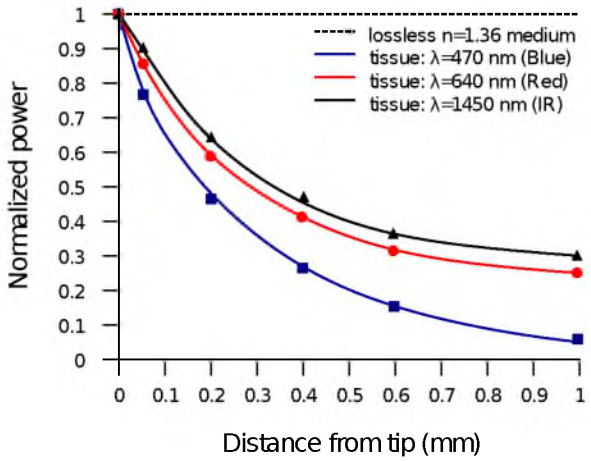

Figure 5.9. Power vs. tissue depth for both lossless and scattering media for different wavelengths.

5.4.2 Potential applications of optrode arrays across experimental paradigms requiring different illumination volumes and protocols

In-vitro optogenetic experiments have demonstrated action potential firing by illumination of a cell body; a spot as small as 5 μm wide can evoke action potential trains, but larger spots up to 15 μm wide increased the spiking rate, photocurrent, and response time [28]. Further widening of the spot can cause additional axonal/dendritic excitation by illuminating the soma (i.e., cell body) and surrounding axons/dendrites of the neuron. 30-μm diameter blue spots were generated from a μLED array to perform multisite dendritic excitation that can sustain spiking for the investigation of physiological information flow in hippocampal slices [10]. The capability to control multiple points in the neural network is the basis of artificial replication of functional processes. This experiment can be translated into an *in-vivo* paradigm by accessing the hippocampus in intact brain using arrays consisting of less divergent thinner optrodes for ~100 micron-sized illumination volumes. Arrays may also benefit other studies in *in-vivo* hippocampus such as the inhibition of epileptiform activity by delivering light to the CA1 and CA3 regions, which are 500–1000 μm wide in mice [29]. Here however, the larger localized area may need a >1 mm wide spot; arrays with micron-wide optrodes are still useful because simultaneous illumination of 30°-tip glass optrodes allow an approximately uniform illumination layer inside tissue with adjoining

profiles from adjacent optrodes. Note that wide-field irradiance is also common in attaining conduction threshold levels for optogenetic stimulation of sparse targets.

Many other optogenetic experiments involve the neocortex, which is a highly nonuniform 3D structure. The neocortex in mammals consists of up to six layers of different neuronal subtypes with a total thickness of 0.5 to 1 mm in rodents to about 2 mm in primates. The neurons in the outermost layers I to III project within the neocortex, while the innermost layers V and VI mostly project to the thalamus, brainstem, and spinal cord; however, neurons in layer VI receive all sensory information to the neocortex. It is commonly accepted that these layers are organized in columns, which comprise the basic functional units; primates have column diameters of roughly 0.5 mm, to which the optrode array pitch can be matched. Cholinergic signaling in the neocortex was studied using optogenetic two-photon microscopy in the IR, which only penetrated layers 1–3 [30]. Direct blue irradiation with glass optrodes could extend the stimulation depth. In contrast to multilayer coverage, stimulation within a single layer is desired such as in exciting and/or inhibiting pyramidal cells in layers II/III and V/VI of the visual cortex for outputs to cortical and subcortical areas, respectively. These layers are 150–500 μm thick and lie 200–500 μm inside the rodent neocortex, and $\sim$0.5 mm thick and $\sim$1.5 mm deep into the primate necortex [31]. Optrode length can be adjusted to access specific layers for these types of studies, and tip angle can be chosen to control stimulation depth.

There are also prominent studies based on highly-selective local firing of peripheral nerves for the restoration of sensory/motor control, which is suited for infrared stimulation. For example, optical neuroprostheses via the sciatic nerve ideally require simultaneous independent access to individual axons. The sciatic nerve ranges in diameter from about 0.5–2 mm in rodents and 3 mm in cats to 2.5 cm in humans. Within the nerve are fascicles, which are bundles of axons that are 200 to 400 μm in diameter; each axon has $\sim$10 μm diameter. There are multiple fascicles lying hundreds of μm's to mm's inside the nerve. Within the nerve, activation of muscle groups can be performed through selective stimulation of axons within different fascicles, and activation of specific motor units can be obtained through selective stimulation of different axons within the same fascicle. This can be achieved with tightly confined beams from thin silicon optrodes of varying lengths

illuminating different axon groups well inside the nerve [32].

5.5 Conclusions

We established the characteristics of light projection into tissue from microfabricated 3D neural interface devices designed to enable patterned deep-tissue light delivery. Experimental and simulation results support the effectiveness of both glass and silicon optrodes in significantly minimizing light attenuation in tissue and providing different spatial profiles of emission for diverse optogenetic and infrared stimulation requirements. Optrodes provide high-efficiency (up to ~90%) delivery of light to >1 mm tissue depths. The variety of possible input sources and optrode geometries provide a custom fit of the output beam to the stimulation target volume dictated by the application. These characteristics may be estimated using simulation models or even calculations from measurements in air to avoid cumbersome tissue tests.

5.6 References

[1] G. Nagel, T. Szellas, W. Huhn, S. Kateriya, N. Adeishvili, P. Berthold, D. Ollig, P. Hegemann, and E. Bamberg, "Channelrhodopsin-2, a directly light-gated cation-selective membrane channel," Proc. Natl. Acad. Sci. U. S. A. **100**, 13940–13945 (2003).

[2] J. Wells, C. Kao, K. Mariappan, J. Albea, E. D. Jansen, P. Konrad, and A. Mahadevan-Jansen, "Optical stimulation of neural tissue in vivo," Opt. Lett. **30**, 504–506 (2005).

[3] K. Dhakal, L. Gu, B. Black, and S. K. Mohanty, "Fiber-optic two-photon optogenetic stimulation," Opt. Lett. **38**, 1927–1929 (2013).

[4] E. S. Boyden, F. Zhang, E. Bamberg, G. Nagel, and K. Deisseroth, "Millisecond-timescale, genetically targeted optical control of neural activity," Nat. Neurosci. **8**, 1263–1268 (2005).

[5] J. Wells, C. Kao, P. Konrad, T. Milner, J. Kim, A. Mahadevan-Jansen, and E. D. Jansen, "Biophysical mechanisms of transient optical stimulation of peripheral nerve," Biophys. J. **93**, 2567–2580 (2007).

[6] M. G. Shapiro, K. Homma, S. Villarreal, C.-P. Richter, and F. Bezanilla, "Infrared light excites cells by changing their electrical capacitance," Nat. Commun. **3**, 736 (2012).

[7] A. M. Aravanis, L.-P. Wang, F. Zhang, L. A. Meltzer, M. Z. Mogri, M. B. Schneider, and K. Deisseroth, "An optical neural interface: in vivo control of rodent motor cortex with integrated fiberoptic and optogenetic technology," J. Neural Eng. **4**, S143 (2007).

[8] R. A. Normann, B. R. Dowden, M. A. Frankel, A. M. Wilder, S. D. Hiatt, N. M. Ledbetter, D. A. Warren, and G. A. Clark, "Coordinated, multi-joint, fatigue-resistant feline stance produced with intrafascicular hind limb nerve stimulation," J. Neural Eng. **9**, 026019 (2012).

[9] S. Royer, B. V. Zemelman, M. Barbic, A. Losonczy, G. Buzski, and J. C. Magee, "Multi-array silicon probes with integrated optical fibers: light-assisted perturbation and recording of local neural circuits in the behaving animal." Eur. J. Neurosci. **31**, 2279–2291 (2010).

[10] N. Grossman, V. Poher, M. S. Grubb, G. T. Kennedy, K. Nikolic, B. McGovern, R. B. Palmini, Z. Gong, E. M. Drakakis, M. A. A. Neil, M. D. Dawson, J. Burrone, and P. Degenaar, "Multi-site optical excitation using ChR2 and micro-LED array," J. Neural Eng. **7**, 016004 (2010).

[11] T. V. F. Abaya, M. Diwekar, S. Blair, P. Tathireddy, L. Rieth, G. A. Clark, and F. Solzbacher, "Characterization of a 3D optrode array for infrared neural stimulation," Biomed. Opt. Express **9**, 2200–2219 (2012).

[12] T. V. F. Abaya, S. Blair, P. Tathireddy, L. Rieth, and F. Solzbacher, "A 3D glass optrode array for optical neural stimulation," Biomed. Opt. Express **3**, 52–69 (2012).

[13] A. N. Zorzos, J. Scholvin, E. S. Boyden, and C. G. Fonstad, "Three-dimensional multiwaveguide probe array for light delivery to distributed brain circuits," Opt. Lett. **37**, 4841–4843 (2012).

[14] R. Bhandari, S. Negi, and F. Solzbacher, "Wafer-scale fabrication of penetrating neural microelectrode arrays," Biomed. Microdevices **12**, 797–807 (2010).

[15] O. Yizhar, L. Fenno, T. Davidson, M. Mogri, and K. Deisseroth, "Optogenetics in neural systems," Neuron **71**, 9–34 (2011).

[16] K. Yamada, "Silicon photonic wire wavegudes: fundamental application," in *Silicon Photonics II*, vol. 119 of *Topics in Applied Physics* (Springer-Verlag Berlin Heidelberg, 2011), pp. 1–29.

[17] G. M. Hale and M. R. Querry, "Optical constants of water in the 200-nm to 200-um wavelength region," Appl. Opt. **12**, 555–563 (1973).

[18] M. Bass, C. DeCusatis, G. Li, V. Mahajan, J. Enoch, E. Stryland, and O. S. of America, *Handbook of Optics: Optical Properties of Materials, Nonlinear Optics, Quantum Optics* (McGraw-Hill, 2009).

[19] V. Tuchin, *Handbook of Optical Biomedical Diagnostics* (SPIE Press, 2002).

[20] S. Prahl and S. L. Jacques, "Optical properties spectra," http://omlc.ogi.edu/spectra (2001).

[21] A. N. Yaroslavsky, P. C. Schulze, I. V. Yaroslavsky, R. Schober, F. Ulrich, and H.-J. Schwarzmaier, "Optical properties of selected native and coagulated human brain tissues in vitro in the visible and near infrared spectral range," Phys. Med. Biol. **47**, 2059 (2002).

[22] X. Han, "Optogenetics in the nonhuman primate," Prog. Brain Res. **196**, 215–233 (2012).

[23] N. G. Horton, K. Wang, D. Kobat, C. G. Clark, F. W. Wise, C. B. Schaffer, and C. Xu, "In vivo three-photon microscopy of subcortical structures within an intact mouse brain," Nat. Photonics. **7**, 205–209 (2013).

[24] Z.-N. Lu, R. Bansal, and P. Cheo, "Radiation losses of tapered dielectric waveguides: a finite difference analysis with ridge waveguide applications," J. Lightwave Technol. **12**, 1373–1377 (1994).

[25] F. Helmchen and W. Denk, "Deep tissue two-photon microscopy," Nat. Methods **2**, 932–940 (2005).

[26] J. G. Bernstein, X. Hana, M. A. Henningera, E. Y. Koa, X. Qiana, G. T. Franzesia, J. P. McConnella, P. Sterne, R. Desimone, and E. S. Boyden, "Prosthetic systems for therapeutic optical activation and silencing of genetically-targeted neurons," Proc. Soc. Photo. Opt. Instrum. Eng. **6854**, 68540H (2008).

[27] L. Wang and S. L. Jacques, *MCML - Monte Carlo modeling of light transport in multi-layered tissues in standard C*, University of Texas M. D. Anderson Cancer Center (USA) (1992).

[28] E. Papagiakoumou, F. Anselmi, A. Begue, V. de Sars, J. Gluckstad, E. Y. Isacoff, and V. Emiliani, "Scanless two-photon excitation of channelrhodopsin-2," Nat. Methods **7**, 848–854 (2010).

[29] J. Tonnesen, A. T. Sorensen, K. Deisseroth, C. Lundberg, and M. Kokaia, "Optogenetic control of epileptiform activity," Proc. Nat. Acad. Sci. **106**, 12162–12167 (2009).

[30] A. Kalmbach, T. Hedrick, and J. Waters, "Selective optogenetic stimulation of cholinergic axons in neocortex," J. Neurophysiol. **107**, 2008–2019 (2012).

[31] J. J. Hutsler, D.-G. Lee, and K. K. Porter, "Comparative analysis of cortical layering and supragranular layer enlargement in rodent carnivore and primate species," Brain Res. **1052**, 71–81 (2005).

[32] G. A. Clark, S. L. Schister, N. M. Ledbetter, D. J. Warren, F. Solzbacher, J. D. Wells, M. D. Keller, S. M. Blair, L. W. Rieth, and P. R. Tathireddy, "Selective, high-optrode-count, artifact-free stimulation with infrared light via intrafascicular utah slanted optrode arrays," Proc. SPIE **8207**, 82075I (2012).

CHAPTER 6

LIGHT IN-COUPLING THROUGH OPTRODE ARRAY NEURAL INTERFACES

This paper analyzes the coupling of light into multimode optrodes from a variety of light sources and/or in-coupling mechanisms for different expermental paradigms—micron-size site-specific light delivery, deep-tissue wide-area illumination, multiwavelength transmission, etc. Optrode arrays were specifically designed for optogenetic and infrared neural stimulation, but may find use in other applications such as imaging. Direct fiber, lensed and collimated beam in-coupling are examined. Analysis of the dependence of optrode transmission efficiency and emission profile on the source or coupling characteristics is presented. Optrodes exhibit as high as ∼90% transmission efficiency and produce symmetric output profiles when in-coupling loss is minimized. Both source and optrode attributes influence light transmission. High-efficiency edge-coupling is possible using sources with small apertures and optrode arrays with thin backplanes. Coupling through objective lenses also achieved ∼90% efficiency using arrays with >0.5 mm thick backplanes.

6.1 Introduction

Optrode arrays have been designed, manufactured, and extensively characterized with respect to optogenetic and infrared neural stimulation requirements [1–3]. Figure 6.1 shows scanning electron micrographs of glass and slanted silicon arrays. These arrays have optrode shank width on the ∼100 μm scale and length on the ∼1 mm scale. Optrodes are essentially penetrating waveguides serving the purpose of efficient localized light delivery into deep tissue; multiple optrodes within a 3D array structure facilitate simultaneous independent access to deep targets for spatiotemporal pattern transmission. These arrays are amenable

to integration with a wide variety of light sources and/or coupling mechanisms. Figure 6.2 illustrates a number of optical sources that may be utilized with optrode arrays.

Optical fibers are currently the most commonly used method for light delivery inside the brain [4]. Ease of handling and wide-spread familiarity with fibers in the optical neural stimulation community facilitate straightforward attachment to arrays for experiments not needing free-range motion of test subjects, but requiring stimulus patterns. Still, one-to-one fiber-to-optrode correspondence will only be practical for arrays with few optrodes such that mechanical limitations of the fiber bundle do not render subjects motionless.

A common test setup in optogenetics that immobilizes animals in acute preparations employs microscopy platforms—scanning, widefield, two-photon, etc. [5]. Like optical fibers, microscopes may be operated easily with implanted optrodes to transmit light power deep inside tissue. Lensing in general can improve coupling from any light source, and spatial light modulators (e.g., digital micromirror device, DMD; liquid crystal display, LCD; acousto-optic deflector, AOD) provide opportunities for spatiotemporal patterning when only a single source is available.

Most interestingly, wireless devices for chronic *in-vivo* tests of free-moving animals may potentially be accomplished using vertical cavity surface-emitting lasers (VCSELs) or light-emitting diodes (LEDs); micro-LEDs (μLED) arrays have already been demonstrated for *in-vitro* patterned optogenetic stimulation via surface illumination [6] and discrete LEDs have been integrated with polymer waveguide arrays [7]. Note that the input coupling methods mentioned are not mutually exclusive. For instance, a microscope has been used with an AOD [8], μLED array emission has been scaled with lenses [6], and a setup with a laser beam directed onto a DMD chip then fed through a microlens array and fiber bundle has been implemented [9].

In this work, light in-coupling to optrodes from distinct sources through various mechanisms are studied to determine conditions for high-efficiency coupling. This includes collimated and divergent sources that are butt-coupled or lensed into the arrays with different geometries. Simulations and experimental results that support theoretical analyses are also presented.

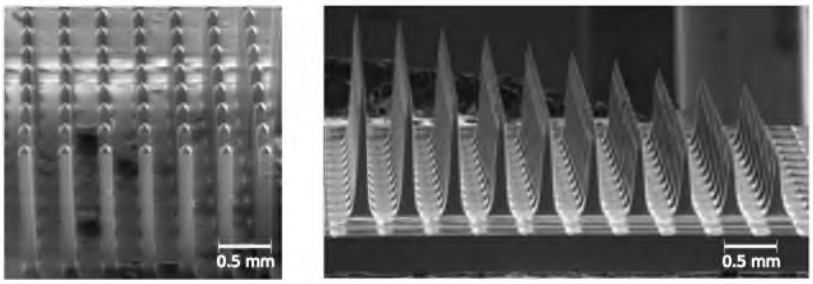

Figure 6.1. Scanning electron micrograph of constant-length glass (a) and slanted silicon optrode arrays (b). Glass arrays shown are 1.5 mm long and 100 μm wide. Silicon arrays have optrodes with 0.5 mm to 1.5 mm lengths and ~300 μm base diameter; shorter silicon optrodes have higher taper slopes.

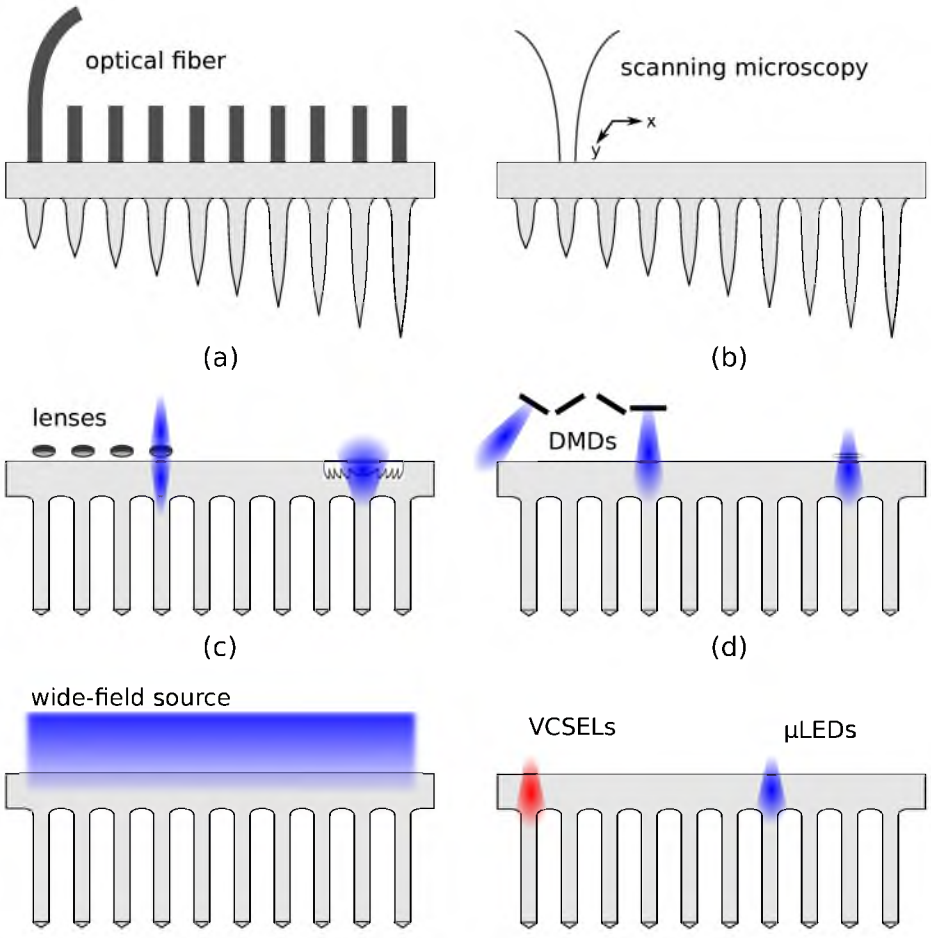

6.2 Theory

Waveguides typically have an inner core section that transmits light and a surrounding cladding material (Figure 6.3). Depending on the core size and its refractive index contrast against the cladding, the waveguide may be single mode or multimode. Modes are the unique spatial distributions of optical field allowed in the waveguide. A "V-number" that indicates how the waveguide parameters influence the number of modes is defined as $V = (2\pi h/\lambda_0)\sqrt{n_{core}^2 - n_{clad}^2}$. Here, λ_0 is the transmitted wavelength, h is the core radius, and n_{core} and n_{clad} are the refractive indices of the core and cladding, respectively. A cylindrical waveguide with a V-number less than 2.405 is considered single mode; otherwise, more than one mode can be transmitted. Optrodes are highly multimoded with $V > 50$ given the relatively large cross-sectional area with respect to the transmitted wavelength and the absence of a cladding that creates high refractive index contrast against the surrounding medium (i.e., tissue). For $V > 8$, ray optics give accurate results and may be used for analyses instead of the more complicated wave theory [10]. The rest of the section gives a brief overview of several illumination and coupling techniques discussed mainly from a ray optics perspective.

6.2.1 Butt-coupling to step-index multimode waveguides

Optrodes are considered step-index waveguides with the "cladding" as the surrounding tissue upon implantation. If the optrode backside is directly placed over the source emitting region, the coupling mechanism is butt-coupling. Figure 6.3 is a simple illustration of imperfect coupling between two step-index waveguides. Coupling loss may arise from a mismatch between the core cross-sectional areas of the waveguides. The area of the source must be less than or equal to that of the receiving waveguide ($a_s \leq a_r$) to avoid loss. Otherwise, the maximum coupling efficiency from area $a_s \geq a_r$ mismatch alone is [11]

$$\eta_{area} = a_r/a_s, \qquad a_s > a_r. \tag{6.1}$$

Waveguides can also only accept or emit light that is incident over a limited range of angles characterized by the numerical aperture

$$NA = n_{core} \sin\theta_{NA} = \sqrt{n_{core}^2 - n_{clad}^2}\,, \tag{6.2}$$

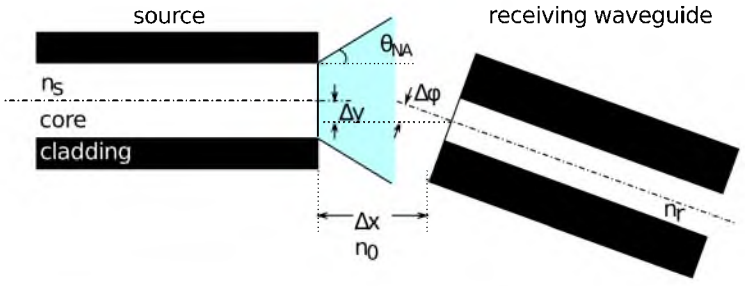

Figure 6.3. Possible losses between butt-coupled step-index multimode waveguides: area and NA mismatch, refractive index mismatch, misalignment, and end separation.

where θ_{NA} is the half-angle of the acceptance/emission cone, and n_{core} and n_{clad} are the core and cladding refractive indices. Similarly, coupling loss is not incurred if the NA of the source is equal or smaller than that of the receiving waveguide ($NA_s \leq NA_r$; emitted cone is narrower than acceptance cone). The coupling efficiency when there is only NA mismatch is

$$\eta_{NA} \leq (NA_r/NA_s)^2, \qquad NA_s > NA_r. \tag{6.3}$$

Fresnel reflection loss also decreases the efficiency in cases where the source and receiving waveguides have different core refractive indices (n) or are not in physical contact. The efficiency accounting for Fresnel loss when there is physical contact is

$$\eta_{ref} = 1 - \left(\frac{n_s - n_r}{n_s + n_r}\right)^2. \tag{6.4}$$

If a gap is present, this coupling efficiency equation is applied twice to include both source and receiving interfaces.

Extrinsic losses from misalignment may be present but may easily be minimized by precise mechanical adjustments. In addition to the reflection loss, end separation reduces power transfer from diverging light sources due to broadening of the beam from core area a_s to area a'_s at the receiving interface a distance Δx away. The coupling efficiency in Equation 6.1 is then modified to

$$\eta_{area} = a_r/a'_s. \tag{6.5}$$

Equation 6.1 is corrected for the case of a lateral misalignment Δy to account for only the overlapping area between the source and receiving waveguide cores

$$\eta_{lat} = a'_{rs}/a'_s, \tag{6.6}$$

where a_{rs} is the area of overlap. Lastly, anglular misalignment yields a maximum efficiency of

$$\eta_{ang} = 1 - \frac{n_0 \Delta\phi}{\pi NA} \tag{6.7}$$

found by computing the overlap of the transmitting and receiving cones with n_0 as the interface medium refractive index and $\Delta\phi$ as the angle between the optical axes.

Note that the overall coupling efficiency is the product of all efficiency factors in consideration.

6.2.2 Coupling through lenses

Coupling through converging lenses, such as a microscope objective, is a common scheme to achieve high efficiency light delivery. The thin lens equation from ray optics governs imaging through lenses:

$$\frac{s'}{f} = \frac{s}{s-f}, \tag{6.8}$$

where f is the lens focal length (i.e., distance between lens and focal point) with t_i and t_o as the image and object distances from the lens. The magnification is simply the ratio of the image to object size (e.g., imaged beam diameter to initial beam diameter), which consequently leads to $M = t_i/t_o$. For lossless coupling or imaging, the limit for the object-to-image size reduction is dictated by the Abbe sine condition $y_s \sin(\gamma_s) = y_{s'} \sin(\gamma_{s'})$. When a circular light source with area $a_s = \pi y_s^2$ and numerical aperture $\mathrm{NA}_s = \sin(\gamma_o)$ is used and mapped on an area $a_{s'} = y_{s'}^2$ with $\mathrm{NA}_{s'} = \sin(\gamma_{s'})$, the smallest possible image area is

$$a_{s',min} = a_s \frac{NA_s^2}{NA_{s'}^2}. \tag{6.9}$$

In addition, $\mathrm{NA}_{s'} < 1$ because $\gamma_{s'} < 90°$, and thus $a_{s',min} \geq a_s NA_s^2$. Note that this equation imposes lossless imaging that is limited at least by the product of the initial beam area and the square of its numerical aperture, which is essentially Equations 6.1 and 6.3 for maximum coupling efficiency.

6.2.2.1 Gaussian beams

Lasers produce Gaussian beam output profiles. Gaussian beams propagate with increasing width according to the mathematical model

$$w(z) = w_0\sqrt{1+\left(\frac{z}{z_R}\right)^2} \tag{6.10}$$

with

$$z_R = \left(\frac{\pi w_0^2}{M^2\lambda}\right) = \frac{w_0}{\theta}, \tag{6.11}$$

where w is the radius of the $1/e^2$ contour along the propagation distance z, w_0 is the beam waist (i.e, smallest beam radius at $z = 0$), z_R is the Rayleigh distance at which $w(z_R) = \sqrt{2}w_0$, λ is the operating wavelength, and θ is the far-field divergence half-angle (i.e., NA angle). An M^2 factor is often defined to denote how an actual beam form having higher order Gaussian modes compares to the basic Gaussian beam. $M^2 \geq 1$ and the ideal Gaussian beam has an M^2 factor of exactly one. The M^2 factor has also been used to describe multimode quasi-Gaussian beams, which contain a Gaussian function in the mathematical models. Note that for a multimode Gaussian-like beam, the "Rayleigh distance" does not necessarily depend on the beam waist, but a divergence length can be defined as a multimode analogue to the Rayleigh length. Beyond the Rayleigh/divergence length, the beam spreads with a full-angle divergence ϕ.

Equation 6.8 for the thin lens equation is modified for Gaussian beams as

$$\frac{t_i}{f} = \frac{\frac{t_o}{f}\left(\frac{t_o}{f}-1\right)+\left(\frac{z_R}{M^2 f}\right)^2}{\left(\frac{t_o}{f}-1\right)^2+\left(\frac{z_R}{M^2 f}\right)^2}. \tag{6.12}$$

Equation 6.12 leads to a maximum $t_{i,max}$ and minimum $t_{i,min}$ focusing distance for the beam. If the input beam has $z_R/(M^2 f) \gg 1$, the beam is focused with $t_{i,max} = t_{i,min} = f$. If $z_R/(M^2 f) \ll 1$, collimation occurs with $t_{i,max} \to \infty$, and $t_{i,min} \to -\infty$. Collimated Gaussian beams have long z_R and low NA. Figure 6.4 illustrates lens imaging of a Guassian beam. Note that if the the object is at the focal point, the image will be at the focal point on the other side regardless of the $z_R/(M^2 f)$ value. The magnification is defined as the ratio of the image to object beam waist, but also relates the transformation in divergence half-angle and Rayleigh distance by

$$m = \frac{w_0'}{w_0} = \frac{\theta}{\theta'} = \sqrt{\frac{z_R'}{z_R}} = \frac{1}{\sqrt{(\frac{t_o}{f}-1)^2+(\frac{z_R}{M^2 f})^2}}. \tag{6.13}$$

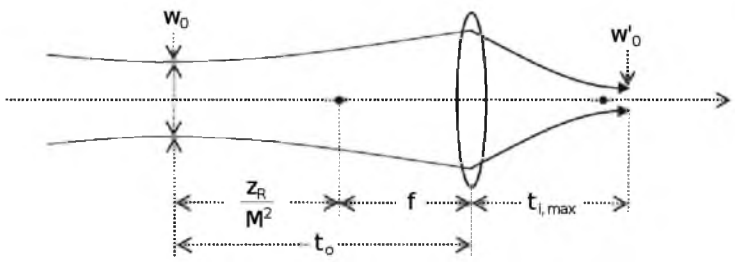

Figure 6.4. Lens imaging of a Gaussian beam. Collimation or focusing may be aproximated using the $z_R/(M^2 f)$ value of the beam.

6.2.2.2 Lambertian sources

A Lambertian source is characterized as having a power distribution $P = P_0 cos\theta$, where θ is the angle of observation with respect to the optical axis and P_0 is the power at $\theta = 0°$. Half of the power of such model is emitted within a 120° full-angle cone. The coupling efficiency from a Lambertian source is approximately $\eta = (a_r/a_s)NA^2$ into a waveguide with characteristic NA and smaller core area a_r than the source aperture area a_s. Again, this is essentially Equations 6.1 and 6.3 considering that a Lambertian source has a numerical aperture approaching 1. Lambertian sources can be coupled to waveguides via collimating lenses for increased efficiency. However, there are limitations to coupling highly divergent beams, such as low coherence light, as briefly addressed in the next section.

LEDs are generally considered lambertian sources [6, 11]. An edge-emitting LED emits half of its power within $\theta = 15°$ and $\theta = 60°$ in orthogonal directions, while real surface-emitting LED radiant patterns are more directed with half the power concentrated within $\theta = 20°$.

6.2.2.3 Widefield sources

Widefield illumination has been accomplished by collimation for coupling into fiber bundles [12, 13]. Collimated beams are shaped from divergent beams via lenses to exhibit very low NA for increased coupling efficiency. The transformation using Gaussian beams was already briefly discussed in Section 6.2.2.1. Aside from the coupling loss sources presented in Section 6.2.1, the packing or fill fraction of the fiber core areas to the bundle area also limit the efficiency. This situation is similar to an entire optrode array backside undergoing

widefield illumination. The efficiency factor is

$$\eta_{fill} = \frac{\sum a_{optrode}}{a_{beam}}, \tag{6.14}$$

where $a_{optrode}$ is the area of an individual optrode and a_b is the area of the collimated beam.

6.2.3 Spatially coherent vs. incoherent sources

The difference between coherent and incoherent sources is noted as it affects in-coupling efficiency as well. Coherent light from lasers is composed of individual fields with the same frequency and phase, leading to a unidirectional strong irradiance. When the conditions in Sections 6.2.1 and 6.2.2 are satisfied, coherent light can be realistically coupled into a waveguide with nearly 100% efficiency.

On the other hand, incoherent sources like LEDs and tungsten lamps emit light with a large angular spread leading to high coupling loss. A lens provides a simple coupling mechanism for broadly distributed radiation. However, when the emitter surface is larger than the receiving waveguide core area, use of a lens is equivalent to butt-coupling [12, 14]. This is explained by the constant radiance theorem, which for a lens means that though imaging has changed the size of the image compared to the object (i.e., image has higher irradiance), the solid angle has changed in exactly the opposite way such that the radiance does not change and thus the coupled power stays the same [12]. Still, divergent light from incoherent sources with smaller aperture areas may be passed through a collimator or concentrator to fill the waveguide core end face and increase the waveguide effective acceptance NA for highly-improved coupling efficiency [12, 13].

6.3 Results and discussion

A variety of waveguide geometries were used to examine the efficiency of different coupling mechanisms. Table 6.1 lists the characteristics of these optrodes. It has already been shown that scattering in glass optrodes is negligible such that transmission efficiency with a particular in-coupling mechanism is approximately equal for optrodes with the same width but varying lengths [2]. In addition, the glass optrode tip angle was shown to have no effect on the transmission efficiency. On the other hand, the different taper profiles of varying-length silicon shanks lead to different transmission efficiency values [1]; the longest

Table 6.1. Optrode geometries used in testing.

	FS-01	FS-01	FS-03	Si-01
Material	Fused silica	Fused silica	Fused silica	Silicon
Shank cross-section	square	square	square	circular
Width (μm)	120	120	70	300 at base
Tip shape	30° pyramid	30° pyramid	30° pyramid	tapered to 5 μm
Backplane thickness (μm)	100	170	170	500

(1.5-mm long) optrodes yielded the highest efficiency and are thus used in this work. White light or monochromatic beams were coupled through fibers and/or lenses and into the optrode waveguides. All tests were performed in air; the optrodes are inserted through an aluminuim foil sheet in order to block power from the backplane during measurements.

6.3.1 In-coupling divergent light

Divergent light sources include both Lambertian and Gaussian sources. In this set of experiments, a ~1 m long 50-μm core fiber with 0.22 NA was butt-coupled to the array backside through an n = 1.45 intervening fluid to minimize interface refractive index contrast and end separation. With a short in-coupling fiber, the beam transmitted into the optrode is dependent on the optical source. For example, a single-mode laser will initially couple into the lower modes of the optical fiber and eventually couple into higher guided modes; as a result, the output of a short fiber may be similar in form to that of the source. Light emitted by the fiber from a laser was characterized and found to be representative of a multimode Gaussian-like beam. The propagation through glass and silicon backplanes is estimated from the input measured in air by a beam profiler. The beam diameter and full-angle divergence upon entering the optrode shank (i.e., at the optrode base after beam spread through the backplane) are listed in Table 6.2 along with the theoretical coupling efficiency with insignificant extrinsic losses from fiber to backside surface. Light emitted by the fiber from a white light source is modeled according to the emission cone of the fiber; the estimated beam characteristics at the optrode base and the coupling efficiency for this setup are also summarized in Table 6.2. Both laser and white light diverges inside the

Table 6.2. Theoretical in-coupling charateristics via ∼1 m long 50-μm optical fiber: approximate full-angle divergence in backplane (ϕ), beam width at optrode base ($2w_0$), and coupling efficiency (η) calculated for a 1550-nm output fiber-coupled laser and for a white light source.

		FS-01	FS-02	FS-03	Si-01
Laser	ϕ (°)	13	13	13	5.5
	$2w_0$ (μm)	243	64	64	70
	η	30	100	100	100
White light	ϕ (°)	13	13	13	-
	$2w_0$ (μm)	277	92	92	-
	η	24	100	74	-

backplane and the beam size at the optrode base determines the coupling efficiency Note that Fresnel reflection is not negligible for silicon but has been factored out for the analysis since it has been demonstrated as an independent loss factor [1]. The numerical aperture of the optrodes are high (∼1 and ∼3 for glass and silicon, respectively) such that the efficiency values are approximated solely from Equation 6.1. Experimental results are summarized in Table 6.3. The normalized output power is measured with respect to the power emitted by the fiber; this includes loss from the coupling effiency and other sources such as the tips.

Table 6.3. Normalized output power (P_{out}) from optrodes, which includes loss from coupling efficiency and other loss mechanisms (e.g., tip backreflection, taper radiation) measured at different wavelengths λ from various light sources.

P_{out}	FS-01	FS-02	FS-03	Si-01
λ=470 nm incoherent (LED)	22	93	66	-
λ=570 nm incoherent (plasma)	22	92±2	66±4	-
λ=640 nm incoherent (plasma)	22	92±2	65±1	-
λ=640 nm coherent (laser)	25	95	94	-
λ=1450 nm coherent (laser)	23	93	93	36
λ=1550 nm coherent (laser)	23	93	93	39
λ=1875 nm coherent (laser)	24	94	93	37

The silicon optrodes have low overall efficiency because of the taper (Si-01) [1]. However, observe that most of the theoretical computations closely appproximate the measured values with room to account for other optrode losses. Incoherent sources are expected to incur more loss as the divergence of light from the fiber immediately starts compared to Gaussian-like beams with far-field divergence. For example, the blue light (470 nm) LED source (Thorlanbs, Inc.) produces a Lambertian emission with a 120° half-power cone. The in-coupling fiber simply limits the output emission angle by its NA. The beam width after propagating through a 170-μm thick backplane is still smaller than 120 μm but larger than 70 μm and hence the large decrease in P_{out} from in-coupling a Gaussian to a Lambertian beam into the thinner optrode (FS-03). In the case of a 120-μm shank, coherent light slightly improves ($\sim$1%) the optrode efficiency possibly due to a larger tolerance in the coupling alignment allowed by its narrower input beam (FS-02). At longer propagation distances (i.e., for thicker backplanes), the Lambertian and Gaussian beam sizes have become similar such that there is no significant efficiency drop observed (FS-01).

Typical fibers have NA from 0.1 to 0.4 such that the area mismatch is the main consideration for this coupling mechanism. Using larger in-coupling fiber diameters will understandanbly result in lower coupling efficiency.

Note that the coupling efficiency from a Lambertian incoherent source to the 0.22 NA fiber is about 5% from the NA mismatch alone. This low efficiency is not truly problematic in the case of fiber-coupling because the fibers distance the optrode-implanted tissue from the power source such that risk of thermal tissue damage (e.g., denaturation) is avoided. The source may still be used as long as sufficient power can be delivered out of the optrodes. In tissue, the transmission will be further reduced according to the optical absorption properties as previously reported [3]; there is at most $\sim$4% drop in the transmission.

6.3.2 Coupling through converging lenses

In this set of measurements, input beams having low divergence (e.g., collimated beams) were passed through objective lenses for coupling into the optrode arrays. White (broad spectrum) and coherent 633 nm (red) and 1550 nm (near-infrared) sources were used. The setup is shown in Figure 6.5. Table 6.4 lists the objective properties with the corresponding

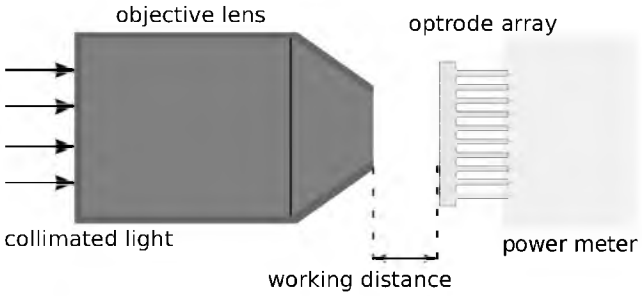

Figure 6.5. Test setup for measuring transmission efficiency when light is coupled through a microscope objective.

estimated theoretical limit for coupling efficiency. These are determined from the imaging and coupling equations presented in Section 6.2, with further details discussed below. The resulting maximum optrode transmission efficiencies are recorded in Table 6.5. The normalized output power of the optrode is with respect to the focused beam; coupling efficiency is only one of the factors that constitute the overall normalized output. Fresnel reflection from the input interface adds a loss of 3.4% for glass arrays and 30% for silicon arrays, which are factored out in the analysis; antireflection coatings make this type of loss negligible. In addition, the shank taper in silicon contributes to the loss [1].

The red collimated light is generated from a HeNe (633 nm) laser with a spot size of 1 mm and divergence 1.3 mrad. This denotes a very long z_R of about 770 mm, which is expected of a coherent Gaussian laser beam. In this case, $z_R/(M^2 f) \gg 1$ causes the image beam waist produced by the objective to be situated at the focal point, which is located at the end of the objective working distance. The spot diameter at the focal point is likely in the range of 1 to 25 μm (from shorter to longer focal length) for the different lenses; this is approximated by Equation 6.13 with $M^2 \sim 1$ and the distance of the laser aperture to the objective aperture as ~150 mm in the setup. The small spot sizes indicate that 100% coupling efficiency may be attained, even for the 40× objective with a very short working distance. The image beam waist in air from the 40× lens is 0.6 mm from the objective but will be farther in a medium of higher refractive index (i.e., focal length increases). The beam waist within the glass blackplane is estimated to be $n_{optrode} \times 0.6\,mm = 0.87$ mm from the backside when the objective is in contact with the array. In this case, the beam is computed as ~48 μm wide with full-angle divergence of 18° when entering the optrode

Table 6.4. Estimated theoretical maximum coupling efficiency for the setup in Figure 6.5 for three light sources, four microscope objectives, and four optrode arrays.

Objectives			Theoretical maximum in-coupling efficiency (%)									
M	NA	WD	FS-01			FS-02			FS-03			Si-01
			White	633 nm	1550 nm	White	633 nm	1550 nm	White	633 nm	1550 nm	1550 nm
50x	0.45	17	100	100	-	100	100	-	100	100	-	-
40x	0.65	0.6	58	100	100	100	100	100	100	100	100	100
20x	0.40	1.6	100	100	-	100	100	-	62	100	-	-
10x	0.25	6.8	45	100	100	45	100	100	16	100	93	100

Table 6.5. Microscope objective lenses used for testing with characteristics listed: magnification (M), numerical aperture (NA) and working distance (WD) in mm. M = 50x objective is a long working distance objective. Corresponding mean optrode transmission efficiencies for different optrode geometries at various wavelengths of light are listed as well. Input Fresnel reflection is factored out.

Objectives			Optrode transmission efficiency (%)									
M	NA	WD	FS-01			FS-02			FS-03			Si-01
			White	633 nm	1550 nm	White	633 nm	1550 nm	White	633 nm	1550 nm	1550 nm
50x	0.45	17	90	96	-	90	96	-	90	96	-	-
40x	0.65	0.6	63	92	90	80	96	92	80	94	93	34
20x	0.40	1.6	90	96	-	90	96	-	51	96	-	-
10x	0.25	6.8	35	96	94	35	96	93	12	96	89	64

at its base. Still, using the 40× objective did not couple light as efficiently as objectives with longer working distances; practically, the lens does not have absolute contact with the optrode, which may be the source of discrepancy for the calculations.

The infrared light comes from a tunable telecom laser coupled to a short 0.22 NA fiber with a 50-μm mode core diameter that is connected to a collimating lens. The collimated beam is modeled as a multimode Gaussian having a diameter of 1.8 mm with full-angle divergence of 0.5° and divergence length of 315 mm according to Equation 6.13. The distance from the collimating lens to the microscope objective aperture is ∼150 mm. This follows a similar analysis as coupling for the HeNe laser beam and thus results in similar values.

The result for silicon optrodes is more interesting. The optrode efficiency when the 40× objective is used is the same as the value achieved for a butt-coupled fiber. On the other hand, the 10× objective notably increased the transmission efficiency. This may be accounted for by the much lower estimated divergence of ∼2° of the propagation within the silicon optrode, which sends the rays straight thru the shank (i.e., negligible taper loss) and out of the tips with minimal tip backreflection.

Laser inputs are representative of using point-scanning confocal or two-photon microscopes, where beams of small spot size, low divergence, and high radiant flux are required.

Lastly, the value for white light is the average achievable efficiency across all wavelengths. Not explicitly shown here is the effect of chromatic abberation, where the transmission varies from blue to red depending on the position of the objective relative to the array backplane. When the objective lens is slightly closer to the array, blue is transmitted with about 92% efficiency and red with 88%; when the objective is moved back, the reverse occurs. White light from a fiber-coupled incoherent source was collimated through another lens and placed ∼150 mm before the objective aperture. The collimated beam fills the objective aperture, which is about 2 mm in diameter. Due to the collimation, the expected image is located at the focal point with diameter equal to (2 mm)/M, where M is the magnification of the microscope objective. For thinner backplanes (FS-02 and FS-03), light may be focused on the optrode base with beam width less than the shank cross-sectional area; The results follow Equation 6.1 for the area mismatch between the focused beam and the optrode area, except for the 40× objective. With the 40× objective, the transmission efficiency achieved

was not as high and a possible explanation involves how the rays exit the optrode tips. At the edge between the shank and the pyramidal tip, total internal reflection (TIR) depends on the angle the ray makes with the tip face instead of the sidewall. Rays propagating at higher angles (i.e., higher-order modes) hit the optrode sidewall with incident angles approaching the critical angle (i.e., decreasing towards the critical angle). With the sharper 30° tip, only rays with incident angles greater than 74° on the sidewall (i.e., less than 16° propagation angle in glass or 0.4 NA emission) will reflect off the tip face for TIR at 44°, which is equivalent to the glass-air interface critical angle. Otherwise, such as in beams from 0.65 NA emission, the ray will refract out of the edge and will not be collected by the power meter. Hence, the measured transmission efficiency is lower. Again, for FS-01, the beam would start to diverge again after ~0.87 mm into the backplane. The beam width at the base is theoretically ~180 μm, which yields a 58% coupling efficiency. Note that the measured data is the only value greater than the predicted theoretical limit.

6.3.3 Widefield illumination

Widefield illumination was accomplished using a 4-mm collimated beam formed through a collimating lens. This closely models use of the microscope for optogenetics and its application with DMDs and LCDs. The typical illumination system in widefield microscopes includes a low angular spread incoherent short-arc lamp for fluorescence excitation. In this test setup, fiber-coupled white light plasma and red (640 nm) laser sources provided the input. With a large collimated beam, the fill-fraction efficiency in Equation 6.14 prevails. The theoretical η_{fill} and measured optrode normalized output power with respect to the collimated beam power are listed in Table 6.6. Fresnel reflection loss is calculated to be 3.4% from air to glass (i.e., $\eta_{ref} = 96.6\%$), which is low in comparison to the loss due to fill-fraction. In addition, the optrode efficiency without coupling loss is about 90%, as shown in Section 6.3.1. The overall efficiency is expected to be $\eta_{fill} \times \eta_{ref} \times 90\%$, which approximates the measured values. Notice that the backplane thickness does not affect the transmission since the beam is wide and collimated; the square ratio of the shank widths is also proportional to the P_{out} ratio. Illumination with the coherent source is negligibly higher due to the more directed light into the power meter.

Table 6.6. Widefield illumination through glass optrode arrays: normalized output power P_{out} and theoretical coupling efficiency due to fill fraction (η_{fill}) with collimated white light and red (640 nm) laser beam.

	FS-01	FS-02	FS-03
Theoretical η_{fill}	11.0	11.0	3.7
Measured P_{out}			
White light	9.6	9.6	3.2
Red	9.7	9.7	3.2

6.4 Future directions and technical considerations for coupling light into optrode arrays

The fibers in use by neuroscientists today may be attached (e.g., by epoxy, anodic bonding, notches [15–17]) to arrays for stability during *in-vivo* experiments, but the motion of animal subjects may be limited and swivel joints may have to be designed to allow more mobility. Thin backplanes desired for in-coupling with fibers may be made more robust, and air gaps may be elimininated if epoxy is used for attachment.

Another drawback of optical fibers for in-coupling is the the need for either dedicated light sources that are typically lasers or complex switching circuitry to allow spatiotemporal pattern delivery. A solution is to use addressable miniature light sources. Discrete LEDs have been glued to fibers [18] and have been bonded to a 3D waveguide array by polymeric bonding using SU-8 photoresist [7]. Alignment is an important step when dealing with arrays. Also, the relatively large divergence of LEDs will likely require lenses to achieve high optrode transmission efficiency. Because a μLED array is in close proximty to tissue as it is mounted on the implanted optrode array, heating must be under control; coupling efficiency must be high to maintain lower input power levels. Microlens arrays may be bonded, reflowed or etched onto the optrode arrays [19–21]. Fresnel lenses may also be designed into the optrode array backside. Alternatively, VCSELS may be able to provide coherent light that may forgo use of lenses at a higher cost.

An untethered device understandably improves range of motion. In this case, μLED or VCSEL arrays will have to be wirelessly controlled.

Lastly, the challenge for multiwavelength in-coupling deals with achieving equivalent emission volumes for highly-localized single-optrode illumination. Different sources will

need to share the space on the optrode backside (e.g., multiple μLEDs per optrode), which possibly leads to varying asymmetrical optrode beam profiles as the spatial launching conditions are different. In addition, tissue optical properties alter the profile. Solutions have yet to be investigated.

6.5 Conclusion

Different experimental paradigms on optical neural stimulation may be achieved by using various light in-coupling techniques with optrode arrays. Optrodes can transmit light into tissue with an efficiency of up to $\sim$90% when in-coupling loss is eliminated. Light coupled into the optrodes via butt-coupled optical fibers may incur minimal loss when the fiber has a small core and the array has a $\sim$100 μm thin backplane. External lenses can achieve maximal efficiency using arrays with $>$0.5 mm thick backplanes. More importantly, proper lensing by forming weakly divergent beams may significantly improve transmission through silicon optrodes. Widefield beams on the array backside is always limited by the fill-fraction of total optrode cross-sectional area in the illuminated spot. Despite the possibility of high transmission efficiency, technical considerations have yet to be overcome towards implementation of integrated optical light delivery microsystems for neural stimulation, especially of free-moving animals for chronic studies.

6.6 References

[1] T. V. F. Abaya, M. Diwekar, S. Blair, P. Tathireddy, L. Rieth, G. A. Clark, and F. Solzbacher, "Characterization of a 3D optrode array for infrared neural stimulation," Biomed. Opt. Express **9**, 2200–2219 (2012).

[2] T. V. F. Abaya, S. Blair, P. Tathireddy, L. Rieth, and F. Solzbacher, "A 3D glass optrode array for optical neural stimulation," Biomed. Opt. Express **3**, 52–69 (2012).

[3] T. Abaya, M. Diwekar, S. Blair, P. Tathireddy, L. Rieth, and F. Solzbacher, "Deep-tissue light delivery via optrode arrays," J Biophotonics (2013).

[4] K. M. Tye and K. Deisseroth, "Optogenetic investigation of neural circuits underlying brain disease in animal models," Nat. Rev. Neurosci. **13**, 251– 266 (2012).

[5] E. Papagiakoumou, F. Anselmi, A. Begue, V. de Sars, J. Gluckstad, E. Y. Isacoff, and V. Emiliani, "Scanless two-photon excitation of channelrhodopsin-2," Nat. Methods **7**, 848–854 (2010).

[6] N. Grossman, V. Poher, M. S. Grubb, G. T. Kennedy, K. Nikolic, B. McGovern, R. B. Palmini, Z. Gong, E. M. Drakakis, M. A. A. Neil, M. D. Dawson, J. Burrone, and P. Degenaar, "Multi-site optical excitation using ChR2 and micro-LED array," J. Neural Eng. **7**, 016004 (2010).

[7] K. Kwon and W. Li, "Integrated multi-LED array with three-dimensional polymer waveguide for optogenetics," in *Proceedings of the International Conference on Micro Electro Mechanical Systems* (2013), pp. 1017–1020.

[8] Y. Liu, Y. Zhao, X. Lv, Y. Li, X. Zhang, J. Zhang, L. Wang, and S. Zeng, "Instrumentation of a compact random-access photostimulator based on acousto-optic deflectors," Rev. Sci. Instrum. **83**, 025116 (2012).

[9] A. N. Zorzos, J. Scholvin, E. S. Boyden, and C. G. Fonstad, "Three-dimensional multiwaveguide probe array for light delivery to distributed brain circuits," Opt. Lett. **37**, 4841–4843 (2012).

[10] A. Ghatak and K. Thyagarajan, "Optical fibers and waveguides," in *Fundamentals of Photonics* (SPIE, 2000), pp. 249–292.

[11] D. Mynbaev and L. Scheiner, *Fiber-optic Communications Technology* (Prentice Hall, 2001).

[12] M. C. Hudson, "Calculation of the maximum optical coupling efficiency into multimode optical waveguides," Appl. Opt. **13**, 1029–1033 (1974).

[13] K. Thyagarajan, A. Sharma, and A. K. Ghatak, "Efficient coupling of incoherent light into optical fibers and bundles," Appl. Opt. **17**, 2416–2419 (1978).

[14] L. F. Stokes, "Coupling light from incoherent sources to optical waveguides," IEEE Circuits. Device. **10**, 46–47 (1994).

[15] J. Holm, H. Ahlfeldt, M. Svensson, and C. Vieider, "Through-etched silicon carriers for passive alignment of optical fibers to surface-active optoelectronic components," Sensor Actuat. A-Phys. **82**, 245–248 (2000).

[16] A. Saran, D. C. Abeysinghe, R. Flenniken, and J. T. Boyd, "Anodic bonding of optical fibers-to-silicon for integrating mems devices and optical fibers," J. Micromech. Microeng, **13**, 346 (2003).

[17] H. Porte, B. Ben Bakir, and S. Bernabe, "Epoxy free butt coupling between a lensed fiber and a silicon nanowire waveguide with an inverted taper configuration," in *IEEE International Conference on Group IV Photonics* (2011), pp. 386–388.

[18] E. Stark, T. Koos, and G. Buzski, "Diode probes for spatiotemporal optical control of multiple neurons in freely moving animals," J. Neurophysiol. **108**, 349–363 (2012).

[19] X. Huang, B. Wang, and Q. Lin, "A thermally tunable microlens array on indium tin oxide glass," in *Proceedings of the International Conference on Miniaturized Chemical and Biochemical Analysis Systems (MicroTAS)* (2008), pp. 287–289.

[20] S. K. Lee, M. G. Kim, K. W. Jo, S. M. Shin, and J. H. Lee, "A glass reflowed microlens array on a Si substrate with rectangular through-holes," J. Opt A-Pure Appl. Op. **10**, 044003 (2008).

[21] P. Savander, "Microlens arrays etched into glass and silicon," Opt. Lasers Eng. **20**, 97–107 (1994).

CHAPTER 7

CONCLUSIONS AND FUTURE WORK

This chapter gives a synopsis of the results and highlights the important contributions of this work. Recommendations for further development and supporting endeavors are also itemized.

7.1 Conclusions

The purpose of the research described in this dissertation is to develop first-generation microwaveguide arrays for three-dimensional highly-localized light delivery in tissue for optogenetic and infrared neural stimulation (INS). Key characteristics of these interfaces include deep tissue access, implantability, robust fabrication, high light transmission efficiency, modifiable emission volumes, and capacity to accommodate multiwavelength spatiotemporal modulation from a variety of sources. To date, demonstrated methods for extending stimulation depth and techniques for simultaneous activation over multiple sites have almost been mutually exclusive. Thus, the specific aims of this work may be summarized as the creation of an implantable light delivery neural interface and the characterization of its performance to enable concurrent selective independent deep-tisue neural activation in a comprehensive area of living tissue (e.g., *in-vivo*, *in-vitro*). The micromachining process yield uniform and enduring structures with modifiable geometry. Because this work does not include neural stimulation tests, long-term biocompatibility was not yet considered and thus, relevant fabrication steps were not implemented. The resulting optrodes transmit light into tissue efficiently and emit beam profiles that match a number of physiological features that may be of interest in various experimental paradigms. Optrode arrays may be used in several ways: single or simultaneous point stimulation, multidepth stimulation, layer stimulation by illumination of all optrodes, multiwavelength stimulation through single or

multiple optrodes, etc. It is envisioned that these optrode arrays, currently in bare form, will initiate a new line of devices that would allow more complex stimulus-response studies and advance understanding of neurological and physiological function.

7.1.1 Adapting the Utah electrode array architectures for infrared neural stimulation

Utah electrode arrays have been proven effective neural interfaces for imitating natural neuronal/muscular responses via high-channel count electrical stimulation and recording [1–4]. Aside from the stimulation protocols, the key is in the scope and spatial resolution of the arrays being mapped well to the architecture of large peripheral nerves and cortical layers across a wide range of mammalian species. With the emergence of neural activation with light, it is only reasonable to hypothesize that a similar device architecture will be able to achieve optical stimulation at the same level of success, although the stimulation mechanism is different. Understandably, light waveguiding is different than current conduction, but the needles of the UEA have been established as minimally damaging to tissue.

The Utah slant electrode array (USEA) introduced in Chapter 1 was then transformed into the Utah slant optrode array (USOA) by using intrinsic silicon that is transparent to near-infrared wavelengths. The procedures for manufacturing elecrode arrays [5] were simplified to include only frontside dicing and etching for USOAs. Prior backside processing is different and consists of patterning alignment marks for in-coupling light into optrodes. As expected, the wafer-scale process is repeatable. In addition, the process provides a margin of controllablity of the optrode geometry and array pitch that later on leads to controllablity in output beam shape.

The amount of light each silicon optrode can transmit and its spatial extent are important measures of the feasibility of the waveguide array devices. High efficiency is desired for minimum input power to prevent tissue heating on the surface, and highly-confined emission volumes are needed for highly-selective INS. Loss was analyzed for arrays with a standard size of 10×10 with 400-μm pitch and optrode lengths of 0.5–1.5 mm. Input of 1550 nm is used as it is apt for laboratory equipment and has the same characteristics as INS wavelengths from the silicon perspective. As it is without special coatings (e.g., cladding, antireflection), the optrodes exhibited losses from Fresnel reflection, radiation due to the

taper, total internal reflection in the tips, and in-coupling; a maximum 40% transmission efficiency was observed and that is from the longest least tapered optrodes. Note that the waveguide taper is formed during etching, and its slope is dependent on the combination of optrode pitch (i.e., base) and length; shorter optrodes taper quicker and lose more power than longer ones for the same base width. Fresnel loss at the in-coupling interface contributed an independent reduction in transmittance, which is small compared to other loss mechanisms. Only coupling loss from source aperture $>200\,mu$m is significant, but light interactions with the base sidewall cause more taper losses for larger source apertures. Tip backreflections within the silicon optrode is deemed to be the major source of loss. Improvements such as antireflection coating, focusing/collimating the input beams, and removing the taper may increase the efficiency of the optrode array to a maximum of 64%. Taking into account the actual higher reflectance loss inside the tips and redesigning the tip shape will yield even higher efficiency values. This suggests that progress is possible for silicon optrodes.

The output beam profile is modifiable within a tight range. The beam size and divergence seem to increase with both optical source aperture area and divergence. Optrode geometry, specifically the taper profile, changes the full-angle divergence within 2–4° deviation in air. Nominal beam size is about 50 μm and divergence varies from 14–20°. This demonstrates a relatively highly-localized stimulation space, which is expected to further decrease in tissue.

Use of the optrode arrays with the commercial Capella infrared neural stimulator (Lockheed Martin Aculight, Inc.), which is the prominent laser employed for various INS applications, was evaluated as well. The maximum system efficiency from laser to fiber to optrode is determined to be only about 10% with a 400-μm fiber that exactly matches the laser emission aperture. The coupling efficiency from laser to fiber dominates the system efficiency. Greater system efficiencies can be obtained using light sources with effective emission apertures smaller than 400 μm.

7.1.2 Glass arrays for both optogenetic and infrared neural stimulation

The USOAs needed to be improved, but the field of optogenetics is growing more rapidly than INS that development of optrode arrays capable of transmitting both visible and

infrared wavelengths is more justified. To this end, fused silica glass (SiO_2) is chosen as substrate material to bulk-micromachine the same architecture as USOAs. However, the differences in wet chemistry between silicon and glass lead to straight-edged glass optrodes with constant length in one wafer (i.e., flat architecture). The absence of the taper is an advantage to transmission efficiency but poses a challenge for implantation. Glass optrode tips were shaped like pyramids, and these led the complete insertion of arrays tissue, albeit with more difficulty. The fabrication process for glass allowed much more degrees of freedom in the design and control of the output beam profile; pitch, length, width, and tip angle can be altered independently to obtain varying spatial resolution, depth access, output beam width and output divergence, respectively. The beam divergence is much greater for sharper tips, more than a three times increase for a $0.5\times$ increase in the tip angle (i.e., slope) with respect to the optical axis. Beam width is proportional to the shank width regardless of tip angle. Using a 105m fiber, a 150-m wide optrode with a 45° tip taper emits a 1550 nm beam with 122-μm diameter and 16° full-angle divergence; 56° for a 30° tip. This strongly indicates the versatility of glass optrodes for multifarious research implementations and aims.

The maximum transmission efficiency obtained was approximately constant at 70% for wavelengths in the visible spectrum, at 1550 nm, and at 1875 nm when a 50- or 100-μm in-coupling fiber is used. Note that the array backplanes were thick and prevented 100% light coupling from source to optrode. The decrease in output power with larger fibers follows the limit imposed by coupling efficiency due to area mismatch. About the same level of output power was measured for varying optrode length and tip angle. As an alternative to dedicated optrode illumination, a 4-mm collimated beam of white light was used as input to determine the feasibility of implementing flood illumination with optrode selective switching. In this case, the transmission efficiency follows the fill-fraction (i.e., sum of optrode areas to illumination area) limit. The majority of the system loss is determined to come from the tips via backreflection towards the source.

With much higher transmission and better output beam control, glass optrodes may well be preferred over silicon optrodes once implantation has been thoroughly studied.

7.1.3 Deep-tissue light delivery via optrode arrays

Both silicon and glass arrays were characterized in tissue. In this set of experiments, glass arrays with thinner backplanes were used to eliminate coupling loss; input beam divergence through glass is considerable while it is negligible within the silicon backplane. The transmission efficiency achieved for glass optrodes increased to more than 90%. Experimental and simulation results prove that both glass and silicon optrodes significantly minimizes light attenuation in tissue. The transmission through optrodes surrounding tissue inversely follows the optical attenuation spectrum. Compared to results in air, efficiency measurements in tissue for glass optrodes only decreased with up to 8% deviation in the visible (decreasing from blue to red) and less than 3% in the near-infrared, again depending on the absorption and scattering characteristics of the wavelength. The values are even closer for silicon optrodes, where the difference between the results in air and tissue are within 0.4%. This simply points out that for a $1\,mW/mm^2$ optrode power calibrated in air, up to an additional $0.08\,mW/mm^2$ may be needed at the output in order to deliver the $1\,mW/mm^2$ into tissue.

The spatial profiles of the optrode tip illumination in tissue were also simulated and measured with wavelengths of 470 m (blue), 640 nm (red), and 1450 nm (INS wavelength). A wider beam and faster broadening for shorter wavelengths is observed, which are indications of the higher scattering in tissue. Results agree with simulation and hand calculations from measurements in air after taking into account the change of the refractive index from 1.0 to ~1.36. From air to tissue, the beam width stays relatively consistent and the divergence narrows in accordance with theory. If highly divergent beams are needed, sharper optrodes than what bench test results suggest are required. The variety of possible input sources and optrode geometries will be able to provide a custom fit of the output beam to the stimulation target volume dictated by a specific application.

The good agreement among simulation, calculated, and experimental values indicate that optrode characteristics may be estimated via models or estimates from air measurements to avoid cumbersome tissue tests.

7.1.4 Light in-coupling to optrode arrays

Different mechanisms of coupling were tested: butt-coupling to single optrodes, lensing, and flood-illuminating arrays. Fibers, microscope objectives, and collimated beams represented these mechanisms, all of which are currently typical light sources or techniques used for optogenetics and INS. Coherent single-mode Gaussian beams and incoherent Lambertian sources were coupled into the optrodes. The methods were analyzed using a collection of well-known theory. Although some of the measured efficiencies appeared to be inconsistent with results from similar cases, all values were explained by considering theoretical limits on coupling and imaging. Light coupled into the optrodes via butt-coupled optical fibers may incur negligible loss when the fiber has a small core and the backplane is as thin as $\sim$100 μm for glass; external lenses can achieve maximal effiency for glass arrays with $>$0.5 mm thick backplanes. However, the efficiency depends on the type of source and the coupling setup (i.e., position of input relative to lens) for Gaussian beams. Widefield beams on the array backside are always limited by the fill-fraction of the total optrode cross-sectional area in the illuminated spot. Despite the possibilty of high transmission efficiency with any source, there are still technical considerations towards implementation of integrated optical light delivery microsystems (i.e., optrode with source, coupling media, and control circuitry) for neural stimulation, especially of free-moving animals for chronic studies. Ultimately, the results demonstrate how the optrode arrays may be used with commonly-applied systems in optical neural stimulation to enhance light delivery protocols.

7.2 Future work

The focus of this work is on device engineering. An iterative process consisting of design, fabrication, and bench testing was performed to evaluate and characterize the utility of the optrode array device. To further optrode array development, the following activities are highly recommended:

(a) *Optimization of optrode array fabrication and insertion.* Fabrication and implantation of silicon arrays is already well-established via the Utah electrode array standard processing procedures. However, the dicing program for glass arrays may be optimized to improve yield and utilization of wafer real estate. In addition,

an alternative dicing technique may be devised in order to produce varying-length glass optrodes within an array and optrodes with less sharp edges (e.g., polygon cross-section). Glass arrays may also benefit from backside processing for alignment marks when optical source circuits are integrated in the future. Insertion protocols may also need revision for glass arrays as early results reveal more difficulty in implantation of such devices.

(b) *In-vitro and/or in-vivo neural stimulation with optrode arrays.* For any device, a collection of proof-of-concept tests is needed. The arrays have already been characterized in tissue and results have been matched to theoretical requirements for neural stimulation with light. Implantation of glass arrays in living tissue has also been performed preliminarily and histological data were encouraging; silicon array insertion was already proven successful (i.e., with insignificant damage) by numerous Utah electrode array studies. However, initial acute *in-vivo* INS with silicon optrode arrays implanted in cat sciatic nerve produced few repeatable clear action potential responses (see Appendix A). Additional controlled INS experiments and fundamental optogenetic trials using the optrode array devices, involving imaging and electrical recording during activation, will yield insight on the relationship among optrode illumination profiles, location of triggered neurons/cells, incident power levels, and neural response strength. Consequently, properly designed experiments will also provide data on tissue stimulation and damage thresholds with using optrode array devices, and efficacy data for different wavelengths delivered through optrodes during INS. All these may be used to evaluate limitations of the optrodes for optical stimulation inside tissue not readily analyzed during bench testing to advance the device engineering aspect of the development process. After the biocompatibility of optrode arrays has been ascertained, chronic tests will assess long-term effects of implantation and long-term performance of the devices.

(c) *Development of hybrid optrode-electrode arrays and optrode arrays for both stimulation and imaging.* *In-vivo/in-vitro* verification of INS is currently performed using separate electrodes placed at a distance from the targeted area. Optogenetic

activation is commonly observed via fluorescence microscopy or discrete fiber/diode-electrode assemblies to record activity in proximity to the stimulation site. As it is, optrode arrays require external recording means. It seems that a simple solution to integrating electrical recording capabilities is to embed an optrode array within a Utah electode array or vice versa, as shown in Figure 7.1. Although the recording site is not immediately adjacent to the stimulation site as allowed in optical methods, the electrode is only μm to mm's away from where light is delivered. Without electrodes, optrode arrays may be optimized for deep-tissue imaging instead. Fluorescence imaging is limited in depth and optrodes can be used for two-way transmission of light (e.g., also for light collection from tissue) such that optical recording in deep regions in intact thick tissue like *in-vivo* brain may be possible. Imaging through optrode arrays will of course have lower resolution than conventional fluorescence imaging.

(d) *Development of fully-integrated optical neural interfaces.* Neuroprosthesis and chronic neuroscience research require neural interfaces with complete systems for light generation, spatiotemporal modulation, recording, etc. This necessisates further investigation in appropriate light in-coupling mechanisms, circuit power constraints for the prevention of tissue heating, and fabrication and packaging methods. Eventually, wirelessly controlled optical sources mounted on the optrode arrays must be achieved to allow hermetic packaging and full implantation without subcutaneous wiring.

(e) *Move towards flexible devices.* There has been an increasing shift towards flexible neural interfaces that conform to tissue movement and minimize scarring, especially

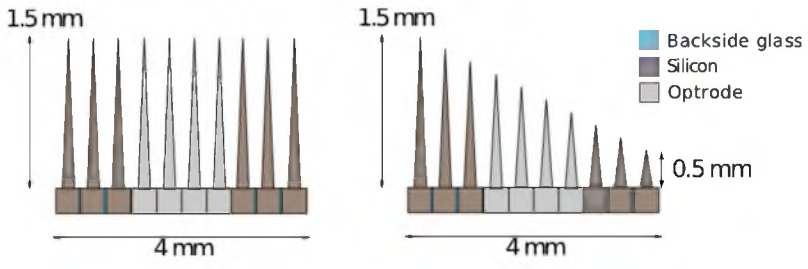

Figure 7.1. Example of a hybrid array consisting of optrodes within a silicon Utah electrode array in flat (a) and slant (b) configurations.

for chronic applications [6–8]. Techniques involving polymer-silicon composites being developed at the University of Utah for Utah electrode arrays can most likely be applied to the optrode arrays [9]. Still, acute investigations could still be executed reliably using the rigid optrode array architecture.

(f) *Encapsulation for long-term biocompatibility.* Biocompatibility of neural interfaces has been enforced by encapsulation techniques involving use of Si carbide, polymide, Si nitride, Si dioxode, silicone, PDMS, or parylene-C [10, 11]. These methods may also be applied to the optrode arrays (note that encapsulation layer adhesion to silicon are practically through its naturally occuring oxide surface), although glass on its own is highly biocompatible and chemically stable [12].

(g) *Cladding and/or antireflection coating deposition.* A built-in cladding will make the optrode performance robust and independent of tissue characteristics. Antireflection coating will improve, even if only slightly, the transmission efficiency of optrodes.

7.3 References

[1] A. Branner, R. Stein, E. Fernandez, Y. Aoyagi, and R. Normann, "Long-term stimulation and recording with a penetrating microelectrode array in cat sciatic nerve," IEEE T. Bio-Med. Eng. **51**, 146–157 (2004).

[2] P. J. Rousche and R. A. Normann, "Chronic recording capability of the Utah intracortical electrode array in cat sensory cortex," J. Neurosci. Methods **8**, 1–15 (1998).

[3] R. Normann, D. McDonnall, G. Clark, R. Stein, and A. Branner, "Physiological activation of the hind limb muscles of the anesthetized cat using the Utah slanted electrode array," in *Proceedings of IEEE International Joint Conference on Neural Networks* (2005), pp. 3103–3108.

[4] R. A. Normann, B. R. Dowden, M. A. Frankel, A. M. Wilder, S. D. Hiatt, N. M. Ledbetter, D. A. Warren, and G. A. Clark, "Coordinated, multi-joint, fatigue-resistant feline stance produced with intrafascicular hind limb nerve stimulation," J. Neural Eng. **9**, 026019 (2012).

[5] R. Bhandari, "Wafer-scale fabrication of penetrating neural microelectrode arrays," Ph.D. thesis, University of Utah (2009).

[6] Y.-T. Kim, R. W. Hitchcock, M. J. Bridge, and P. A. Tresco, "Chronic response of adult rat brain tissue to implants anchored to the skull," Biomaterials **25**, 2229–2237 (2004).

[7] C.-M. Lin, Y.-T. Lee, S.-R. Yeh, and W. Fang, "Flexible carbon nanotubes electrode for neural recording," Biosens. Bioelectron. **24**, 2791–2797 (2009).

[8] T. Wang, W. Yang, H. Huang, and C. Fu, "A novel fabrication method of flexible micro electrode array for neural recording," in *Proceedings of the International Conference on Micro Electro Mechanical Systems* (IEEE, 2007), pp. 295 –300.

[9] B. Baker, R. Sharma, P. Tathireddy, L. Rieth, and F. Solzbacher, "Flexible Utah electrode array for application in neural interfaces," in *Neural Interfaces Conference* (2012).

[10] S. F. Cogan, D. J. Edell, A. A. Guzelian, Y. Ping Liu, and R. Edell, "Plasma-enhanced chemical vapor deposited silicon carbide as an implantable dielectric coating," J. Biomed. Mater. Res., Part A **67A**, 856–867 (2003).

[11] S. Myllymaa, K. Myllymaa, and R. Lappalainen, *Recent Advances in Biomedical Engineering* (InTech, 2009), chap. 9, pp. 165–169.

[12] K. Lilienthal, M. Stubenrauch, M. Fischer, and A. Schober, "Fused silica 'glass grass': fabrication and utilization," J. Micromech. Microeng, **20**, 025017 (2010).

APPENDIX A

INFRARED NEURAL STIMULATION VIA THE UTAH SLANT OPTRODE ARRAY

Infrared neural stimulation (INS) was performed with Dr. Greg Clark and Dr. Dave Warren of the Center for Neural Interfaces. Intrafascicular INS was achieved using the Utah slant optrode array (USOA) implanted in the cat sciatic nerve; the optrode tips are in contact with axons within fascicles of the nerve, as illustrated by the schematic of Figure A.1. Figure A.2 shows the experimental setup. The USOA is inserted in foil to block light transmitted through the backplane. An Utah slant electrode array (USEA) is implanted distal to the USOA to record compound nerve action potentials (CNAPs) while EMG wires were placed within different hind limb mucles to record compound muscle action potentials (CMAPs). A 400-μm fiber connected to the Capella laser was placed in contact with the array backside to deliver light to individual optrodes penetrating the tissue. The backside did not have the aluminum windows described in Chapter 3, but had holes as fiber alignment marks created by deep reactive ion-etching (DRIE), as shown in Figure A.3. Note that holes appear only every other row in this experiment because the optrode pitch is as big as the in-coupling fiber used. A 5 ms pulse at $\lambda = 1873$ nm provided 1–2 mJ of energy out of the optrode tips.

Figure A.4 shows recorded CMAPS after stimulation from two different optrodes in two different cats. EMG signals were observed from the following muscles activated by the sciatic nerve: tibialis anterior (TA), peroneus (Per), medial gastrocnemius (MG), lateral gastrocnemius (LG), and soleus (Sol). There were only few responses recorded from a number of trials, but important observations were noted. First, the activated muscles exhibited strong EMG signals (e.g., TA in Cat 1, Sol in Cat 2). Second, responses were

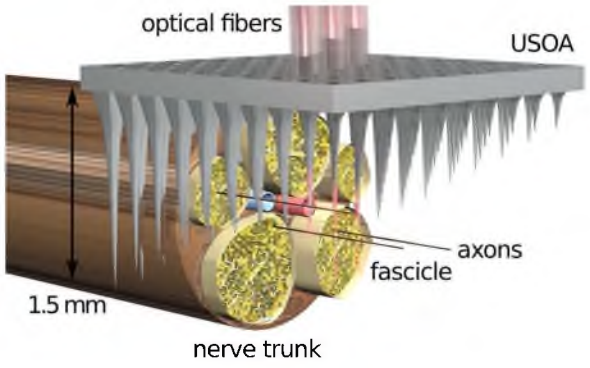

Figure A.1. USOA accesses axons within fascicles during intrafascicular INS.

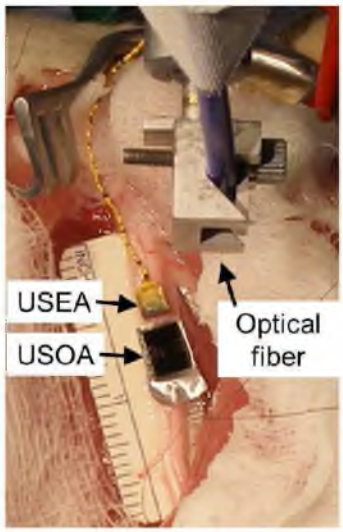

Figure A.2. Experimental setup showing the exposed cat sciatic nerve with the USEA and USOA implanted. The USOA is seen inserted in aluminum foil, the purpose of which is to block light that may be transmitted through the backplane. USEA was implanted to record compound nerve action potentials distal to the stimulation site, and EMG wires not shown here were attached to various muscles to record compound muscle action potentials. The 400-mum optical fiber that delivers the 1875 nm light from the Capella laser was held steady above the nerve.

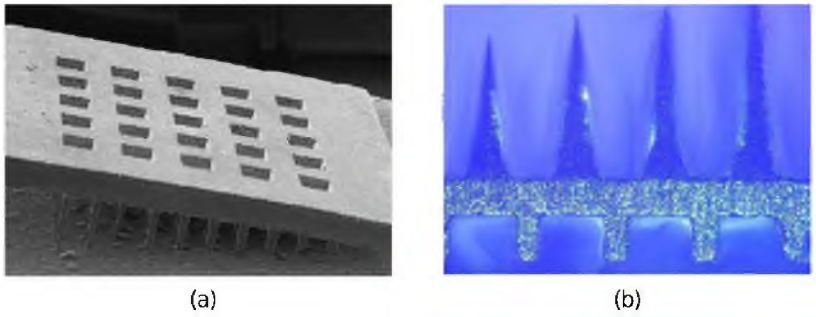

Figure A.3. Silicon optrode arrays used in the experiment had holes etched by DRIE for optical fiber alignment. (a) Scanning electron micrograph showing that holes are placed every other row because the optrode pitch is the same as the fiber core size of 400 μm. (b) Cross-section of arrays showing DRIE holes that are ~300 μm deep.

repeatable; Cat 1's response shows mean data for 9 laser stimuli. Lastly, stimulation produced selective responses. Cat 1 had strong TA response with weak or no response in other muscles, and Cat 2 had strong Sol response without evoked response from other muscles. It was recognized that different optrodes activated different muscles and exhibited selectivity between different muscles innervated by different branches of the sciatic nerve (e.g. TA and MG/LG), between different muscles innervated by the same nerve branch (e.g. LG and Sol from the tibial nerve), and between presumed same nerve fascicle (e.g. MG and SOL). Comparable within-branch selectivity has not been previously reported for extraneural INS of rat sciatic nerve. Moreover, stimulus artifacts were not observed.

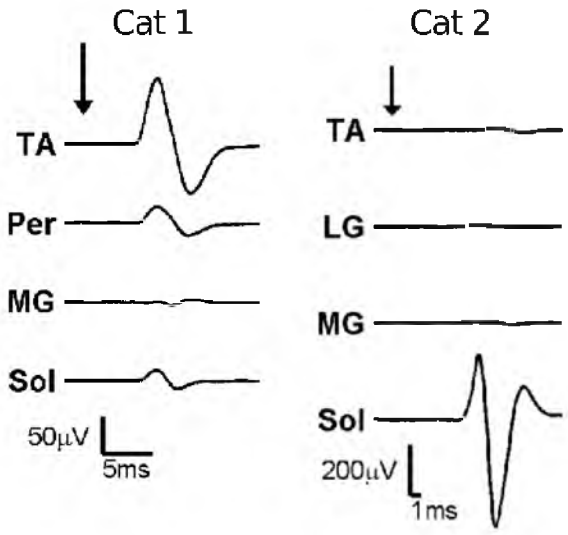

Figure A.4. Compound muscle action potentials were recorded from the cat tibialis anterior (TA), peroneus (Per), medial gastrocnemius (MG), lateral gastrocnemius (LG), and soleus (Sol). These muscles are activated by the sciatic nerve. The arrow indicates time of stimulation onset. Results demonstrate strong, repeatable, selective responses from intrafascicular infrared neural stimulation via Utah slant optrode arrays.

APPENDIX B

TRANSMISSION MODEL FOR OPTRODES IMPLANTED IN TISSUE

The Matlab code for simulation of optrode transmission in tissue mentioned in Chapter 5 is discussed here. The model is limited to a slab (infinitely planar) waveguide, which is justified by the optrode symmetry and its highly multimoded nature. It consists of a main block that ultimately computes for the normalized output power and effective attenuation coefficient with using optrodes and three functions that solve for the loss coefficients, modes, and mode power confinement.

B.1 Optrode attenuation and output power

The optrode output power is computed across wavelengths 370 nm to 2100 nm for every 10 nm. For silicon, the spectrum of analysis was limited in the range 1400 nm to 2100 nm. Relevant refractive indices and attenuation coefficients vary with the wavelength and thus are stored in a matrix file that is loaded into a data array for the code to read (e.g., *si_n.txt* loaded into *index_core* for the silicon optrode). The program goes through a loop until computations for all wavelengths have been performed. Within the loop, the normalized output power of the optrode with respect to the incident power is calculated for a specific wavelength by a function discussed in detail in Section B.2. Once a value is returned by the called function, the value is stored in an array. Next, the wavelength is increased by 10 nm to start the next iteration and a counter for the data array index is incremented. The current transmission result is further normalized to values in air previously determined using the same code. This is to eliminate the effect of in-coupling misalignment and tip losses. Finally, the normalized transmission data is written onto an output file. The code

was written as follows. Note that all radiation terms (e.g. p_{rad}) in the code only appears for silicon analysis.

```
global h;
global k;
global nf;
global nc;
global L;

h=120*10^(-4);
L=0.15;
lambda=1.4*10^(-4);

wavelength = 0.37*10^(-4):0.01*10^(-4):2.1*10^(-4);
index_core = load('si_n.txt');
index_clad = load('tissue_n.txt');
alpha = load('brain_attenuation.txt');

%for eigenvalue solver
%wavetype: 1 means TE, 0 means TM
wavetype=1;
mmm=1*10^(-3);

i=1;
while lambda < 2.1*10^(-4)

nf=index_core(i);
nc=index_clad(i);
k=2*pi/lambda;

[ave_trans]=conf(wavetype, lambda, mmm, alpha(i));
trans(i)=ave_trans;

lambda=lambda+0.01*10^(-4);
i=i+1;

end

air=load('air_trans.txt');
trans1=(trans./air).';
dlmwrite('trans_norm', trans1);
```

The variables are defined as:

h	optrode width; optrode base width for silicon
k	wavenumber
nf	optrode refractive index
nc	refractive index of cladding (i.e., tissue or water surrounding optrodes)

L	optrode length
lambda	wavelength
alpha	attenuation coefficient of cladding
i	counter for array index to store results for different wavelengths
ave_trans	normalized output power with respect to incident power of a specific wavelength
trans	array storing "ave_trans" for all wavelengths
trans1	normalized output power further normalized with respect to results in air

B.2 Power confinement and loss coefficients for the optrode

This function takes information from the main block regarding the wave type (transverse electric [TE] or transverse magnetic [TM]) and wavelength of light launched, a number defining the precision of the mode solver (mmm), and the attenuation coefficient of tissue for the current wavelength considered. The value returned is the normalized output power of the optrode with respect to the incident power.

For each wavelength examined, multiple modes are present in the waveguide such that this function also operates in a loop until all modes have been computed for. The loop starts by calling the eigenvalue mode solver, which is another function discussed in detail in Section B.4. The solver returns parameters describing the mode, of which the effective index (n_eff) and the tranverse wavevector (κ) are specifically used in the rest of the code. The value of κ is passed on to a function that actually computes for the power confinement of each mode; this function is discussed in Section B.3. The scattering coefficient and the fractional silicon taper radiation is also computed using n_{eff} according to [1–3]

$$\alpha_{scat} = \frac{\sigma_{rms}^2}{k(h/2)^4 n_{eff}} \tag{B.1}$$

and

$$p_{rad} = \left(\frac{3n_{eff}}{8\pi} \frac{d_{max}^2 - d_{min}^2}{\lambda L} \right)^2 \tag{B.2}$$

respectively. The factor σ_{rms}^2 is the root-mean-square optrode sidewall surface roughness. For the fractional radiation loss, d_{max} and d_{min} are the maximum and minimum taper

diameters, respectively. The other parameters are the same as previously defined in Section B.1. The power confinement, scattering and radiation data for all modes are stored in an array with each iteration of the loop.

Within the same loop, the corresponding ray angle of the mode is computed and the power of the source for that angle is determined according to the angular Gaussian distribution

$$I \propto e^{-k^2/\sigma^2}, \tag{B.3}$$

where

$$k = \frac{2\pi n_f \sin\theta}{\lambda} \tag{B.4}$$

and

$$\sigma = \frac{2\pi \mathrm{NA}}{\lambda}. \tag{B.5}$$

Here, n_f is the optrode refractive index, θ is the angle with respect to the optical axis, and NA is the numerical aperture of the source (i.e., in-coupling fiber). The source is used later to compute the apportioned power of the leaky modes from angles emitted by the source outside the optrode acceptance cone. The normalized transmission over all modes is also averaged by the Gaussian-weighted source.

To compute for the normalized transmission, the attenuation is first determined. For each mode, the effective attenuation seen by light when travelling through optrodes is

$$\alpha_{eff} = \alpha(1 - p_{eff}) + \alpha_{scat}, \tag{B.6}$$

where p_{eff} is the effective power confinement within the optrode, α is the wavelength-specific tissue attenuation coefficient and α_{scat} is the scattering coefficient due to surface roughness of the optrode sidewalls. In other words, loss is only experienced by the power extending into the tissue (i.e., cladding) and the power scattered by the optrode sidewalls; the scattering coefficient is negligible compared to the cladding attenuation. The normalized power transmitted by each mode follows the Beer–Lambert law

$$T = (p_{eff})e^{-(\alpha_{eff}L)}(1 - p_{rad}), \tag{B.7}$$

where L is the optrode length. The term p_{rad} is only relevant for the silicon optrode to account for the power loss due to its taper profile. The T for all modes is then averaged over

the source power distribution, and the fractional power from leaky modes is subtracted from this weighted average to compute for the overall normalized power transmitted through the optrode by the wavelength with respect to the power supplied by the optical source (e.g., fiber-coupled laser).

The code was written as follows:

```
function [ave_trans]=conf(wavetype, lambda, mmm, att)

global h;
global k;
global nf;
global nc;
global L;

dmax=h;
dmin=2*10^(-4);
maxmode=round(h*k*sqrt(nf^2-ns^2)/pi);
NA=0.22;
sigma=2*pi*NA/lambda;

nu=0;
while nu < maxmode

[neff,beta,kappa,gammas,gammac]=solver(wavetype,lambda,nu,mmm);
[p]=profile(kappa);
scat1(nu+1)=((0.44*10^(-6))^2)/(k*((h/2)^4)*neff);
prad1(nu+1)=(3*neff/8/pi*(dmax^2-dmin^2)/lambda/L)^2;
p_eff1(nu+1)=p;
ang=acos(neff/nf);
%gaussian source
source(nu+1)=exp(-(k*nf*sin(ang))^2/sigma^2);

nu=nu+1;

end

angle=asin(sqrt(nf^2-ns^2)/nf):pi/200:pi/2;
angle2=0:pi/200:pi/2;
leak=exp(-(k*nf*sin(angle)).^2/sigma^2);
leak2=exp(-(k*nf*sin(angle2)).^2/sigma^2);
leak_frac = trapz(angle, leak)/trapz(angle2, leak2);

alpha_eff=(1-p_eff1)*att + scat1;
transmit1=p_eff1.*exp(-alpha_eff*L).*(1-p_rad1);

transmit=transmit1.*source;
ave_trans = sum(transmit)/sum(source)-leak_frac;
```

Important additional variables in this code are defined as:

dmax optrode base width for silicon optrodes only

dmin optrode tip width for silicon optrodes only

maxmode estimated number of modes of optrodes

NA numerical aperture of the source

nu mode number

scat1 array for scattering cofficients for every mode

prad1 array for fractional radiation loss for silicon optrodes only

p_eff1 power confinement of every mode

ang ray angle of every mode

source array of source power for each mode

leak_frac fractional power of leaky modes

ave_trans weighted average of power confinement

B.3 Mode power confinement

This function simply computes for a single mode the fraction of power **p** contained within the optrode to the overall power in both the guided mode within the core and evanescent fields in the cladding; it requires the transverse wavevector (κ) of the specific mode for derivation of other mode parameters such as the longitudinal propagation coefficient (β) within the core and the attenuation coefficient (γ_c) of the power decay in the cladding. The power is calculated by integrating the mode profile; x-y region 1 and 3 is designated for the cladding and region 2 for the core. The code was written as follows:

```
function [p]=profile(kappa)

global h;
global k;
global nf;
global nc;

beta=sqrt((k*nf)^2-kappa.^2);
gammac=sqrt(beta.^2-(k*nc)^2);

x1=0:h/100:h;
x2=-h:h/100:0;
x3=(-2*h):h/100:-h;
y1=exp(-gammac*x1);
```

```
y2=cos(kappa*x2)-(gammac/kappa)*sin(kappa*x2);
y3=(cos(kappa*h)+(gammac/kappa)*sin(kappa*h))*exp(gammac*(x3+h));

x=horzcat(x3, x2, x1);
y=horzcat(y3, y2, y1);
yabs=abs(y);
ysq=yabs.^2;
y2sq=(abs(y2)).^2;
inttot=trapz(x,ysq);
int1=trapz(x2,y2sq);
p=int1/inttot;
```

B.4 Eigenvalue solver

This eigenvalue solver calculates the mode properties using normalized parameters. To begin, the normalized frequency (V) and asymmetry parameter (a) is calculated; a for the optrode is zero because of its symmetry. The normalized effective index (b) is first assumed to be 0.5, which is the midpoint for the possible range of 0 to 1, in order to facilitate the iterative process of determining its accurate value. With this b, a tentative normalized frequency (vb) is solved for using the normalized dispersion relation. For a TE mode for example, the relation is [4]

$$V\sqrt{1-b} = \nu\pi + tan^{-1}\sqrt{b/(1-b)} + tan^{-1}\sqrt{(b+1)/(1-b)}, \tag{B.8}$$

where ν is the mode number from the function *conf* in Section B.2. The tentative vb is compared to the calculated waveguide V and assigns a new value for b depending on which is greater in value. The new b essentially moves closer to the actual b being figured out by half of the current error. The iteration stops once the latest vb is within mmm units of V; mmm is the precision control number defined previously. The last b determined the effective index of the mode. The function returns a value of -1 when there is no solution. The code was written as follows:

```
function [neff,beta,kappa,gammas,gammac]=solver(wavetype,lambda,nu,mmm)

global h;
global k;
global nf;
global nc;

ns=nc;
```

```
%Normalized Parameters
V=k*h*sqrt((nf^2 - ns^2));
a=(ns^2 - nc^2)/(nf^2 - ns^2) ;

b=0.5;
bmin=0;
bmax=1;
if (wavetype)
    vb=(nu*pi + atan(sqrt(b/(1-b))) + atan(sqrt((b+a)/(1-b)))) / sqrt(1-b);
elseif (~wavetype)
    vb=(nu*pi + atan(nf^2/ns^2*sqrt(b/(1-b)))
          + atan(nf^2/nc^2*sqrt((b+a)/(1-b)))) / sqrt(1-b);
end

while (abs(vb-V)>mmm)
    if (vb>V)
        bmax=b;
        b=(b + bmin)/2;
    elseif (vb<V)
        bmin = b;
        b = (b+bmax)/2;
    end
    if ((1-b)<mmm^2)||(b<mmm^2)
        neff = -1;
        beta = -1;
        kappa = -1;
        gammas = -1;
        gammac = -1;
        return;
    end
    if (wavetype)
        vb=(nu*pi + atan(sqrt(b/(1-b))) + atan(sqrt((b+a)/(1-b)))) / sqrt(1-b);
    elseif (~wavetype)
        vb=(nu*pi + atan(nf^2/ns^2*sqrt(b/(1-b))) +
              atan(nf^2/nc^2*sqrt((b+a)/(1-b)))) / sqrt(1-b);
    end
end

beta=k*sqrt((nf^2 - ns^2)*b + ns^2);
neff=beta./k;
kappa=sqrt(k^2*nf^2-beta^2);
gammas=sqrt(beta^2-k^2*ns^2);
gammac=sqrt(beta^2-k^2*nc^2);
```

B.5 References

[1] K. Yamada, "Silicon photonic wire wavegudes: fundamental application," in *Silicon Photonics II*, vol. 119 of *Topics in Applied Physics* (Springer-Verlag Berlin Heidelberg, 2011), pp. 1–29.

[2] S. Tang, L. Wu, F. Li, T. Li, and R. T. Chen, "Compression-molded three-dimensional tapered optical polymeric waveguides for optoelectronic packaging," Proc. SPIE **3005**, 202–211 (1997).

[3] Z.-N. Lu, R. Bansal, and P. Cheo, "Radiation losses of tapered dielectric waveguides: a finite difference analysis with ridge waveguide applications," J. Lightwave Technol. **12**, 1373–1377 (1994).

[4] C. Pollock and M. Lipson, *Integrated Photonics* (Kluwer Academic Publishers, 2003).